DEPARTAMENT OF
MATERIALS SCIENCE

PRINTED ECO-MATERIALS FOR FLEXIBLE THERMOELECTRIC DEVICES

JOANA ROUMELIOTIS SAMPAIO FIGUEIRA

Master in Materials Engineering

DOCTORATE IN MATERIALS ENGINEERING

NOVA University Lisbon

October, 2023

NOVA SCHOOL OF
SCIENCE & TECHNOLOGY

DEPARTAMENT OF
MATERIALS SCIENCE

PRINTED ECO-MATERIALS FOR FLEXIBLE THERMOELECTRIC DEVICES

JOANA ROUMELIOTIS SAMPAIO FIGUEIRA
Master in Materials Engineering

Adviser: Joana Filipa Quintino Loureiro
Researcher, NOVA University Lisbon *

Co-adviser: Luís Miguel Nunes Pereira
Invited Associate Professor, NOVA University Lisbon

Examination Committee:

Chair: Rodrigo Ferrão de Paiva Martins
Full Professor, NOVA University Lisbon

Rapporteurs: Paula Maria Lousada Silveirinha Vilarinho
Associate Professor, University of Aveiro
Carlos José Macedo Tavares
Assistant Professor, University of Minho

Co-Adviser: Luís Miguel Nunes Pereira
Guest Associate Professor, NOVA University Lisbon

Members: André Miguel Trindade Pereira
Assistant Professor, University of Porto
Eliana Maria Fernandes Vieira
Junior Researcher, University of Minho
Rodrigo Ferrão de Paiva Martins
Full Professor, NOVA University Lisbon
Joana Dória Vaz Pinto Morais Sarmento
Assistant Professor, NOVA University Lisbon

DOCTORATE IN MATERIALS ENGINEERING

NOVA University Lisbon
October, 2023

* School of Science and Technology, NOVA University Lisbon, until 31st January 2017.

Printed Eco-Materials for Flexible Thermoelectric Devices

To Manuel, a peerless jewel born in a messed up, but also wonderful world.

To the endless love of my family.

ACKNOWLEDGMENTS

An engineering PhD work is only possible when the student has the opportunity to join experienced researchers and has access to laboratories with the necessary equipment and resources. I am grateful to FCT - Fundação para a Ciência e Tecnologia, for investing in my thesis proposal through a scholarship that enabled me to embrace this challenge (SFRH/BD/121679/2016). I really thank my supervisors Joana Loureiro and Luís Pereira for allowing me to start this journey with them and for their help along the way and to CENIMAT/CEMOP for having welcomed me and providing me conditions to be a "young researcher". I also want to thank Eliana Vieira of Minho University and Cristina Gaspar from AlmaScience for their guidance and support throughout my tasks. I want to acknowledge Swansea University for the chance to walk through their facilities, talk to people with background in thermoelectrics and printing and see some science happening. This PhD work was also financed by national funds from FCT, IP, and FEDER, under the scope of the projects PTDC/CTM-NAN/5172/2014, PTDC/CTMBIO/6178/2014, UID/CTM/50025, PTDC/NAN-MAT/32558/2017, UID/CTM/50025/2019, PTDC/CTM-PAM/4241/2020, LA/P/0037/2020, UIDP/50025/2020, UIDB/50025/2020, UIDB/04436/2020, UIDP/04436/2020. It has also received funding from the European Union Horizon 2020 under the grants agreements 640598 (ERC-2014-STG NEW-FUN), 692373 (BET-EU, H2020-TWINN-2015, GA), 952169 (SYNERGY, H2020-WIDESPREAD-2020-5, CSA), and 101008701 (EMERGE, H2020-INFRAIA-2020-1).

I will not write endless personal thanks to colleagues hoping that they know how grateful I always was and that they felt that I helped them too whenever I could. Science is indeed teamwork and I really enjoyed meeting you all! As for my friends (some already included in the colleague's category, of course!)… Although being part of my life is sometimes getting into a rollercoaster, you must confess… You like it and probably have a rollercoaster of your own too. Let us continue the sad and happy rides together, Patanisca! Finally, the atom nucleus, my family. They truly proved that family is where love begins and never ends. There are no words to express my humble and endless gratitude for all the support they have provided me during my whole life. Without them, my scientific work along with my motherhood experience would not be fruitful. An enormous gratefulness especially to my mother, my father, and my grandmother.

“All creative scientists know that the true laboratory is the mind,

where behind the illusions they uncover the laws of truth."

(Paramahansa Yogananda)

ABSTRACT

The Internet of Things is already a reality, driving the need for scientists to develop and integrate cost-effective, biocompatible, flexible, and lightweight solutions for universal connectivity, including sensing features. Additionally, sustainability emphasizes the importance of using eco-friendly materials and choosing energy-efficient production techniques.

While often promoted as a green energy source, thermoelectric materials excel in temperature-sensitive applications, being capable of detecting thermal stimuli such as human touch. The combination of sustainable Seebeck coefficient holding materials with printing methods enables scalable and affordable thermal sensors that may be flexible, lightweight and biocompatible, opening the door for wearable applications.

This doctoral research focused on the development of printed thermoelectric sensors using graphite-based materials. Sustainability considerations guided the choice of substrates, solvents, and encapsulating materials. The results show that graphite flakes can be used as purchased, yielding planar, vertical, and planar/vertical thermoelectric architectures, capable of containing multiple elements in series, which increases the signal output. The formulated cellulose-based inks can be printed directly onto untreated flexible substrates (paper and fabric). Sensors were also obtained using silicone elastomer-based composites, allowing for significant design flexibility and substrate absence. It was possible to achieve touch sensors with fast response times (bellow 1 s) and to have a V_{ON} optimization surpassing 4.5 mV (when connecting multiple elements in series, in ~1.5 cm^2) and high SNR values (above 300 for EC/G_{Flakes} and up to 170 for PDMS/G_{Flakes}). Regarding the planar sensors made with EC/G_{Flakes}, the printed elements were evaluated and approved for flexible applications, with curvature radii down to 3.5 mm.

At its core, this research addresses the urgent need for versatile and sustainable sensing solutions in the era of the 'Internet of Things', showcasing advancements in the field through innovative material applications and low-energy consumption production techniques.

Keywords: Thermoelectric; Printing Techniques; Flexibility; Low-cost; Sustainability

RESUMO

A "Internet of Things" tem promovido o desenvolvimento ~~e integração~~ de soluções económicas, biocompatíveis, flexíveis e leves que satisfazem as necessidades de conetividade universal, incluindo funcionalidades de sensorização. Adicionalmente, a sustentabilidade ambiental enfatiza a importância da escolha de materiais ecológicos e técnicas de produção energeticamente eficientes. Embora os materiais termoelétricos sejam frequentemente promovidos como uma fonte de energia verde, também podem ser usados em aplicações sensíveis à temperatura, detetando e medindo pequenos estímulos térmicos, como o toque humano. A combinação de materiais termoelétricos sustentáveis com técnicas de impressão permite a produção escalável de sensores térmicos economicamente acessíveis, flexíveis, leves e biocompatíveis, apropriados para aplicações "wearable".

Este trabalho de doutoramento centrou-se na produção de sensores termoelétricos impressos à base de grafite. A sustentabilidade foi considerada na escolha de substratos, solventes e materiais encapsulantes. Os resultados mostraram que flocos de grafite podem ser usados conforme adquiridos, originando arquiteturas termoelétricas planares, verticais e planares/verticais, podendo conter vários elementos em série, o que permite um aumento do sinal de resposta dos sensores. As tintas formuladas à base de celulose podem ser impressas diretamente em substratos flexíveis não tratados (papel e tecido). Os sensores produzidos com compósitos à base de elastómero de silicone mostraram uma grande liberdade de geometrias e a possibilidade de ausência de substrato. Foram obtidos sensores com tempos de resposta rápidos (abaixo de 1 s), passíveis de alcançar uma otimização de V_{ON} superior a 4,5 mV (ao conectar vários elementos em série, em ~1.5 cm^2) e altos valores de SNR (acima de 300 para EC/G_{Flakes} e até 170 para $PDMS/G_{Flakes}$). Os sensores planares feitos com tintas de EC/G_{Flakes} foram testados e aprovados para aplicações flexíveis, com raios de curvatura de até 3.5 mm. Na sua essência, este trabalho abordou a necessidade premente de soluções de deteção versáteis e sustentáveis na era da "Internet of Things", apresentando inovações no desenvolvimento de materiais amigos do ambiente e uso de processos com baixo consumo energético.

Palavras-chave: Termoelétricos; Técnicas de impressão; Flexibilidade; Baixo-custo; Sustentabilidade

CONTENTS

LIST OF FIGURES

Appendices

LIST OF TABLES

Appendices

LIST OF ACRONYMS

ASSIST	National Science Foundation of Advanced Self-Powered Systems of Integrated Sensors and Technologies
BSE	Backscattered Electrons
CA	Contact Angle
CENIMAT	Centro de Investigação de Materiais
CEMOP	Centre of Excellence in Microelectronics, Optoelectronics and Processes
CNT	Carbon Nanotubes
Cot	Cotton
CR	Curvature Radius
CRM	Critical Raw Material
DAA	Diacetone Alcohol
DMF	Dimethylformamide
DMS	Dimethyl Sulphide
DSC	Differential Scanning Calorimetry
E	Energy
EC	Ethyl Cellulose
EDS	Energy Dispersive Spectroscopy
EVA	Ethylene-Vinyl Acetate
FPC	Flexible Printed Circuit (commercial)

FTEG	Flexible Thermoelectric Generator
G	Graphite
GPS	Global Positioning System
HDPE	High-Density Polyethylene
IoT	Internet of Things
IoH	Internet of Humans
LCA	Life Cycle Assessment
NMP	N-Methyl-2-Pyrrolidone
ns-FTEG	Non-stretchable Flexible Thermoelectric Generator
OL	Overload
OP	Office Paper
OrgCot	Organic Cotton
PCM	Phase-Change Material
PDMS	Poly-(dimethylsiloxane)
PE	Polyethylene
PEDOT	Poly(3,4-ethylenedioxythiophene)
PEN	Polyethylene naphthalate
PET	Polyethylene Terephthalate
PI	Polyimide
PLA	Polylactic Acid
PF	Power Factor
PS	Polystyrene
PSS	Polystyrene Sulfonate
PVP	Polyvinylpyrrolidone
RT	Room Temperature
R2R	Roll-to-Roll
SE	Secondary Electrons

SEM	Scanning Electron Microscopy
s-FTEG	Stretchable Flexible Thermoelectric Generator
SL	Sticker Label (paper)
SP	Screen-printing
STA	Simultaneous Thermal Analyser
TC	Thermocouple
TCR	Resistance Temperature Coefficient
TE	Thermoelectric
TGA	Thermogravimetric Analysis
THF	Tetrahydrofuran
TPU	Thermoplastic Polyurethane
UV	Ultraviolet
WTEG	Wearable Thermoelectric Generator
XRD	X-Ray Diffraction
ZT	Thermoelectric Figure of Merit

LIST OF SYMBOLS

γ_{LG}	Liquid-vapor interfacial tension
γ_{SG}	Solid-vapor interfacial tension
γ_{SL}	Solid-liquid interfacial tension
$\dot{\gamma}$	Shear rate
ΔT	Thermal gradient
η	Efficiency (in energy context) or Viscosity (in viscosity context)
θ	Contact angle
μ	Charge mobility
ν	Charge carrier velocity
Π	Peltier coefficient
ρ	Volumetric mass density
ρ_n	Electrical resistivity of the n-type material
ρ_p	Electrical resistivity of the p-type material
τ	Scattering time (in an electronic conduction context)
τ	Shear stress (in a viscosity context)
τ_{fall}	Fall time
τ_{rise}	Rise time
X	Thomson coefficient
$\vec{B}$	Magnetic field

C_{ink}	Carbon ink
E	Energy of the charge carriers
E_F	Fermi energy
f_0	Equilibrium Fermi-Dirac distribution
g	Electronic density of states
I	Current
k	Thermal conductivity
k_e	Thermal conductivity promoted by electrical charges
k_ph	Thermal conductivity promoted by phonons
n	Charge carriers’ concentration
q	Electron charge
R	Electrical resistance
$\mathrm{R_H}$	Hall coefficient
$\mathrm{R_{Sheet}}$	Sheet Electrical Resistance
S	Seebeck coefficient
$\mathrm{S_n}$	Seebeck coefficient for a p-type material
$\mathrm{S_p}$	Seebeck coefficient for a n-type material
t	Time
$\mathrm{T_C}$	Temperature on the colder side
$\mathrm{T_H}$	Temperature on the hotter side
V	Voltage
$\mathrm{V_H}$	Hall voltage
$\mathrm{V_{OC}}$	Open circuit voltage
$\mathrm{V_{ON}}$	On state voltage
$\mathrm{V_{OFF}}$	Off state voltage
$\mathrm{V_{OUT}}$	Output Voltage
$\mathrm{V_{signal}}$	Output Voltage above noise level

$\mathbf{V}_{\mathbf{noise}}$	Output Voltage during resting mode

1

MOTIVATION

Thermoelectric devices collect thermal energy and convert it to "green" electrical power, promote local cooling, heat, and sense temperature. They lack mechanical structures, can be made flexible, and have long operating lifetimes, making them valuable for applications in the Internet of Things and wearable electronics. In theory, thermoelectric materials and devices could significantly contribute to saving the world. However, they present several drawbacks that researchers are still addressing, such as the cost, scarcity, and toxicity of the commonly used thermoelectric materials and the complexity of the production processes. Consequently, there is a need to explore new, more environmentally friendly, and readily available thermoelectric materials, along with innovative production methods.

When the use of low-environmental-impact materials (a consideration that is unfortunately and frequently neglected) is combined with low-energy processes (low processing temperatures, no vacuum systems), the result is a more eco-sustainable device. Even if state-of-the-art performance levels are not achieved in some cases, using greener and low-cost materials and processes is preferable, particularly regarding end-of-life product considerations, recycling, or biodegradability. Furthermore, while the primary goal of this research field revolves around powering society with green energy extracted from an inexhaustible source – wasted heat – requiring high-performance materials (high figures of merit) to decrease payback periods, the reality is that thermoelectric materials can serve other purposes, such as temperature sensing, which requires a different optimization approach.

Recent times have seen a significant surge in the demand for low-energy production techniques and eco-materials, contributing to the increased scientific attention towards printed electronics. Additionally, to make these devices practical for real-world applications, it is essential to ensure their proper and efficient encapsulation, protecting them from extreme environmental and usage conditions. Therefore, developing greener encapsulant materials and encapsulation processes is vital for creating and producing sustainable, flexible electronic devices. Progress in all these areas is highly relevant for advancing sustainable and wearable technologies, including thermoelectrics.

With a background in Materials Engineering and some years of experience in the thermoelectric field, I worked in the search for high performance but toxic and expensive materials, using complex and energy-intensive techniques. I was also involved with a line of research focused on eco-friendly thermoelectric materials, albeit using the same production techniques. Therefore, I found that writing a work plan combining green thermoelectric materials and printing methods was a logical choice regarding sustainability, flexibility, and biocompatibility.

The main goal of this PhD work was to develop TE devices using green materials in a sustainable and economically feasible way, considering the scale-up ability, price, biocompatibility and encapsulation, opening the doors to commercial products in the future. The different tasks of this PhD project were:

- Task 1: Design and development of planar sensors through screen-printing

    - Formulation of printable TE inks based on ethyl cellulose and graphite.
    - Optimization of the printing process for different flexible substrates.
    - Study the morphological, electrical, and thermoelectric properties of the printed elements.
    - Connection of multiple TE elements electrically in series.
    - Performance of bending tests.
    - Achieve coiled architectures (planar/vertical) using arrays of TE elements wrapped up.
- Task 2: Creation of planar and vertical devices based on a PDMS/G composite
    - Evaluate the best composite composition.
    - Production of TE elements using blade coating and film casting.
    - Study different thermal contact areas and thicknesses.
    - Connection of multiple TE elements electrically in series.
    - Performance of bending tests.
- Task 3: Study different flexible encapsulant materials
    - Encapsulation of screen-printed planar TE sensors
    - Encapsulation of blade-coated vertical TE sensor

2

INTRODUCTION

Disclaimer

Some excerpts of this section have been published in the following publications:

Figueira, J.; Bonito, R. M.; Carvalho, J. T.; Vieira, E. M. F.; Gaspar, C.; Loureiro, J.; Correia, J. H.; Fortunato, E.; Martins, R.; Pereira, L. *Screen-printed, flexible, and eco-friendly thermoelectric touch sensors based on ethyl cellulose and graphite flakes inks*. Flexible and Printed Electronics **2023**, 8 (2). https://doi.org/10.1088/2058-8585/acc114.

Figueira, J.; Loureiro, J.; Vieira, E. M. F.; Fortunato, E.; Martins, R.; Pereira, L. *Flexible, scalable, and efficient thermoelectric touch detector based on PDMS and graphite flakes.* Flexible and Printed Electronics **2021**, 6 (4). https://doi.org/10.1088/2058-8585/ac45de.

Figueira, J.; Gaspar, C.; Carvalho, J. T.; Loureiro, J.; Fortunato, E.; Martins, R.; Pereira, L. *Sustainable Fully Printed UV Sensors on Cork Using Zinc Oxide/Ethylcellulose Inks*. Micromachines **2019**, 10 (9), 601. https://doi.org/10.3390/mi10090601.

2.1 Thermoelectricity

The thermoelectric (TE) phenomenon allows the design and manufacturing of devices working with no noise, vibrations, or gas emissions that can be used for thermal energy harvesting and conversion into electrical energy, local cooling or heating, and temperature (T) sensing. They have no moving parts, can be produced in large areas, can be flexible (transparent, if required), and have long operating lifetimes. Unfortunately, these devices are usually associated with a low energy conversion efficiency, and the TE devices with better performances typically use toxic, rare, and expensive materials, making their commercial applications scarce. Furthermore, conventionally used TE materials and devices are brittle, bulky, and rigid [1].

2.1.1 Thermoelectric Effects

One of the effects encompassed by the TE phenomenon opens the door to green energy conversion and heat waste recovery - the Seebeck effect. It was discovered by Thomas Johann Seebeck in 1821, with research efforts being made to take advantage of it producing electric energy. Through this effect, there is a conversion of a thermal gradient (ΔT) stimulus in an electrical voltage (ΔV), due to charge carriers' diffusion along the material, being the Seebeck coefficient (S) the key factor that determines the magnitude of this conversion, as described by **Equation 2.1**:

$$S = -\frac{\Delta \mathrm{V}}{\Delta \mathrm{T}} \quad (V/K) \tag{2.1}$$

This coefficient can also be related to the intrinsic properties of the materials, originating a much more complex formula to determine the S, **Equation 2.2** [1]:

$$S = \frac{k_B}{\mathrm{q}} . \frac{\int \tau \, . \, \nu^2 \, . \, g \, . \, \left(\frac{E - E_F}{k_B \, . \, T}\right) . \left(-\frac{\delta f_0}{\delta E}\right) dE}{\int \tau \, . \, \nu^2 \, . \, g \, . \left(-\frac{\delta f_0}{\delta E}\right) dE} \quad (V/K) \tag{2.2}$$

Where k_B is the Boltzmann constant, τ is the scattering time, ν is the carrier velocity, q is the electron charge (1.602×10^{-19} C), E is the energy of the charge carriers, E_F is the Fermi level, g represents the electronic density of states and f_0 is the equilibrium Fermi-Dirac distribution.

The sign of S is determined by the type of the majority carriers of the material. In a p-type material, its value is positive (S_p), with holes flowing from the hot to the cold side, while in n-type materials, S is negative (S_n) and are the electrons that move in that direction.

The reverse counterpart of the Seebeck effect is called the Peltier effect, in which there is an electrical stimulus and a thermal gradient as an output. It was found by Jean Charles Peltier in 1834, and with it, we can achieve localized heating or cooling, being the Peltier element a standard TE device in scientific laboratories. In this case, an electric current is necessary, which will reorganize the charge carriers within the semiconductor material, creating a temperature gradient in the material [2]. The fact that the TE element cools on one side and heats on the other is related to differences in energy levels in which current flows between the metal contacts and the TE material. In other words, and giving an example of an n-type non degenerated semiconductor, if an electron requires more energy to transit between energy levels (from near the E_F level in the contact to the bottom of the conduction band of the TE material), it will absorb energy from the immediate environment in which the TE element is operating, cooling the transition zone. Conversely, if it is transiting to a lower energy level, excess heat will be released into the surroundings [3]. The Peltier coefficient (π) and S are not independent of each other, as demonstrated by Kelvin's relation in **Equation 2.3** [4]:

$$\pi = S\,.T \quad (V) \tag{2.3}$$

There is a third effect closing the TE phenomenon, the Thomson effect. In the absence of an electric current, heat conduction along the elements of a TE pair results in a uniformization of the temperature distribution within each element. When an electric current is present, the temperature distribution within each element changes, not solely due to the Joule effect, but with an additional variation known as the Thomson effect. This phenomenon depends on the material composing the TE element and its average temperature. The Thomson coefficient (χ) and S are also related through Kelvin's second relation, represented by the following **Equation 2.4** [4]:

$$\chi = T\,.\frac{dS}{dT} \quad (V/K) \tag{2.4}$$

Thermoelectric devices are heat engines, and a consequence of this is that the maximum efficiency is limited by the Carnot efficiency (**Equation 2.5**):

$$\eta = \frac{T_H - T_C}{T_H} \tag{2.5}$$

This dictates that energy can only be harvested from the temperature gradient between the hot side (T_H) and the cold side (T_C) - energy cannot be harvested from the background temperature [5].

2.1.2 Figure of Merit and Power Factor

A thermoelectric generator (TEG) is a solid-state device that can convert a temperature gradient into electricity, and a TE material's overall efficiency in this conversion is given by the dimensionless figure of merit, ZT, defined as (**Equation 2.6**):

$$ZT = \frac{\mathrm{S}^2 \,.\, \sigma \,.\, \mathrm{T}}{k_{ph} + k_e} \qquad 2.6$$

where σ is the electrical conductivity, k_{ph} and k_e are the lattice and the electronic thermal conductivities, respectively, at a thermodynamic temperature, T [1]. The lattice *k* refers to phonons (quantise lattice vibrations that conduct heat), while electronic *k* is the component referent to the thermal energy carried by electrical charges (including contributions from both electrons and holes) [6].

For the ZT enhancement, TE materials must have high electrical conductivity and low thermal conductivity ($k = k_{ph} + k_e$), as represented in **Figure 2.1**. This makes electrically conducting metals inappropriate for TE applications due to their high thermal conductivities and low Seebeck coefficients.

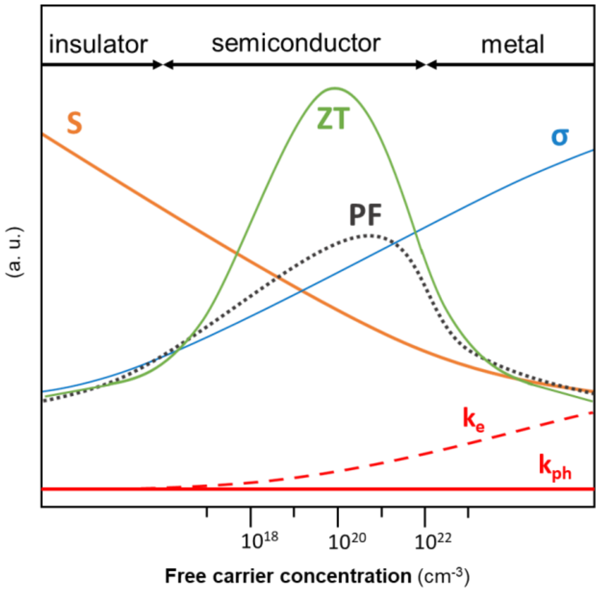

Figure 2.1 - Dependence of Seebeck coefficient, electrical conductivity, and thermal conductivity on the concentration of free carriers. The expected variation of the thermoelectric power factor and figure of merit are also plotted. Adapted from [7], [8].

In case thermal conductivity data for a given material is not available nor possible to measure, the TE quality of a material can be assessed by the power factor (PF) given by **Equation 2.7**:

$$PF = \mathrm{S}^2 \,.\, \sigma \quad (\mathrm{W}.m^{-1}.K^{-2}) \qquad 2.7$$

Of course, this is an incomplete overview of the TE characteristics. Still, researchers can use it to compare results between different materials, especially if they know that the thermal conductivities do not differ significantly.

Generally, a material that is a good electrical conductor is also good at conducting heat since both charge carriers and phonons carry thermal energy. Following the Wiedemann-Franz law, σ is proportional to the electronic component of thermal conductivity, which counteracts each other regarding ZT. This has led to slow progress in improving ZT, with heavily doped semiconductors striking the best balance between the interrelated material parameters [5], corresponding to the maximum of the green curve in **Figure 2.1**. Also, the inverse relationship between S and σ complicates the design of organic semiconductors for TE applications, and optimizing one condition quite often has a detrimental effect on the other - an ideal TE material should be an electrical crystal to maximize σ and at the same time a phonon glass to minimize the *k* [9].

A TEG often uses a combination of p-type and n-type materials to enhance its efficiency. By connecting both TE materials in series, the two types of charge carriers will move in the same direction, as mentioned, ensuring that the generated voltage from the Seebeck effect is additive. Consequently, when calculating a device's efficiency, it is necessary to determine an 'average' ZT value that takes into account the properties of both materials, **Equation 2.8** [5]:

$$Z\bar{T} = \frac{\left(S_p - S_n\right).\bar{T}}{\left(\sqrt{\rho_n \, . k_n} + \sqrt{\rho_p \, . k_p}\right)^2} \qquad 2.8$$

The maximum power conversion efficiency of a TEG considering the Carnot efficiency and material properties limitations can be estimated using **Equation 2.9** [10]:

$$Z\bar{T} = \frac{T_H - T_C}{T_H} \, . \frac{\sqrt{1 + Z\bar{T}} - 1}{\left(\sqrt{1 + Z\bar{T}} + \frac{T_C}{T_H}\right)} \qquad 2.9$$

For the TEG to become competitive, its ZT must be close to 3, so they can surpass 40% of Carnot efficiency (a value achieved by conventional devices) [11]. From electronics to industrial furnaces, numerous waste-heat sources at low- (<250 °C), mid- (~250-650 °C), and high- (>650 °C) temperatures exist, but TEGs have mostly been explored for waste-heat recovery in mid- and high-T applications such as automotive, engine, and industrial applications with untapped exhaust and process heat because of the potential for appreciable power generation [12].

A ZT~1 was reported at the end of the 1950s in Bi_2Te_3 and PbTe, two of the most extensively studied TE materials of all time, and this value was a practical upper limit for more than 30 years. In the last decade, however, significant improvements in ZT have been reported in materials such as TaFeSb with a ZT of 1.5 at 700 °C, $Cu_2S_{0.52}Te_{0.48}$ with a ZT of 2.1 at 727 °C, PbTe–SrTe with a ZT of 2.5 at

650 °C, and SnSe with a ZT of 2.7, also at 650 °C [1], [5], [13]. **Figure 2.2** - **(a)** shows the progress of some of these maximum ZT in bulk inorganic systems achieved over time, emphasising the diversity of chemical systems and mechanisms that have shown high performance, as well as the T corresponding to those results. The ZT values of typical inorganic TE materials have surpassed the unity and are now approaching 3, the critical value for energy conversion efficiency explained previously. Unfortunately, as mentioned before, these materials have scarcity and toxicity issues, and most of the best results are for very high working T, which is far from being compatible with wearable technology. Besides, such inorganic materials usually have problems regarding their heavy weight, high cost, and processing conditions [1], [14], [15].

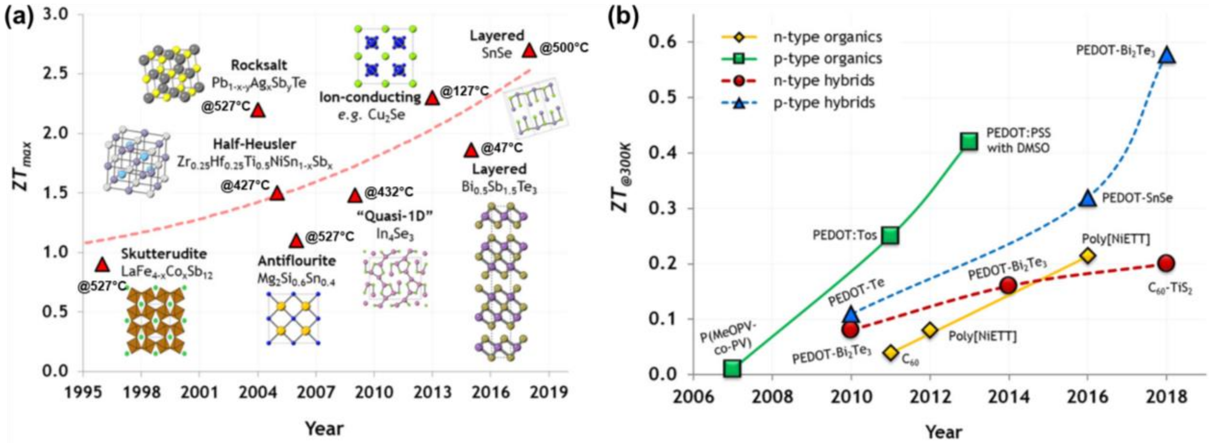

Figure 2.2 - Progress over time of: **(a)** maximum ZT in bulk inorganic systems (for different medium temperatures) and **(b)** ZT at room temperature in p- and n-type organic materials and organic-inorganic hybrid systems. Adapted from [1], with the permission of AIP Publishing.

Polymer-based organic TEGs, which contain unique merits such as low cost, lightweight, convenient processing, mechanical flexibility, and low thermal conductivity, have been promoted as a new generation of thermoelectric candidates [16]. In **Figure 2.2 - (b)**, we can see the progress of ZT at room temperature (RT) in p- and n-type organic materials and organic-inorganic hybrid systems over time, highlighting the rapid advancements in materials based on poly(3,4-ethylenedioxythiophene (PEDOT), a commonly used conductive polymer. Finding organic materials with low k is easy, but with high S values is very difficult, except when considering the incorporation of metal or metal oxide particles into a matrix, achieving hybrid composites with properties from both "worlds". Although the research community has paid a lot of attention to this "new" TE route, and many review articles have been published in the field of organic, soft, flexible, and printable thermoelectrics [9], [14], [16], [17], most of them are far from being usefully employed or applied owing to their low thermoelectric efficiency or ZT value.

2.1.3 TEGs Architectures and Configurations

Similar to other research fields, the advancement in thermoelectric science is based on different pillars critical to the devices' final performance. The choice and optimization of the TE materials is crucial. Still, other aspects, such as the adopted elements geometries and devices architecture, the used substrates, gap fillers, and electrical connections, also play an important role, and thermal and structural design analysis of the TE device must be carried out [18].

A TE device can have different types of structures and geometries that can be produced through several techniques - it is a world of numerous possibilities. In terms of structure, the thermocouples (TCs) can be assembled in two main configurations (**Figure 2.3**), depending on the direction of heat flow regarding the substrate plane. A third possible configuration is the combination of both, i.e., a vertical/planar design, where TE elements are plainly produced but vertically assembled at the end of the process. The designs development from planar to vertical heat flow is driven by the improved thermal contact (proportional to the contact surface area) to the heat source (hot side) and sink (cold side) that may be achieved with a vertical design [19]. All the configurations assume that the individual TE elements are arranged thermally in parallel but electrically in series.

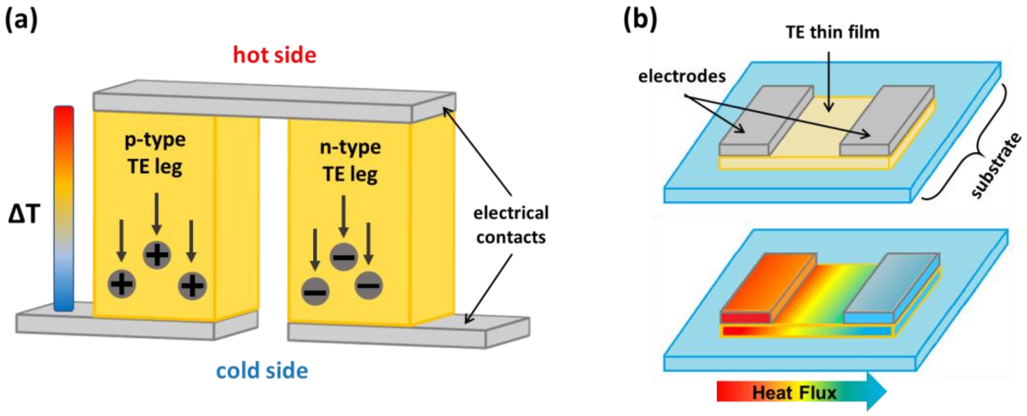

Figure 2.3 - Examples of TE elements designs: **(a)** a thermocouple in a vertical geometry, where the heat flows perpendicular to the substrate and through the TE legs, explaining the majority carriers movement with the temperature gradient, and **(b)** a single element in a planar geometry, where the heat flux occurs along the film and parallel to the substrate.

Traditional TE devices are constructed from bulk materials shaped into small millimetric scale blocks and subsequently arranged into TE modules. A thermocouple is one pair of n- and p-type TE legs, and a module generally has several couples. The typical structure employed in these systems is a vertical/vertical architecture (**Figure 2.3** - **(a)**), commonly referred to as π architecture. To obtain these vertical/vertical structures, which are usually thicker than the planar ones because of the heat flux direction, techniques like mechanical alloying and spark plasma sintering [20], electrochemical deposition and photolithography [19], [21], dispenser printing [22], [23], blade/spatula-coating [24], [25] or 3D-printing [26]–[28] can be used.

Film-based manufacturing techniques also opened the possibility of utilising in-plane, or planar/planar architectures (**Figure 2.3** - **(b)**). In such structures, the thermal flux no longer passes from the top face to the bottom face through the TE legs but instead flows parallel to the film and its substrate. Significant losses can be encountered if the thermal conductivity of the substrate is comparable to that of the thermoelectric materials [29]. To build planar/planar structures, several thin-films and micro-films deposition techniques can be used, such as sputtering [30], plasma enhanced chemical vapor deposition [31] or resistive thermal evaporation [32], which need controlled environments and are most of the times complex methods, or such as screen-printing (SP) [33], [34], roll-to-roll (R2R) [35], [36], spin-coating [37], [38] or even spatula/blade-coating [39]–[41], which are simpler and faster techniques. Although planar TE devices are usually less efficient than vertical ones, their advantages are linked to the possibilities of large area applications, flexible and transparent devices, and less materials required to produce them.

Regarding the electrical conduction type, instead of using TE couples constituted by p- and n-type pairs, it is possible to use only either the n-type or p-type material [10], [25], [26], [36], [42]–[45]. Some examples of single-type TE legs in both planar and vertical architectures can be seen in **Figure 2.4**. The individual TE elements can still be linked thermally in parallel and electrically in series, with the electrical connections running "top-to-tail", linking the hot and cold sides of the TEG [29].

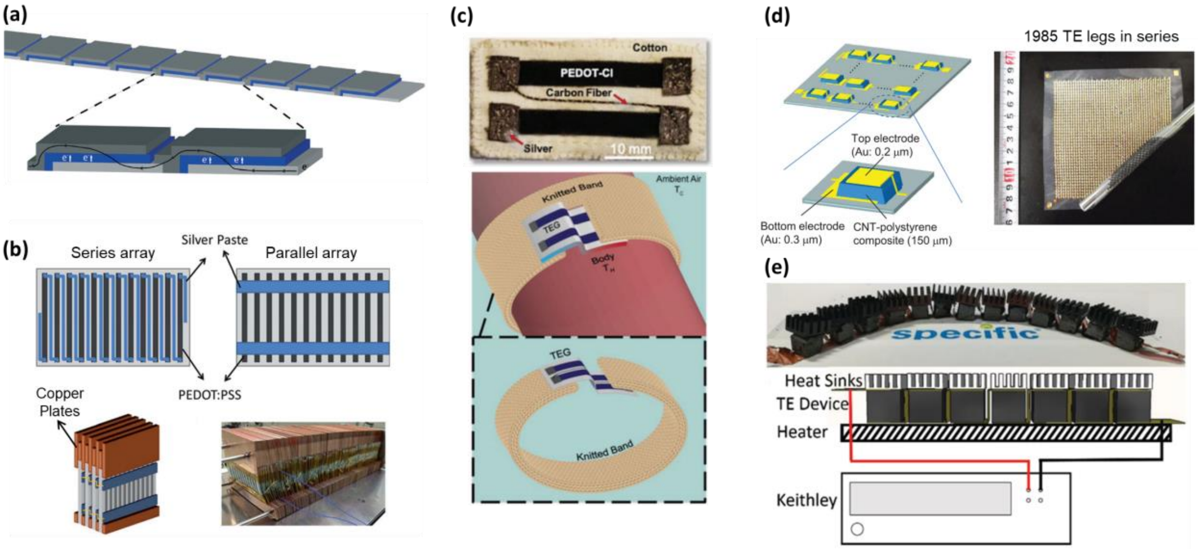

Figure 2.4 - Literature examples of single-type TE arrays: **(a)** poly(3,4-ethylenedioxythiophene) polystyrene sulfonate (PEDOT:PSS) and silver printed by R2R on polyethylene terephthalate (PET) foil [36], **(b)** PEDOT:PSS and silver blade coated on paper [10] - copyright 2014, The Royal Society of Chemistry, **(c)** PEDOT-Cl by vapor print on cotton with carbon fiber thread as interconnection [43] - copyright 2019, John Wiley & Sons, Inc., **(d)** carbon nanotubes and polystyrene (CNT-PS) composite deposited by spatula coating on polyethylene naphthalate (PEN) with vacuum deposited gold as electrodes - reprinted from [25], with the permission of AIP Publishing., and **(e)** SnSe 3D-printed TE ink with copper tape as interconnection [26].

A TEG is usually a more extensive system than a module. In a common TEG, the modules are connected thermally in parallel with heat exchangers to transfer heat from the heat source to the module's hot side and away from its cold side. The modules are connected to an electrical load to close the circuit and enable electricity extraction [12]. Parallel to the TE properties, three factors turn out to be crucial for the TEG performance: increasing the thermal resistance of the generator, decreasing the thermal resistances of the package and the contact to the heat source and sink, respectively, and finally, minimizing the electrical resistance of the contacts between thermocouples. These goals may be achieved through both design and material selection [46]. There are several published works with simulation results around the optimization of the TE legs geometries and the device's architectures, some of them considering the other components [23], [24], [47]–[53].

2.1.4 Wearable Thermoelectric Generators

Within ,the Internet of Things (IoT), there is an emerging class of devices worn in, on and around the human body and can sense, record and exchange data with surrounding networks. Wearables and other human-centered devices can be summarized as the Internet of Humans (IoH), and wearability, alongside big data, cost and energy, represent the fundamental challenges in the implementation of IoT and IoH. The IoH includes sensors that measure body activity, biopotentials, biomarkers and many other parameters, and smart implants or actuators that dispense medication or provide electrical stimuli [54].

One of the major challenges of these wearable devices concerns their powering/charging because there is a limited number of devices a user will charge daily, making charging a potential market killer. Also, the chemical batteries will typically fail and need replacement after a finite time, thus requiring new batteries and extra labour, which is sometimes inconvenient or even impossible [55]. Researchers are developing novel power supply methods adopting energy harvesting to overcome this limitation of batteries. However, these sources are not always suitable for wireless and portable electronic equipment because of their operating mechanism, cost, and size. Therefore, TE power generation is receiving considerable attention from researchers both in academia and industry as a possible green energy solution to address this need [56].

These energy harvesters have been designed and fabricated over the years to fit different application areas, and at ASSIST (National Science Foundation of Advanced Self-Powered Systems of Integrated Sensors and Technologies), a TEG is one of the enabling technologies being explored to create wearable, self-powered, health and environmental monitoring systems [57]. Wristwatch/GPS (Global Positioning System), hearing aid, pacemaker, ozone sensor, and fitness trackers (GPS with health monitoring system) are some examples of applications that can benefit from TEG due to their low power requirement (< mW) [56]. Unfortunately, as already mentioned, the most efficient known TE materials are toxic, rare, and expensive, so it is very important that the TE community continue the search for alternative materials. Also, an energy harvester cannot simply replace batteries; it will require a complete system redesign, smart power management, and production cost reduction [58].

The nature of the thermoelectric materials to be used depends on the temperature gradient the TE device is submitted. In applications like wearable electronics, TEGs are expected to harvest energy in a low-temperature (around RT) context and convert it into an electrical current. Therefore, wide-area, low-cost, biocompatible, and mechanically flexible TEG (FTEG) are strongly desired to collect such low-density heat fluxes cost-effectively [49]. The FTEG can make conformal contact with the human skin and fully utilize body heat with minimal energy loss while also being comfortable to wear. However, state-of-the-art TE devices, including TE materials and thermal and electric interfaces, are mostly optimized for technical performance and do not consider wearability. This means that rigid and heavy components and/or toxic or irritating materials are being studied. Current approaches mainly investigate individual components of wearable devices, but to optimize wearability and performance, a holistic system optimization from the human body to a specific application should be considered [54].

In a recent review [59], S. Zhu et al. provide an overview of the state-of-the strategies aimed at achieving flexibility and high normalized power density in TEGs based on inorganic bulk TE materials. The focus on these materials relies on their significant potential as power sources for wearable electronic devices due to their high output. The performances of rigid TEGs (r-TEGs) and flexible TEGs, the latter divided into the non-stretchable FTEGs (ns-FTEGs) and stretchable FTEGs (s-FTEGs), are summarized in **Table 1**, where the used materials to fabricate them are explicit.

Regarding electrodes, some flexible approaches could have deposited the TE legs into a polymer matrix, but interconnects and packaging made from rigid materials limited the flexibility and number of bending cycles [54]. There are some published works with flexible interconnects made with thin copper films, strips, or foils, and made with silver paste, foils, or coated fibers [22], [24], [60], besides the commercial interconnects. Printing techniques can be used to obtain electrodes and conductive paths using silver, carbon, copper, or nickel inks. To solve the problem of mechanical failure between thermocouple and interconnect while bending, some researchers propose liquid metal in a PDMS channel as an interconnect [54], [61], [62].

The thermal resistance of the ambient air can be decreased using heat dissipators like radiators. The outer surface of a device itself may serve as a dissipator, but for more effective heat exchange, a radiator made with aluminium or copper fins or pins, for example, can be provided. This way, the contact surface to the air exceeds the area of the skin occupied by the device, thereby virtually decreasing the thermal resistance of the air (thermal insulant) per square centimeter of skin and increasing the heat flow through the TEG [63]. However, standard fin or pin type metal heat sinks are typically adopted from electronic chip cooling, an application where flexibility and weight are not important issues. Flat heat sinks fabricated from porous materials with a large surface area, but low volume can be used to increase wearability. Alternative approaches using (micro-)fluidics or liquid-solid phase change are very effective in removing heat from the TEG but require a large-area interface to the environment. Flexible or stretchable heat sinks are most promising for future wearable harvesters [64],

[65]. To avoid uncomfortable skin cooling in changing ambient conditions, an ideal heat sink should adopt its thermal resistance accordingly [54].

Table 1 - Performances (ZT and Power Density, for a specific temperature) and features (thermoelectric materials, encapsulants and heat sinks) summary for different types of wearable TEGs (WTEGs). Adapted from [59].

TEG Type	**TE Legs Material**	**ZT or Efficiency**	**Encapsulation**	**Electrodes**	**Ambient Temperature**	**Heat Sink**	**Power Density** (μW/cm^2)	**Ref.**
r-WTEG	Bi_2Te_3	0.8	PDMS/Alumina	Copper	18 °C	heat spreader	6	[57]
r-WTEG	commercial Bi_2Te_3	-	Alumina	Copper	22 °C	plate fin heat sink	20	[63]
r-WTEG	commercial Bi_2Te_3	-	Ceramic	Copper	23 °C	plate fin heat sink	28.5	[66]
r-WTEG	Bi_2Te_3	0.14	AlN	Copper	17 °C	plate fin heat sink	35	[67]
r-WTEG	Bi_2Te_3	-	AlN	Copper	25 °C	heat spreader	44	[68]
ns-FTEG	commercial Bi_2Te_3	-	PDMS	FPC	13 °C	-	0.084	[69]
ns-FTEG	Bi_2Te_3 (glass fabric)	-	PDMS	Copper	15 °C	-	0.75	[70]
ns-FTEG	commercial Bi_2Te_3	-	-	FPC	19 °C	-	0.4	[71]
ns-FTEG	commercial Bi_2Te_3	-	PDMS	FPC	25 °C	-	0.526	[72]
ns-FTEG	commercial Bi_2Te_3	-	Polymer	Copper	25 °C	-	2.28	[18]
ns-FTEG	commercial Bi_2Te_3	0.35	PDMS	Liquid metal	5 °C	-	2.5	[61]
ns-FTEG	commercial Bi_2Te_3	0.85	-	FPC	13 °C	-	3.5	[73]
ns-FTEG	commercial Bi_2Te_3	0.71	PDMS	Copper	24 °C	-	4.5	[74]
ns-FTEG	commercial Bi_2Te_3	-	PDMS	Liquid metal	24 °C	-	5.2	[75]
ns-FTEG	commercial Bi_2Te_3	-	Aerogel/PDMS	Liquid metal	24 °C	-	5.4	[76]
ns-FTEG	commercial Bi_2Te_3	-	Melamine foam	Copper	24 °C	heat spreader	7	[53]
ns-FTEG	Bi_2Te_3	-	Bakelite	Copper	24 °C	flexible heat sink	4.78	[64]
ns-FTEG	Bi_2Te_3	-	Bakelite	Copper	24 °C	flexible heat sink	5.6	[65]
ns-FTEG	Bi_2Te_3	-	Bakelite	Copper	24 °C	plate fin heat sink	5.6	[77]
ns-FTEG	Bi_2Te_3	0.75	Fabric	Copper	24 °C	air velocity: 0.2 m/s	6.3	[78]
ns-FTEG	Bi_2Te_3	-	-	Copper	24 °C	plate fin heat sink	8	[79]
ns-FTEG	Bi_2Te_3	-	PDMS	Liquid metal & Copper	24 °C	hydrogel	8.3	[62]
ns-FTEG	commercial Bi_2Te_3	0.75	Porous PDMS	Copper	24 °C	absorbent polymer	9.37	[80]
ns-FTEG	commercial Bi_2Te_3	0.68	Polymer	Copper	24 °C	absorbent polymer	13	[81]
ns-FTEG	Bi_2Te_3	-	-	FPC	24 °C	radiant cooling	12.5	[82]
ns-FTEG	Mg_3Bi_2/Bi_2Te_3	-	Porous PU	Copper	16 °C	air velocity: 1.1 m/s	20.6	[83]
ns-FTEG	commercial Bi_2Te_3	0.64	Polymer	Copper	13 °C	PCM heat sink	20	[84]
s-FTEG	Bi_2Te_3 (PEDOT:PSS)	-	PDMS	Copper	ΔT = 33 °C	-	0.87	[85]
s-FTEG	Bi_2Te_3	-	Elastic fabric	Polyester fiber	ΔT = 33 °C	-	1	[86]
s-FTEG	commercial Bi_2Te_3	-	PDMS	Liquid metal	ΔT = 10 °C	-	4	[87]
s-FTEG	Bi_2Te_3	-	PDMS/Ag-Ni	Ag nanowires	10 °C	-	6.97	[88]

AlN: Aluminium Nitride. FPC: commercialized flexible printed circuit. PCM: phase-change material.

Soft and flexible thermal interfaces for wearable thermal harvesters are barely discussed in literature. Most authors focus on developing FTEGs and applying them directly on the skin without adding another interface [54] meaning that the active harvesting area is often reduced to the contact points between skin and TCs. Packing flexible devices with polyimide foil [45], [69] or with PDMS [89] between the thermolegs and the skin can be a flexible, conformable and biocompatible choice, but these materials are also thermal insulators. As a result, the TEG could adapt to irregular surfaces, but there will be performance losses.

Light-weight materials with high k, such as aluminium or copper [57], [71], are still the gold standard thermal interface to the body in state-of-the-art wearable thermal harvesters. Interfaces are typically sheets with a skin-contact area of one to several square centimeters and a thickness of one to several millimeters. In most harvesters, the interface is larger in area than the TEG to increase the harvesting area. To optimize contact with the surface of the human body, rigid interfaces are typically segmented and then connected individually by flexible links or by integration into a flexible substrate or fabric. Nevertheless, rigid interfaces cannot compensate for smaller surface topography as it occurs nearly everywhere on the body, therefore reducing the actual harvesting area. Additionally, they can cause discomfort for the wearer if the attachment pressure is too high or if only parts of the interface are in contact with the skin [54].

2.1.5 Thermoelectric Sensing Applications

Temperature sensing plays a pivotal role, for instance, in healthcare monitoring applications. Thus, despite the undoubtedly interest in energy conversion, TE materials can be approached from a temperature-sensitive perspective, as they can detect small thermal stimuli, such as a human touch or contact with cold/hot objects.

The body temperature can detect human touch in combination with TE technology. The human body produces heat as a by-product of metabolic chemical reactions. Then, it is distributed to different body parts by the blood flow, releasing it through the skin via radiation, convection, and sweat evaporation [90]. The human body is a heat engine emanating heat in the range of approximately 50 to 150 W/m^2 at regular daytime activities [91]). The temperature difference between the human body and the ambient is usually around 5-15 °C (skin temperature can change from 25 °C to 36 °C at an ambient temperature range of 4 °C to 40 °C [54]). Of course, results are improved when people are warmer, like when they are younger or did exercise, and/or when the environment is cool, for instance, because there is air motion or a heat dissipator attached. However, temperature gradients for energy harvesting will always be small due to human conditions barriers and thermal resistance losses.

These ΔT are usable for determined sensing or detecting applications, where eco-friendly materials, even with lower S, can be used to obtain low-cost and scalable TE devices that will operate close to RT. Such an approach can provide an alternative to conventional capacitive sensing technologies. In a recent review of flexible temperature sensors [92], regarding the resistance temperature sensors (which also work with thermal stimuli), it is stated that there are some critical issues, e.g., cost, resistance temperature coefficient (TCR), oxidation resistance, and manufacturing requirements. Copper, gold, nickel, platinum, and silver are the most used materials. On the other hand, the thermocouples' rugged, low-cost, and self-powered properties make them preferable for having stable reference temperatures. However, due to their continuous exposure to sudden environmental changes, their use as a wearable sensor is limited (which is not the aimed application of this work). Moreover, concerning pressure and capacitive sensors, a fair comparison is not applicable since the stimuli are of different nature, the performance is evaluated differently, and the applications can diverge (for example, TE thermal sensors can be on one side of a glass window of a laboratory door and be stimulated directly touched or touched through the glass on the opposite side of the door).

The growing integration of sensors due to the increasing number of touchscreen displays and devices boosts the global touch sensor market growth. Therefore, it is necessary to search for biocompatible, flexible, lightweight, and low-cost materials and develop technologies compatible with low-intensity stimuli, like low temperature or low pressure. Moreover, the global TE generator market was valued at 472.5 million USD in 2020 and is projected to reach more than 1440 million USD by 2030, growing at a compound annual growth rate of 11.8% [59]. Thus, there is a window of opportunity for TE materials, not only for energy harvesting and conversion but also for T sensing, such as T sensors or touch detectors [93]–[97]. The device's output power is not always a priority in these types of applications. Therefore, the achievement of flexible, green, lightweight and/or low-cost devices can be considered.

Although a TE energy harvesting device is conventionally evaluated via TE figure of merit ZT, the TE sensing capabilities are poorly compared via these indicators because their performance is determined mainly by the S of the active materials and the *k* of the complete set of the device components [98], [99]. Thus, if low k TE materials and substrates are used, as well as integrating TE elements with little S in series, the production of TE sensors and detectors with relevant performances can be attained.

2.1.5.1 Thermoelectric Touch Detectors

When touched, a TE detector transforms the thermal gradient between the skin and the detector into an electrical signal. Among several desirable features, this device must exhibit a strong sensing performance, including high and stable signal-noise ratio (SNR) values with short response time. It should also present suitable mechanical properties concerning the final application, and, equally important, it needs to be cost-effective and viable for large-scale production [100].

Besides the possibility of flexibility and lightness, the TE sensors offer good performance for both naked and glove-covered fingers as they work with the ΔT formed between the finger and the device. This feature could be interesting in several situations, such as industrial processes, patient-care activities, and laboratory safety, especially in a pandemic like the recent one we experienced. As a main advantage, over the existing touch sensors, a single TE element can distinguish a different finger

T, sense, and discriminate between fast and slow touches, and give two symmetrical responses depending on the stimulated electrode, allowing for a Yes-No/On-Off applications.

Concerning TE sensors and detectors, one of the primary considerations is the optimization of the material's thermal conductivity. Since our goal is to heat only one side of the material and maintain a sufficient ΔT over time to generate a ΔV response, keeping the k as low as possible is crucial. Otherwise, heat would readily flow from the heated side to the other. Another challenge is fabricating TE materials with a suitable size and shape to match the geometry of the heat sources [101]. However, contrary to energy harvesting applications, these detectors only need short thermal stimuli to work properly (therefore, the ability to work in a non-stop mode is not mandatory), and thermal losses are less important. Depending on how large the Seebeck potential of the chosen material is and how low the thermal conductivity of the device is, these detectors can have different discriminated output levels. They can quickly evolve to work from detectors to sensors. Additionally, responses to T changes should be precise and rapid, which depend on the S (material property), translating directly into high signal levels for thermal sensing. The number of connected elements (device architecture) also plays a role in this context. Moreover, high electrical conductivity reduces the Joule heating and increases the TE voltage generated [95], [98], [102].

From the electrical point of view, a detector should have a V_{signal}:V_{noise} ratio of at least 3:1 [103] or even 5:1 [104] to maintain a robust operation, where V_{signal} is the output voltage (V_{out}) above the noise level, when stimulated, and the V_{noise} is the background noise (standard deviation of the signal during resting mode). Several researchers have reported SNR of up to 35 for TE detectors, choosing different materials and techniques. M. Ruoho et al. [95] reported a TE touch panel based on Al-doped ZnO active material with a SNR of 20 and a rise time of 90 ms. A similar SNR value was reported by E.M.F. Vieira et al. [105] for 60 nm - SnO_x thin films with a fast fingertip touch event. The author of this thesis reported an SNR of ~ 10 for a 60 nm thick-Cu_2O film [32]. Recently, T. Koskinen et al. [99] presented a high SNR of 35 for a touch-sensing device made of multilayer graphene ink. This SNR range enables the detection, without any doubt, of individual touches. However, most of these state-of-the-art results come from highly costly techniques (vacuum deposition systems, high-temperature processes) and/or rigid substrates.

2.2 The Need for Sustainable Materials and Production Methods

In 2019, the European Chemical Society published a special periodic table to highlight the relative scarcity of important elements like zinc, gallium, germanium, silver, indium, tellurium, and yttrium. Besides the elements' scarcity issues, this table notes 30 chemical elements used to produce a typical mobile phone. The 2019 version table was already updated twice, in 2021 (mainly because of lithium) and 2023 (due to a change in carbon), with the 2023 version being compared to the first edition in

Figure 2.5. Although making accurate predictions is difficult because technological advances can change the overall scenario, it is fair to state that, unless solutions are provided, there is a risk of seeing many of the natural elements that make up the world around us run out – whether because of limited supplies, their location in conflict areas, or our incapacity to fully recycle them [106].

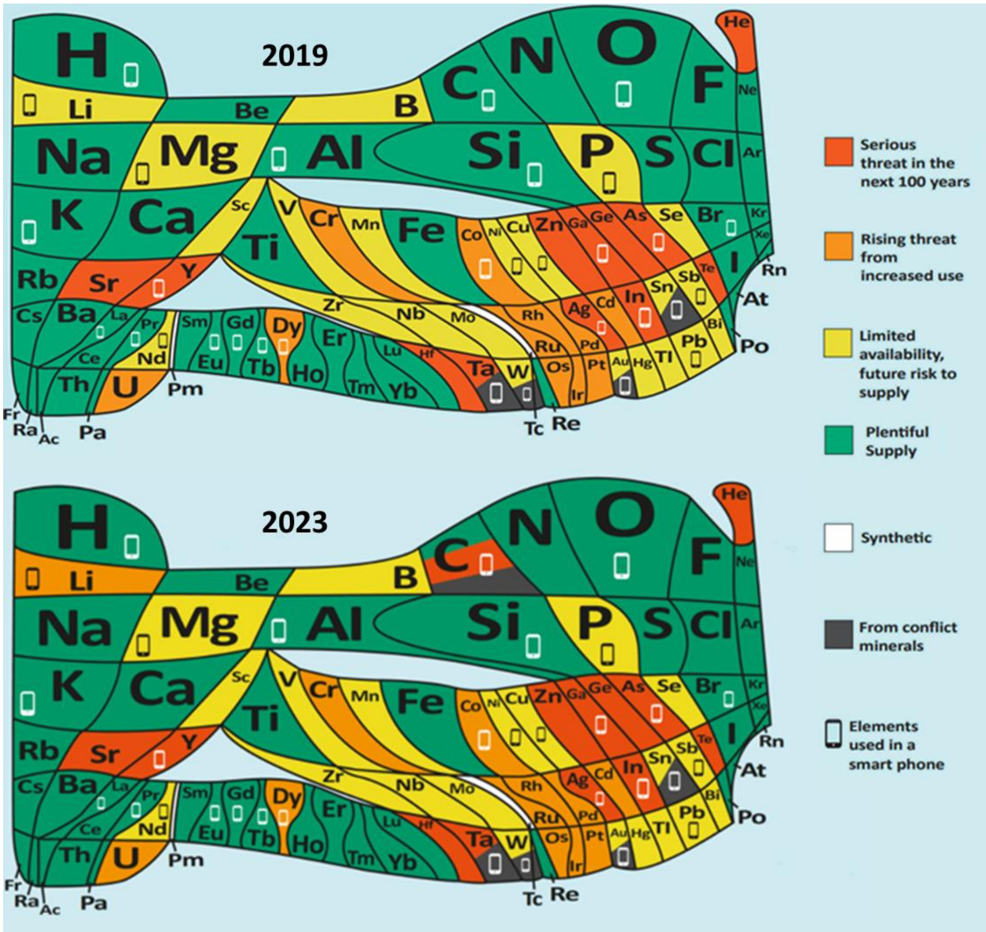

Figure 2.5 - Periodic tables with 90 elements, highlighting their scarcity and nature through a colour code, and referring the elements commonly used for the production of a smart phone, from EuChemS. Both 2019 and 2023 versions are presented for comparison [106].

The term “critical raw materials” (CRMs) refers to various metals and nonmetals that are crucial to Europe’s economic progress and of high importance to the global economy [107]. Some of the used CRMs, see **Figure 2.6**, especially in biomedicine, aerospace, electric vehicles, and energy applications, are almost irreplaceable. However, there is always room to improve and innovate technologies and industries. As long as understanding and adherence to sustainability priorities are maintained and staying vigilant not to cross ethical or risk boundaries, science continually unveils ingenious solutions to address complex problems. Nonetheless, the challenge often hinges on timing, with these solutions occasionally arriving too late, necessitating confrontation with advanced and irreversible consequences stemming from the prevailing issues.

Contemporary research needs to respond and adapt to the possibility of future governmental guidelines prohibiting the use of heavy compounds, toxic solutions, and so forth. Thus, the TE field should always consider global material management roadmaps for the near and distant future. Exploring efficient scaling-up techniques with low energy requirements and rapid steps is as important as having all the device components made with non-toxic or rare resources. Therefore, it is desirable that the whole device is designed per these propositions, and different options should be evaluated to better understand how to take advantage of the TE phenomenon.

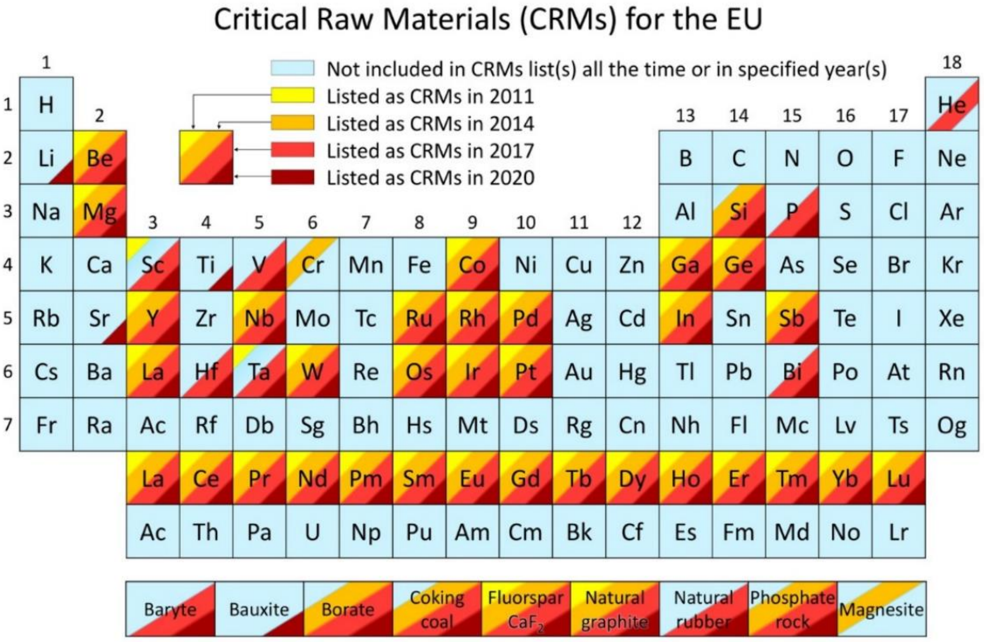

Figure 2.6 - Critical raw materials list for the European Union, gathering data from 2011 to 2020, overlaid on the periodic table of elements, using a colour code to depict the evolution of criticality over time [107].

2.2.1 Eco-friendly TE materials

Most inorganic semiconductors, such as SnSe, Bi_2Te_3, SiGe, SnS, and $CoSb_3$, exhibit excellent TE performance and have been widely explored for the recovery of waste heat at temperatures above 250 °C. Still, they are expensive, have a relatively heavy weight, have strong toxicity, and are complex to process [108]. Moreover, approximately 50% of waste heat is stored below 250 °C and is available on large surfaces, meaning that large areas of processed TE material could recover this lost energy. Printed TEGs formed from lightweight and low atomic mass elements like carbon, nitrogen, or sulphur have the potential to offer a more environmentally sustainable economy compared to devices made from less abundant Earth minerals such as germanium, selenides, and tellurides [5]. In **Figure 2.7**, some examples of soft materials with TE properties are made from abundant and less toxic elements. They are lightweight and can be processed from solution, making it possible to deposit the materials over large areas using cheap printing techniques and flexible substrates. This allows the TE devices to be applied on curved surfaces like wrist-wearables. However, far fewer TE materials have been developed to efficiently recover such small temperature gradients at temperatures as low as 40 °C [9].

The category of soft materials exhibits distinct mechanical properties, including high deformability and low stiffness. However, some other materials and composites can be readily tailored for flexible applications and wearables. The development of printable inks with flexible substrates opens possibilities for creating conformable and biocompatible devices, utilizing soft materials or other materials that offer interesting characteristics, whether in a 2D geometry or composite form. The formulation of printable TE inks, both organic and inorganic based, is indeed a potential route to achieve flexible devices, with the opportunity to scale up their production.

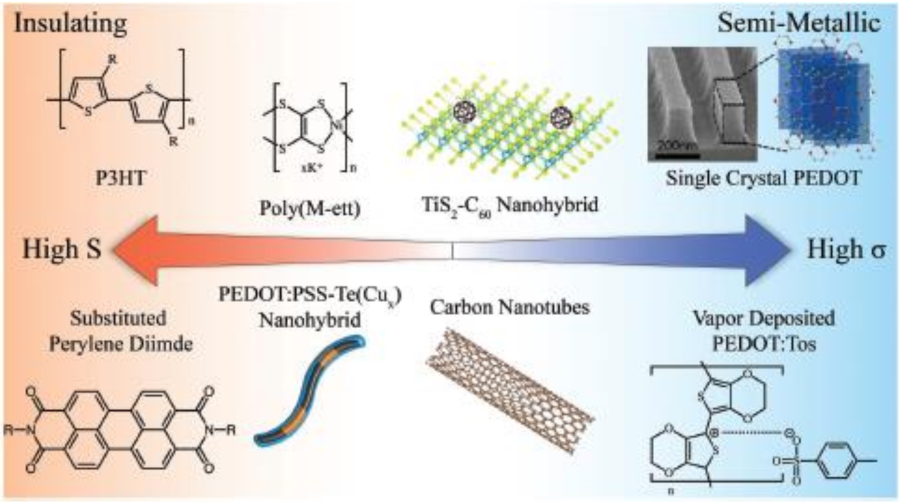

Figure 2.7 - Soft materials exhibit a range of TE properties, from insulating to nearly metallic. High-conductivity materials are characterized by high degrees of order and crystallinity. In contrast, lightly doped, polycrystalline materials demonstrate high Seebeck coefficients, the trade-off of properties already addressed [109] - copyright 2019, John Wiley & Sons, Inc..

Carbon-based pastes and inks are used extensively in various printed, electronic devices, including resistive heater panels, electrochemical sensors, pressure sensors, printed batteries, and supercapacitors [110]. The advantages of carbon include low production cost, disposability, chemical inertness, the ability to be modified or functionalized for electrochemical sensors, and the ability to be used as an intercalation material in energy storage [111]. These can then be dispersed in a viscous carrier fluid to create inks and coatings for various applications, including printable electronics, sensors, smart packaging, and active coatings. However, carbon inks usually present a very low S, which is unsuitable for TE applications.

Graphite (G), a carbon allotrope, is an essential material for scientific and industrial applications because of its peculiar properties: it is highly resistant to heat, almost inert when in contact with virtually any other material, and has good thermal and electrical conductivity [112]. Among other carbon-based materials, G is known to have a TE response but with a relatively small S, compared to more established TE materials [98]. However, reports are showing that some of these materials can perform better than standard organic conducting counterparts such as PEDOT:PSS since the S is sometimes more significant and they can sustain higher processing temperatures if needed [101], [108], [113]–[116]. Moreover, compared to carbon nanotubes and graphene, graphite is much cheaper and has attracted the attention of several research groups [116]–[119].

Graphite ink is often used in printed electronics as a material for electrodes [120], [121], but there are published works using it in the TE field [113], [116], [122] and also on strain and temperature sensors [123], [124]. During this PhD work, graphite flakes were used to produce TE sensors through two different approaches: the formulation of screen-printable inks ethyl cellulose (EC) based, see **Chapter 4**, and the production of a composite with polydimethylsiloxane (PDMS), see **Chapter 5**. More details about PDMS can be found in **section 2.3.1**.

Molybdenum disulfide (MoS_2) is a 2D transition-metal dichalcogenide that is non-toxic and contains earth-abundant elements. This material has shown great potential in various applications such as TE power generation, photodetectors, field-effect transistors, and electrochemical storage in supercapacitors. MoS_2 is a good candidate for TE mainly because of its inherent low thermal conductivity, and it has been used to enhance the ZT of different materials by making nanocomposites, for instance, with TiS_2, Bi_2Te_3, PEDOT: PSS, $CoSb_3$, Au and RGO [125], [126]. Featuring a metastable metallic phase (1T), which can be stabilized or converted to a stable semiconductor phase (2H) by the appropriate heat treatment or use of microwave radiation, MoS_2 has unique characteristics, such as high carrier mobility, strong electron-hole confinement and variable bandgap [127]. **Section 6.2.1** presents a study about the production of a composite based on MoS_2 and cork for TE sensing applications.

2.2.2 Printing Technologies in TEGs

Despite the growth of market demand in wearables, the need for green energy power sources, and sensors for the devices' operation, using cheap materials in their production will be essential to achieve sustainable and marketable wearable technologies. Furthermore, production methods and techniques should also be eco-friendly and low-cost, enabling scale-up.

Flexible electronics are growing interest among researchers and companies with widely varying applications, such as organic light emitting diodes and transistors, conductive tracks on non-standard substrates, and many different sensors [42]. These applications have pushed the outputs of printing techniques to new levels, making a considerable contribution to reaching economically viable printed TEGs that are more suited to efficiently recovering heat at low operating T and in large areas. In a recent review [5], M. Burton et al. comprehensively discussed the substantial advancements made in printing TE materials across various material groups and printing techniques aiming at TEG fabrication.

As mentioned before, the TE temperature sensing feature offers possibilities for different applications. It can be integrated with scalable and cost-effective, biocompatible, flexible, and lightweight thermal sensing solutions, exploring the combination of sustainable Seebeck coefficient-holding materials with printing techniques and flexible substrates.

2.2.2.1 A Synergy between Research Topics

Printing technologies offer a potential route to produce sustainable TE devices at a lower cost, on a large scale, and allow a tailored architecture to meet the heat source stimulus requirements. A proof of that is the increasing number of publications combining TE devices with wearable applications, flexible, organic, and printed materials [128]. Nowadays, interesting tools help us understand the research trends and what has been done in specific areas, providing a glimpse of what has aroused the interest and dedication of the scientific community. Some research trends results from the Web of Science site search tool, based on the number of publications (manuscripts, books, patents) relative to specific keywords, are shown in **Figure 2.8**.

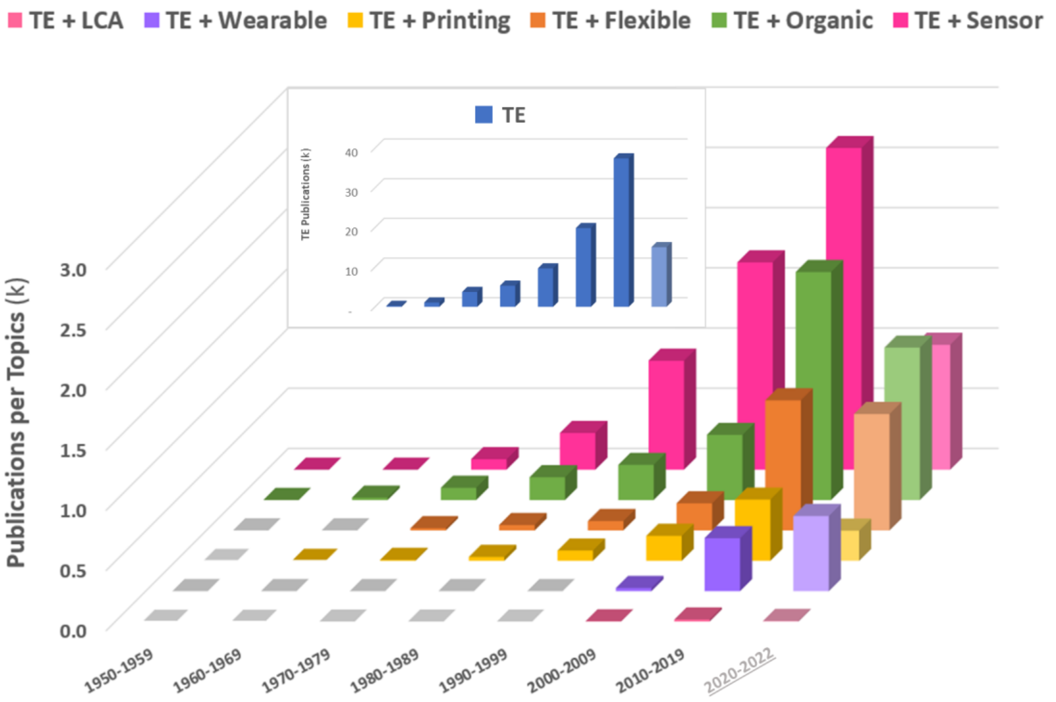

Figure 2.8 - Research trends for specific keywords and time periods given by a Web of Science search tool, where manuscripts, patents, review works and books regarding those topics are accounted for.

Although this type of analysis is not highly accurate (we cannot guarantee that all the databases are included nor check one by one if there are repetitions of sources or a misunderstanding of our search meaning, for example), it is a good indicator of the interests of the scientific community as well as their evolution over time. The blue columns chart corresponds to the single “thermoelectric” keyword (it was kept separately due to the significant scale difference), and it clearly shows that this research topic already has some decades, but it remains growing exponentially. Looking at the other keywords search set, the first appearance of determined concepts is easily perceptible, and the relation between them can be extrapolated. Over the last decades, the search for organic TE has grown exponentially (to be noted that the last column has the count for fewer years than the preceding columns), probably due to environmental awareness and the need for flexible and lightweight technologies. The union of “thermoelectric + printing” and “thermoelectric + flexible” keywords start appearing simultaneously, although with different growth rates, especially in recent years. This may be because most printed TEs are intended to be flexible, while flexible TE can be achieved through other thin film techniques. Most likely, the increase in flexible and printed electronics was driven by the advances in the organic semiconductors field. Regardless of the number of works linked to "thermoelectric + sensor" being high since the 80's, the wearable technology concept is more recent, emerging in the 2000’s. However, it is predictable that the interception of thermoelectrics and wearable applications will continue to draw the attention of researchers since the number of publications in the 2020-2022 period is already much higher than in all the period from 2010 to 2019. Although the research strands are interested in greener and sustainable production techniques, the coupling of life cycle assessment (LCA) and TE concepts has not been widely applied. Unfortunately, this seems a transversal problem to many research topics.

In summary, the field of thermoelectrics has undergone seven decades of development. Despite the primary objective remaining the enhancement of the ZT value, usually resorting to the optimization of non-sustainable thermoelectric materials through complex production methods to achieve high energy conversion, the reality is that the pursuit of more sustainable materials and techniques, even if less efficient, is gaining visibility.

2.2.2.2 Printing Methods

Printing methods are compatible with green materials, easily scalable to mass manufacturing processes, and low-cost. A variety of printing techniques have been explored for the production of electrical components and devices and the selection of the printing technique is dependent on the required printing resolution, fabrication throughput, homogeneity, minimum layer thickness, ink characteristics (e.g. viscosity, rheological behaviour, size and dispersion of the particles), and surface and mechanical properties of the substrate [129].

Printing deposition techniques are divided into contact processes - gravure, screen, flexography, and reverse offset printing - and non-contact processes - inkjet, electrospray, aerosol jet printing, and dispenser (3D) [130]. Among the several options available, SP is one of the most used printing methods due to the possibility of using it in a R2R process, and different types of sensors are produced using this technique [131]–[135]. In **Figure 2.9**, several examples of printed TE using different production techniques, TE materials, and substrates are shown.

Printable inks and pastes are typically composed of fillers, binders, and solvents, which can be combined in a suitable proportion to guarantee proper viscosity. The binders (typically acrylics, alkyds, cellulose, and resins) enhance the ink's adhesion to the substrate and the connection of the particles to each other after printing. Binding occurs during drying and solvent removal or sintering [136]. Other frequently employed ink additives include surfactants and dispersants, which facilitate the dispersion of nanoparticles within the surrounding vehicle, and defoaming agents that are used to reduce surface tension and prevent the entrapment of bubbles.

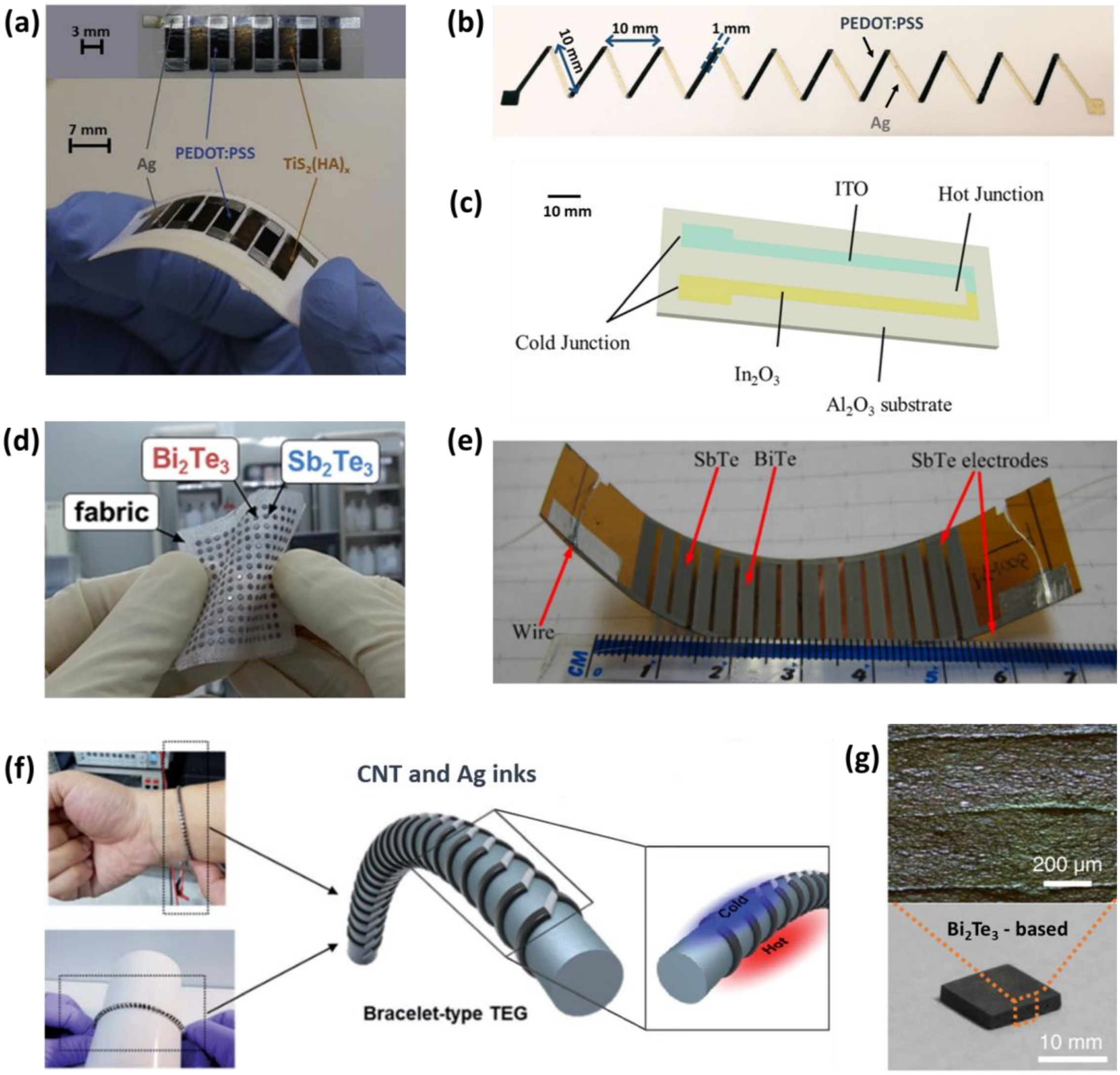

Figure 2.9 - Examples of published printed TE, highlighting the used materials in each description: **(a)** Inkjet printing on paper [137] - copyright 2019, Elsevier; **(b)** Blade-coating on paper [138]; **(c)** Screen-printing on alumina - reprinted from [135], with the permission of AIP Publishing; **(d)** Screen-printing on glass fabric [139] - copyright 2014, Royal Society of Chemistry; **(e)** Screen-printing on kapton [33] - copyright 2016, Elsevier; **(f)** 3D-printing on a PU cable [101] - copyright 2018, Royal Society of Chemistry, and **(g)** 3D-printing with no substrate [28] - reproduced with permission from Springer Nature.

The addition of biocides and fungicides sometimes hinders the growth of bacteria and fungi in conductive inks. Furthermore, the ink viscosity may be regulated by the addition of polymeric thickening agents (e.g. polyvinyl alcohol (PVA), EC, polyvinylpyrrolidone (PVP)) or solvents of different viscosity [136]. The EC is a widely available and recyclable cellulose derivative [140], [141], and it was used to adjust the viscosity of G_{Flakes} inks explored in **Chapter 4**.

The solvents play a core role in the rheological properties of the ink. In the case of SP, most inks select organic solvents such as toluene, tetrahydrofuran (THF), dimethyl sulfoxide (DMS), N-methyl pyrrolidone (NMP), dimethylformamide (DMF), propylene glycol, glycol, 2-propanol, and ethanol (EtOH), which are volatile, poisonous, and environmentally unfriendly. With the sustainable development and green initiatives, these organic solvents are not the best choice for ink preparation, and it is urgent to find “green solvents” that can not only achieve high solubility and stability of fillers but also meet the needs of health and environment [142].

2.2.2.3 Flexible Printing Substrates

Functional inks are formulated according to the desired features, and through printing techniques, it is possible to produce printed films on flexible substrates, achieving flexible devices. Polymeric substrates, such as PEN, PET, and polyimide (PI), known as kapton, are prevalent choices used in large area and flexible electronics. This preference stems from their mechanical and dimensional stability, temperature tolerance, smooth surface morphology (low roughness), barrier properties against oxygen and water, and good electrical insulation. However, while this type of substrate offers exciting properties, it is evident that devices designed for affordability and disposability demand recyclable and environmentally sustainable alternatives [36], [143].

Regarding eco-friendly flexible substrates, the paper has been in focus for printed, electronic applications due to its flexibility, lightness, abundance (renewable source), recyclability, and biodegradable nature, including in the fabrication of TE devices, [10], [117], [138], [144]–[147]. Besides these interesting properties, paper substrates can include printed electronic functions and existing paper products such as packaging. Examples of TE printed on paper can be found in **Figure 2.4** - **(b)** and **(c)** and in **Figure 2.9** - **(a)** and **(b)**.

Meanwhile, fabrics have also been explored, with research being allocated to substrates like polyester [22], [119], [148], glass fiber fabric [34], [41], [139], or cotton [149], [150] which has valuable properties for wearable and flexible applications, such as its breathability, foldability, and elastic recovery [151]. Examples of TE printed on fabric can be seen in **Figure 2.4** - **(c)** and **Figure 2.9** - **(d)**.

Among innovative eco-friendly materials to use with printing techniques, there is cork. In 2015, cork was studied as a possible substrate for inkjet, with a pre-coating treatment to its surface [152]. In 2019, the author of this thesis reported that cork was a suitable flexible substrate for screen-printing aiming ultraviolet light (UV) sensor production [141]. Similar photodetectors are reported in the literature but produced with highly complex and expensive techniques using vacuum systems and temperature steps, processes that are not compatible with flexible and lightweight substrates, and thus wearable technology [153]–[158]. In 2021, A. P. M. Tavares et al. reported cork as a substrate to produce 3-electrode electrochemical devices, also with screen-printing [159]. Besides its use as a printing substrate, it can also be used as part of composite materials for instance in matrixes of thermoplastic polyurethane (TPU), high-density polyethylene (HDPE) or polylactic acid (PLA), to use in 3D-printers [160]–[162].

2.3 Encapsulation - A Step Towards Real Life Applications

Every device produced on a laboratory scale has fixed conditions, such as controlled temperature or humidity. In contrast, they will face different and variable environmental conditions and mechanical stresses that might decrease the device's performance in real-life applications. Most of the studies do not specify these highly relevant conditions to check the devices' viability in some applications. The encapsulation aims to help the devices undergo extreme conditions and meet the different usage requirements with the minor performance loss possible. Lifetime, durability, variability, and stability are practical considerations that are seldom considered [163]. Some printed, electronic devices must have selective permeability, such as ozone sensors that should be able to adsorb oxygen [141] or humidity sensors that must interact with water molecules [131], [164]. On the other hand, optical sensors typically just require a transparent or optically neutral encapsulation [165], [166]. Finally, other sensors require an encapsulation to protect them against the environment's abrasion and wear.

Printing methods along with flexible substrates have been used to produce different kind of sensors, namely, for UV radiation [141], mechanical pressure [167], humidity [164], or temperature [98], [168]. Nonetheless, one of the most important requirements in bringing these devices to market is their encapsulation. Many of the materials used in printed and flexible electronics are sensitive to oxygen or moisture [169], leading to performance losses over time. Encapsulation is also a key aspect in improving the robustness of flexible devices against mechanical impacts or bending/twisting, increasing their durability and shelf-life [170].

For wearable applications, an encapsulation step should always be provided in the end of the device fabrication, not just due to irritating and toxic issues but also because of the materials' performance degradation over time. However, this will always cost in terms of thermal interface increased resistance.

2.3.1 Flexible and Eco-Friendly Encapsulants

Encapsulation technologies have evolved from traditional rigid cover plate encapsulation, rigid inorganic film encapsulation to the current flexible thin-film encapsulation [171], typically polymer-based materials - if the desirable devices to encapsulate are flexible, the encapsulant should keep their flexibility. The commonly used materials such as parylene [172], [173], PDMS [165], [174], laminated plastic [173], [175] and PVA [176], [177], among others, usually are toxic or difficult to recycle. Green encapsulation aims to reduce the environmental impact of flexible electronic devices by incorporating environmentally conscious materials and processes [178], limiting toxic or non-recyclable components and high energy-consuming techniques. Reasonably, suppose the materials and production processes had an eco-friendly approach. In that case, the encapsulation step must not be an exception - electronics have progressed beyond cost-effectiveness to embrace a more sustainable route.

Cellulose-based encapsulants can be a greener alternative to some of the presented options, allowing the biocompatibility and flexibility of the devices while adding a small cost to their production. In **Chapter 4**, it is show-cased a proof-of-concept of ethyl cellulose as a flexible and water impermeable encapsulant material.

Although PDMS is not a biodegradable material, it is an elastomer widely used in several research areas, such as microfluidics or stretchable electronics, suitable as substrate or composite matrix material. It is a biocompatible material, optically transparent, viscoelastic, chemically, and thermally stable, highly flexible, and hydrophobic. It requires low curing temperatures, can easily be moulded with high resolution and aspect ratio [124], [179], [180], and can have its viscosity manipulated [181]. There are several reports about PDMS composites where the PDMS properties were modified and optimized by adding other materials: composites with Ag micro sized flakes and carbon black [179], [182] for flexible electronics without the need of metallization, ZnO and CuO nano particles [183], [184] to form coatings with anticorrosion and antifouling properties, PZT micro particles [185] for piezoelectric devices, boron nitride [186] for wearable pressure sensing systems, graphite flakes [124], [180] for flexible temperature sensors, and graphene nanoplatelets [187] for photoresponsive actuation. In the TE field, PDMS has been reported as substrate and gap-filler, due to its low *k*, flexibility, and biocompatibility [24], [61], [71], [89], [139], [188].

In **Chapter 5**, the reader will find two different PDMS composites, with very distinguished properties: the PDMS/G_{Flakes}, a TE and electrical conductor composite used to produce TE sensors, and the PDMS/cork, an electrical insulator used to encapsulate devices. The choice of G was already explained, in **section 2.2.1**, as for cork, the following paragraphs will be dedicated to it.

As already mentioned in **section 2.2.2.3**, cork is considered a sustainable material, currently used for different industrial applications, of which stoppers for the wine industry and floating devices are two of the most representative [189]. The cork forests constitute a unique and diversified ecosystem, and cork-based products are considered “carbon neutral” since they decrease the amount of carbon dioxide in the atmosphere, being long-life, biologically based products. Cork is harvested without killing the tree, allowing future bark extractions, and used cork can be easily granulated and recycled into raw material for a second life [190], [191]. Macroscopically, cork is a lightweight material, with an average density of about 200 kg/m^3, practically impermeable to liquids and gases, innocuous, and almost age-insensitive, with remarkable chemical and biological stability and a good fire resistance. It is an elastic material, thermal and electrical insulator, and acoustic/vibration absorber. Microscopically, cork consists of layers of alveolar-like cells of which the membranes have a degree of waterproofing and are filled with an air-like gas, which occupies about 90% of their volume [192]. The number of published works focused on cork has increased over the years, which indicates a growing interest from the scientific community in this great raw material [190]. New cork applications for sports, filters, pharmacology, fashion, and architecture, among others, have been developed and commercialized. From haute couture shoes to designer clothes, cork is being used as a raw material to enrich these goods, attracting customers who seek high-quality products and goods from natural sources. The fabrics used to manufacture such commodities consist of extremely thin laminated sheets of natural or agglomerated cork bonded over cloth or another flexible support like paper [190]. In this work, it was produced a composite made of cork granules into a PDMS matrix aiming to lower the amount of PDMS needed, substituting part of it for an eco-friendlier choice and, at the same time, promoting a decrease of the volumetric mass density and thermal conductivity of the PDMS itself [193].

3

METHODS AND TECHNIQUES

Disclaimer

Some excerpts of this section have been published in the following publications:

Figueira, J.; Bonito, R. M.; Carvalho, J. T.; Vieira, E. M. F.; Gaspar, C.; Loureiro, J.; Correia, J. H.; Fortunato, E.; Martins, R.; Pereira, L. *Screen-printed, flexible, and eco-friendly thermoelectric touch sensors based on ethyl cellulose and graphite flakes inks*. Flexible and Printed Electronics **2023**, 8 (2). https://doi.org/10.1088/2058-8585/acc114.

Figueira, J.; Vieira, E. M. F.; Loureiro, J.; Correia, J. H.; Fortunato, E.; Martins, R.; Pereira, L. *Composites Based on PDMS and Graphite Flakes for Thermoelectric Sensing Applications*. Materials Proceedings **2022**, 8 (1), 42. https://doi.org/10.3390/materproc2022008042.

Figueira, J.; Loureiro, J.; Vieira, E. M. F.; Fortunato, E.; Martins, R.; Pereira, L. *Flexible, scalable, and efficient thermoelectric touch detector based on PDMS and graphite flakes.* Flexible and Printed Electronics **2021**, 6 (4). https://doi.org/10.1088/2058-8585/ac45de.

Different TE materials were explored throughout this PhD work, and various architectures/configurations were designed and produced. This section aims at exploring and explaining the production methods and characterization techniques used in this work. Concerning the materials used, a full description can be found at the beginning of each of the following chapters.

3.1 Production and Synthesis Methods

3.1.1 Screen-Printing

Screen-printing is a widely used printing method due to its simplicity, ease of prototyping and associated low-cost. It can have a fast printing speed (150 m/min), suitable for substrates with tailored textures, and versatility for pattern designs (resolution around 30-100 µm) [129]. It is a straightforward technique with the possibility of scaling it up in a R2R process, where all the components move synchronously.

In the SP technique, the ink is forced through the open areas of a specific mesh with the help of a squeegee (in this work, a rubber blade), as depicted in **Figure 3.1**, leaving a printed pattern on the substrate. This happens because the mesh, usually made of a woven fabric, typically polyester, has patterned holes blocked-up with a photo-polymerized emulsion correspondent to the negative of the intended printing pattern, where the ink could pass through the open mesh [194].

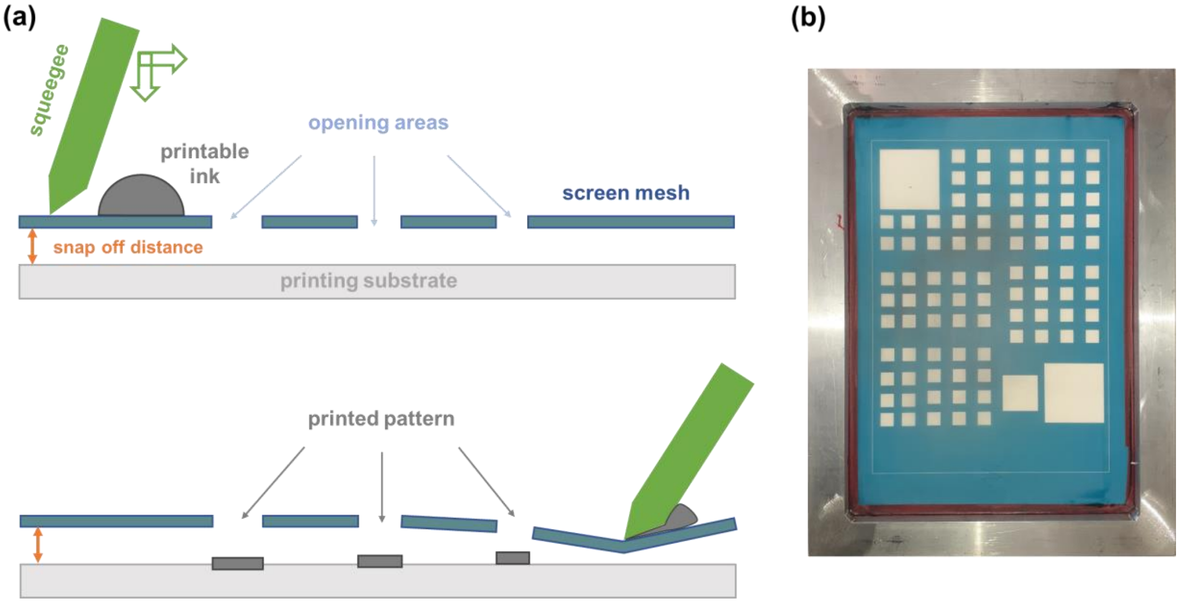

Figure 3.1 - **(a)** Screen-printing process scheme showing the initial phase when the ink is placed on top of the mesh and before the open pattern and also the final result of the squeegee passage with the printed pattern on the substrate and **(b)** example of a used screen-mesh.

Compared to flexography or inkjet printing, this technique requires higher viscosity inks (30-12000 cp), resulting in thicker films and low volatility solvents [130].

The most important parameters for screen printing are:

- the screen mesh (number of apertures per area).
- the squeegee speed, angle, and pressure.
- material viscoelasticity.
- desired shape (pattern, definition).
- snap-off distance (space between the substrate and the screen).

Other important parameters are the desired film thickness (single-layer/multi-layer), drying and curing processes (temperature, UV), and the type of substrate (flexible or rigid, hydrophobic or hydrophilic, smooth or rough). The squeegee movement can be promoted by a person (manual SP) or by a machine (semiautomatic SP). Although the first mode gives room to human errors and difficulty in repeatability of results between users, it is simpler and faster to begin a project printing manually. The use of the semiautomatic process pays off in cases where the inks and geometries are already optimized, and there is a need to print in a larger scale, once it takes time to optimize all the parameters and it spends more material.

The formulation of TE inks for screen-printing allows great freedom for different geometries and large area applications, without the need for complex cleanroom processes. Some limitations regarding this printing technique are the comparatively low printing resolution (~30 µm) [130] and the necessary cleaning steps.

3.1.2 Film Casting and Blade Coating

The film casting technique is widely used for the application of paints, varnishes, adhesives, liquid printing inks and many other surface coatings to produce quick, accurate and repeatable samples. It is based on an adjustable micrometer film applicator or meter bars moved by an automatic arm with controllable speed. The speed rate is directly connected to the viscosity of the ink applied onto the substrate and it plays a dual role in influencing both the thickness and the quality of the resulting film [195]. Striking the right balance between faster and slower blade speeds becomes essential to preserve the film's morphology and its crystallization process [196].

This work used a K101 Control Coater System (**Figure 3.2**), in which a mechanical arm can move at different speeds (from 2 to 15m/min) and fixed direction. The thickness of the wet films is controlled by the applicators and bars chosen, and final thicknesses can vary between 4 and 800 µm. The coating bed has an associated heating system that can be used during or after the casting, up to 150 °C. This technique was used to cast PDMS/G composite mixtures with a micrometer applicator to produce films (without T), and to encapsulate printed sensors with polymeric solutions using a rod (at 60 °C).

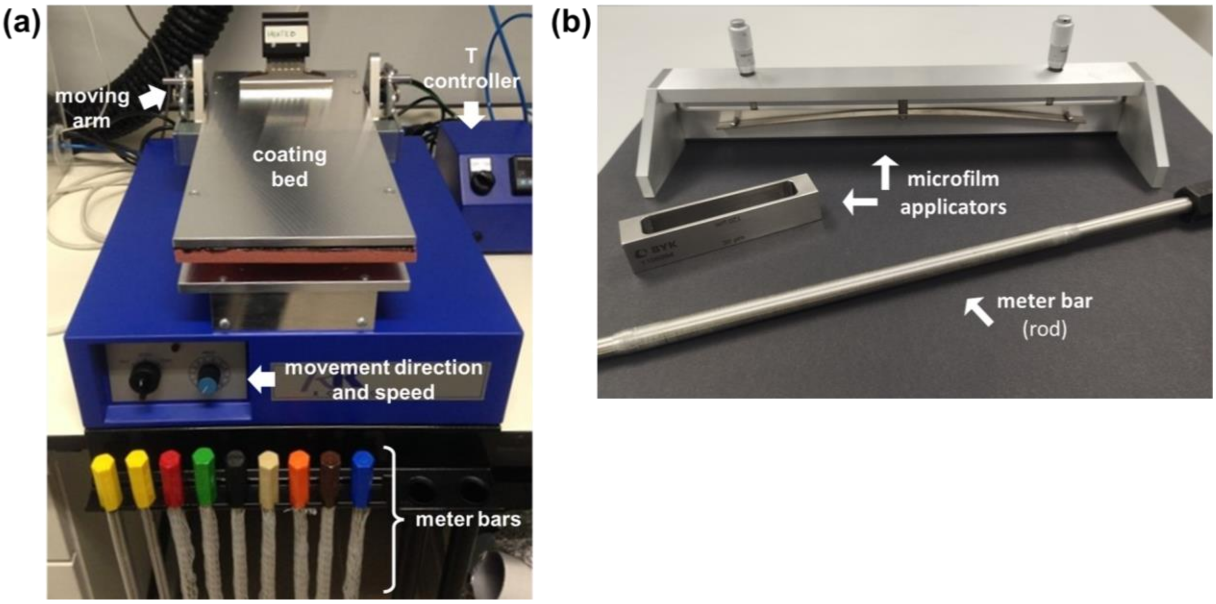

Figure 3.2 - **(a)** Control coater system used for film casting and **(b)** examples of tools to use with the moving arm to cast the solutions.

The principle of the doctor blade method is similar, where a solution/paste is deposited onto a substrate, resorting to a blade that moves on a single axis. This work used this method to cast the higher viscosity mixtures of PDMS/G, creating thick films up to 6.3 mm, using moulds with the desired final geometries.

3.1.3 Plastic Lamination

Laminating machines are used to add protective plastic coatings to chosen surfaces. In a thermal laminator, this is done by heating and fusing plastic pouches (in the case of two-sided laminating) over the surfaces to be covered. These laminating pouches are made of a combination of different types of plastic. The harder outer layer is usually based on PET, a polyester resin that can be formed into various shapes, for instance, flat sheets, which makes it ideal for laminating pouches. It provides the laminating pouches' stiff, rigid, and protective outer layer. The softer inner layer is usually ethylene-vinyl acetate (EVA), a resilient, soft, and stress-resistant plastic often used as a hot-melt adhesive [197]. Sometimes a combination of the PET, EVA, and polyethylene (PE) is used altogether [198].

The lamination step (**section 4.2.2.3**) was done using an OL 250-L-17 laminator along with transparent plastic pouches, from QUIGG, **Figure 3.3**. This laminator has two heated rollers inside, and a backloader technology for easy-of-use. It also has a short preheating time (< 1.5 min) and a fast lamination speed (400 mm/min).

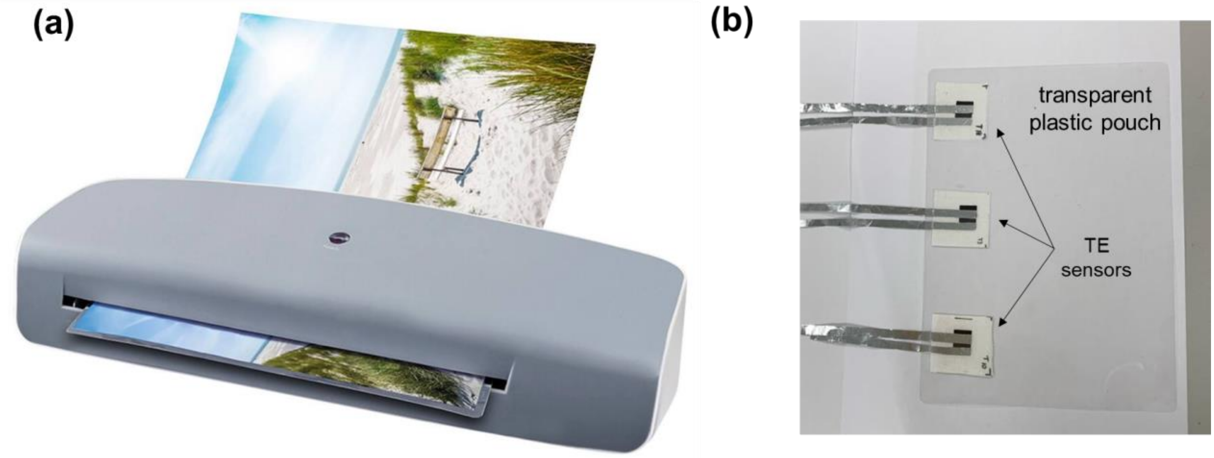

Figure 3.3 - **(a)** Example of the office laminator working with an A4 page and **(b)** image of an A5 plastic pouch being loaded with TE sensors inside for their encapsulation.

3.2 Characterization techniques

3.2.1 Open Circuit Voltage - Potentiostat

A potentiostat is a critical analytical instrument designed to precisely control the potential at the working electrode within an electrochemical cell. It contains a set of internal circuits that enable generating and measuring potentials and currents, making it a fundamental tool for conducting electrochemical investigations. Although electrochemical tests are often related to the study of chemical reactions involving electron transfer, such as redox reactions, corrosion studies, battery testing, or electroplating, the experiments conducted with this equipment may not typically be classified as traditional electrochemical tests. Measuring the open circuit voltage (V_{OC}) over time in TE samples exposed to a thermal stimulus promoting ΔT involves studying the electrical behaviour of materials, which can be related to the field of electrochemistry in a broader sense.

A specific electrode configuration was employed to characterize the sensors using the potentiostat. Two carbon ink (C_{ink}) electrodes were screen-printed on opposite sides of the quadrangular TE elements for the planar TE elements. Aluminium foils were added and affixed to the C_{ink} zones to extend the devices' electrical contacts. Similar connections were made on two opposite sides of the cubic elements in the case of vertical TE sensors. To assess the scalability of the process, connections were also established between multiple elements. The connection of the TE sample electrodes to the potentiostat terminals is crucial. To ensure that p-type materials exhibit a positive S and n-type materials exhibit a negative S, the hot side electrode was connected to the potentiostat positive terminal and the cold side electrode to the negative terminal. This polarity choice is vital for maintaining consistency in our data. A very small auxiliary current, bellow 10^{-4} A, was applied throughout the experiments while the V_{OC} was continuously recorded. This voltage serves as a representation of the potential or voltage relative to a predefined reference point and was monitored over time.

The TE sensor's response to touch events was acquired while touching (or not touching) the sample with a gloved (or ungloved) finger. The V_{OC} was continuously recorded at various water temperatures for the hot water test, allowing the TE material to return to its initial state between temperature changes. The data acquisition had a fixed time step of 0.1 seconds for each measurement.

During this work, a Gamry Instruments Reference 600^{TM} was used, a Potentiostat/Galvanostat/ZRA equipped with an acquisition and analysis software for physical electrochemistry and electrochemical impedance experiments, **Figure 3.4** - **(a)**. An example of a TE sample ready for the potentiostat connections can be found in **Figure 3.4** - **(b)**.

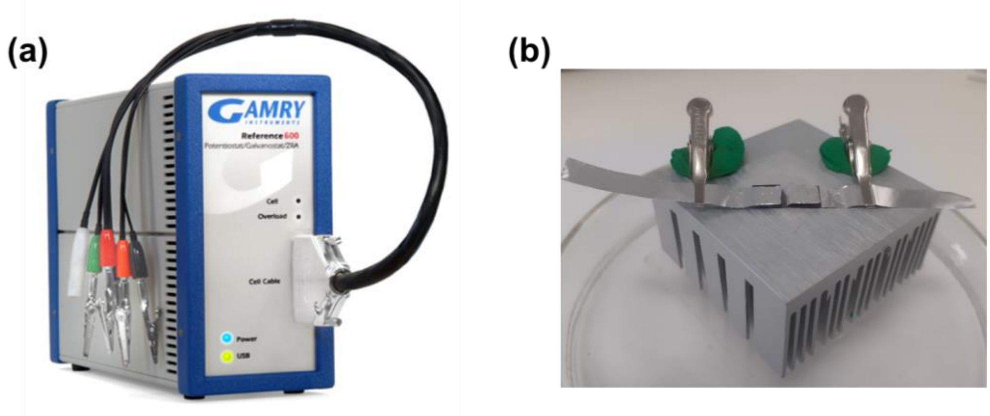

Figure 3.4 - **(a)** Potentiostat equipment (which is used along with a computer and a Faraday cage) and **(b)** a TE sensor with two vertical elements ready to be characterized.

3.2.2 Hall Effect

The Hall effect is one of the most important galvanomagnetic effects, which are physical effects arising in matter carrying electric current in the presence of a magnetic field. When a semiconductor material is subjected to a perpendicular magnetic field ($\vec{B}$) while current (I) flows through it, the free carriers are deflected to one side of the sample, creating an electric field.

The Hall effect generates a voltage drop orthogonal to the path of moving electrons and the applied magnetic field [199], which can be used to determine information about charge carriers in the material, such as their sign (positive for holes and negative for electrons), concentration (n) and mobility (μ). The Hall effect is commonly used as a technique to measure electrical resistivity (sheet and bulk).

The following **Equation 3.1**, **3.2**, **3.3** and **3.4** translate the relations beyond these parameters [143]:

$$V_H = \frac{\overrightarrow{|B|}\,.I}{q\,.n\,.d_s} \quad (\mathrm{V}) \tag{3.1}$$

$$R_H = \frac{V_H \, .d_s}{|\vec{B}| \, .I} \quad (\text{cm}^3/\text{C}) \tag{3.2}$$

$$n = \frac{1}{q \, .R_H \, .d_s} \quad (/\text{cm}^3) \tag{3.3}$$

$$\mu = \frac{R_H}{\rho} \quad (\text{cm}^2/(\text{V.s})) \tag{3.4}$$

Where V_H is the Hall voltage, q is the electron charge, d_s is the thickness of the sample and R_H is the Hall coefficient. The sign of R_H indicates whether the semiconductor is n-type or p-type, if the sign is negative or positive, respectively.

During this work, the carrier Hall mobility, electrical resistivity, sheet resistance, and carrier concentration were measured with a Biorad/Nanometrics HL5500 Hall effect system **Figure 3.5** - **(a)**, using van der Pauw contact geometry, **Figure 3.5** - **(b)**. Although this system can analyse from -180 to 225 °C, all the measurements were performed at RT. The samples for Hall measurement were cut in quadrangular shapes (10 x 10 mm^2) and covered with C_{ink} contacts at the four corners.

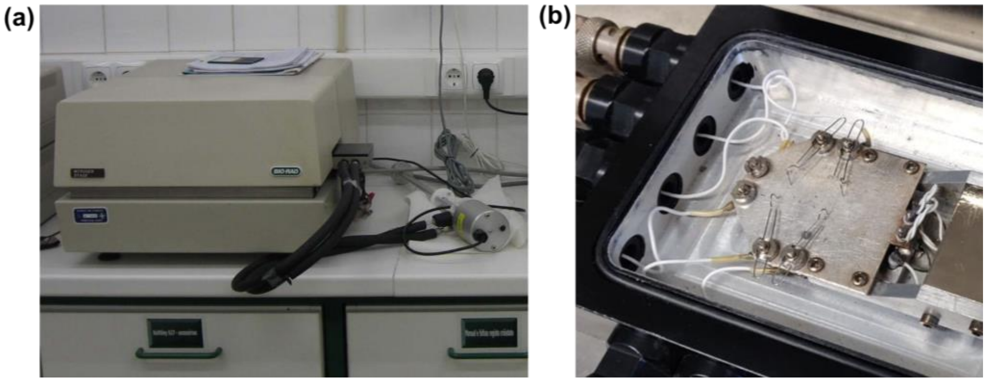

Figure 3.5 - **(a)** Hall effect system installed at Cenimat facilities and **(b)** zoomed-in image of the assembly zone for the sample characterization.

3.2.3 Seebeck Coefficient

To measure the Seebeck coefficient the TE sample is submitted to a thermal gradient, i.e., assemble the material between two plates at different temperatures, where at least one side can have a variable temperature so different temperature gradients can be tested. The S of planar samples was measured at RT, using a homemade setup based on the 'two-probe' method [105], **Figure 3.6**, in University of Minho facilities.

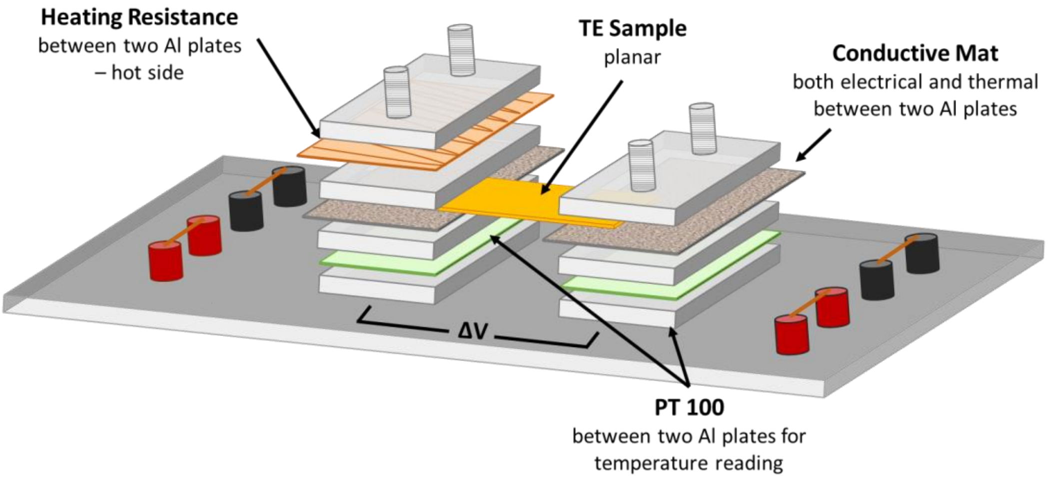

Figure 3.6 - Characterization setup for planar thermoelectric films Seebeck coefficient measurement.

This method consists in connecting one side of the film to a heated metal block at a fixed T (the block is heated by the application of successive voltage values, between 1 and 3 V) using the DC programmable source (Yokogawa model 7651) and the other side to a heat sink at RT, to generate ΔT along the film. This ΔT was measured using platinum wire resistors, Pt-100 (100 Ω at 0 °C precision resistor) at both metal blocks. The resulting thermovoltage (ΔV) was measured by an Agilent 34 410 A 61/2 Digit Multimeter. A linear plot of ΔV versus ΔT is expected, representative of a good thermal contact between the film and the blocks. The S values and corresponding errors were obtained using the LINEST function in an EXCEL worksheet. This function uses the least squares method to calculate the statistics for a straight line (that best fits the experimental data) and returns an array of parameters describing that line, including S (from the slope of the linear fitting), and the associated error [168].

3.2.4 Viscosity

Rheology is the study of the flow and deformation of matter. Usually, these studies are performed with liquids but can also be applied to certain solids. One of the rheological properties is viscosity, which can be simply defined as the internal friction acting within a fluid, i.e., its resistance to flow [200]. A viscosimeter is an instrument that measures the fluid flow and the viscosity of liquids, assessing how resistant a material is to motion when a force is applied.

The formula for measuring the absolute viscosity (η) is described in **Equation 3.5** [201]:

$$\eta = \frac{\tau}{\dot{\gamma}} \quad (\mathrm{cP}) \tag{3.5}$$

Where τ is the shear stress of the fluid, the force per unit area that you need to move one layer of fluid in relation to another [202], and $\dot{\gamma}$ is the shear rate, in which the dot denotes the first derivative of strain versus time - the velocity of the deformation of its form.

Broadly, there are two types of fluids: the Newtonian and the non-Newtonian. In Newtonian fluids, the viscosity remains constant, regardless of changes to the shear rate. In a non-Newtonian fluid, the viscosity values fluctuate [202].

The η of a particle suspension, such as a printable ink, is largely a function of particle volume fraction, particle shape, interactions between particles, particle size distribution, suspension structure, surface properties, adsorbed species, and the hydrophilic/hydrophobic nature of the particles/polymer [111].

In the example of an ink to use in screen-printing, the quality of screen-printed patterns depends on the ink rheology, printer hardware (screen, squeegee, substrate) and the printing process parameters [110]. The ink flow through the stencil is significant as it determines the uniformity of the printed surface. The more viscous and elastic the ink, the less easily it flows through the screen and spreads to make an even film, but if the viscosity of the ink is too low, it will not recover and gives ‘‘slurred’’ prints [110].

In **Chapter 4**, the viscosity of the screen-printed G_{Flakes} inks was measured using a viscometer CAP 2000+ (Brookfield Engineering), **Figure 3.7** - **(a)**, with a spindle 09 (viscosity range: 20 – 10800 cP), at a set T of 25 °C, at 5-10 rotations per minute (rpm). A solvent trap was used to avoid evaporation during the measurement. Also, the viscosity of the EC ink used for encapsulation was measured using an Anton Paar MCR 502 Rotational Rheometer, **Figure 3.7** - **(b)**, at set T of 25 and 60 °C, for shear rates varying between 1 and 1000 s^{-1}.

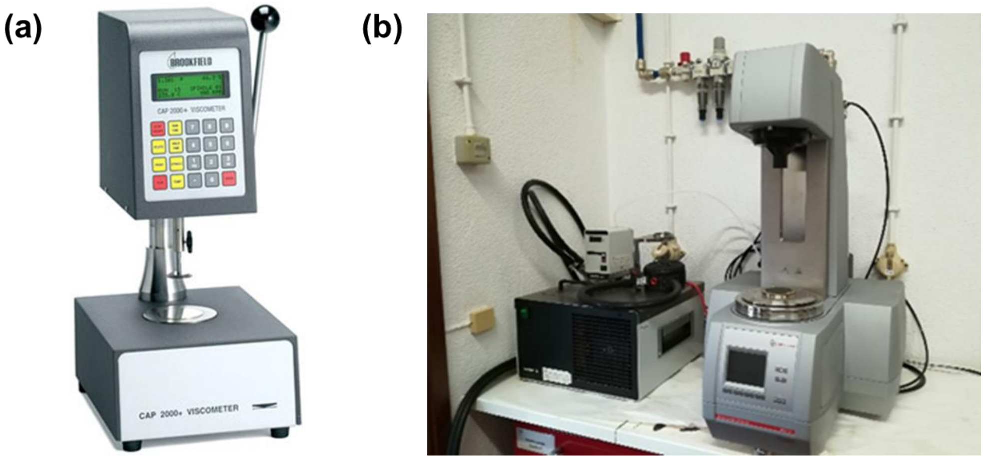

Figure 3.7 - **(a)** The viscosimeter CAP 2000+ at Cenimat facilities and **(b)** the MCR 502 rotational rheometer at the department of materials science.

3.2.5 Scanning Electron Microscopy

A scanning electron microscope (SEM) allows an analysis of materials at the nanometric scale, covering different applications such as topographical surface, chemical composition, or crystalline structure analyses.

This characterization method relies on the following main components [203]:

- a source to generate a highly energetic electron beam, which is called electron gun.
- a travelling vertical column where the electrons pass through at least two electromagnetic lenses.
- a deflection system based on scan coils.
- electron detectors for backscattered and secondary electrons.
- a chamber for the sample.
- vacuum pumps to decrease the pressure of all system.
- a computer screen to display the scanned images and a keyboard to control the electron beam parameters.

The interaction of the beam with the surface can result in the absorption by the sample, the reflection of primary electrons (backscattering), the emission of secondary electrons and the emission of electromagnetic radiation [143].

The primary electrons of an energy between a few keV and 50 keV interact with the sample up to a depth of 1 µm from the surface. Secondary electrons (SE) have an energy factor of a thousand lower than the primary electrons, so they are emitted only from a region of a few angstroms from the sample surface. These electrons provide a topographical contrast since the SE yield depends on the slope and curvature of the surface. The resolution of an SE image is in the order of 2 nm. Backscattered electrons (BSE) have a kinetic energy like the primary electrons and are obtained up to a depth of a few tenths of a micrometer. Since the interaction volume increases with the depth from the surface, a lower lateral resolution is obtained from BSE [204].

The probability for backscattering depends on the atomic number of the incidence zone, so elemental contrast can be obtained, if the atomic numbers are sufficiently different among the sample. When detecting electrons which are emitted from the sample under different angles between the primary beam and the surface, BSE which have undergone Bragg diffraction by the crystal lattice of the samples can be detected. This technique is called electron backscatter diffraction and can be used to study the crystallography and microstructure of the material. In addition to SE and BSE, Auger electrons and X-ray fluorescence are produced in the samples as competing processes. Due to the relatively low kinetic energy, Auger electrons are emitted only from the top few nanometers of the surface. Fluorescent X-rays are emitted from a depth of up to 1 µm. Both provide elemental information, but most commonly, the fluorescent X-rays are detected by energy dispersive spectroscopy (EDS) [204].

Throughout this work, SEM was used for topographical surface analysis, to study the printing substrate type or to access the quality of the printed layers, and it was also used to evaluate the microstructure of the produced composites when varying their composition. The images acquisition was performed using a Hitachi TM 3030Plus tabletop workstation (Tokyo, Japan), **Figure 3.8 - (a)**, and for non-conductive samples, a thin metallic coating of 20 nm of iridium was deposited before the SEM analysis (example in **Figure 3.8** - **(b)**).

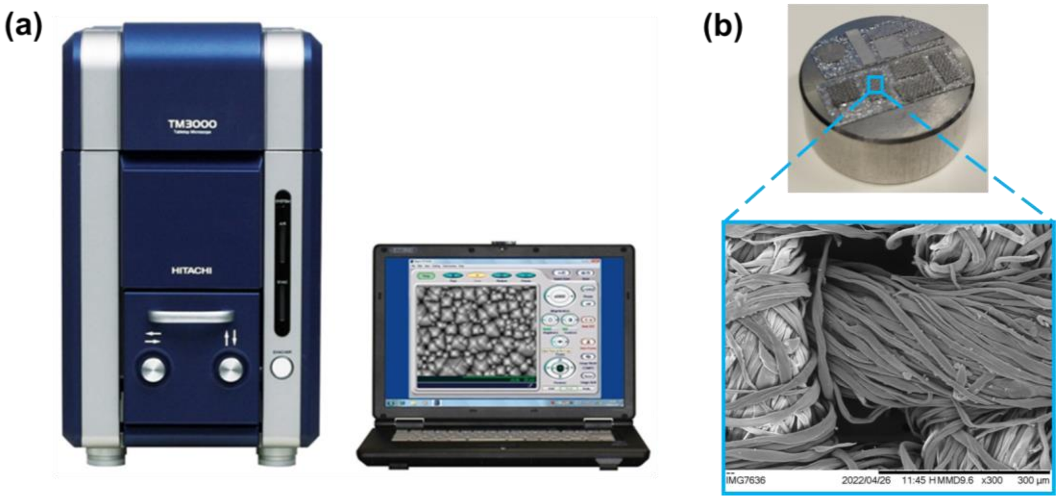

Figure 3.8 - **(a)** The TM3030Plus equipment at Cenimat facilities and **(b)** image of metallised samples assembled for observation and an example of a correspondent SEM image.

3.2.6 Contact Angle

The contact angle (CA) measurement is a surface analytical method that is used to measure and discern the ability of a specific material to absorb or repel a specific liquid. A representation is depicted in **Figure 3.9**, considering a liquid drop resting on a flat and horizontal solid non-porous surface.

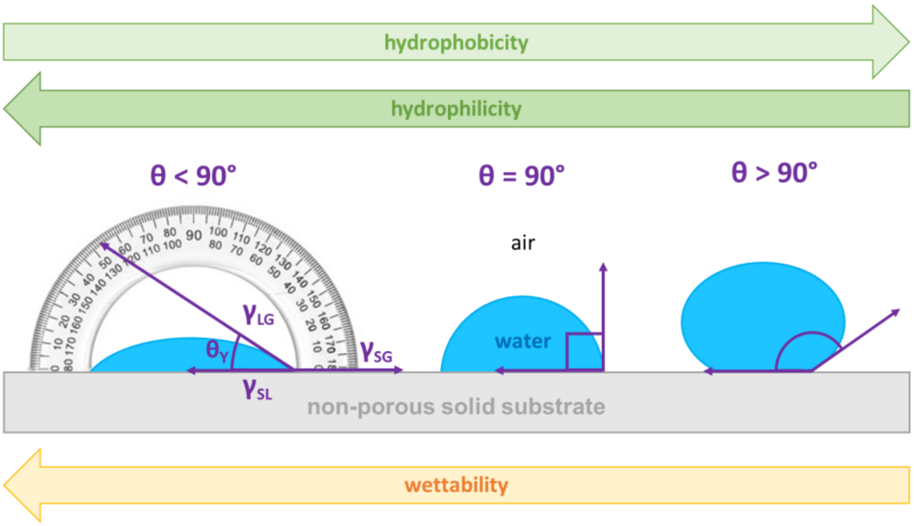

Figure 3.9 - Illustration of CA formed by sessile liquid drops on a smooth homogeneous solid substrate, in a gaseous medium, with indications about the respective interfaces and surface properties.

The measured contact angle is the angle between the solid-liquid interface on their surface. In this case, the liquid is water, and the experiment gaseous medium is air. A small contact angle is observed when the liquid spreads on the surface, while a large contact angle is observed when the liquid beads on the surface, i.e., the larger the contact angle, the greater the hydrophobicity and vice-versa. When this static CA surpasses 150° it is applied the term superhydrophobicity. A CA less than 90° indicates that wetting of the surface is favourable, and the fluid will spread over a large area on the surface easily, while CA greater than 90° generally means that wetting of the surface is unfavourable so the fluid will minimize its contact with the surface and form a compact liquid droplet [205].

The CA of a liquid drop on an ideal solid surface is defined by the mechanical equilibrium of the liquid under the action of three interfacial tensions:

$$\gamma_{LG}.\cos(\theta_Y) = \gamma_{SG} - \gamma_{SL} \qquad 3.6$$

where γ_{LG}, γ_{SG}, and γ_{SL} represent the liquid-vapor, solid-vapor, and solid-liquid interfacial tensions, respectively, and θ_Y is the contact angle. **Equation 3.6** is usually referred to as Young's equation, and the interface where solid, liquid and gas co-exist is referred to as the "three-phase contact line" [205].

This work used CA measurement by drop shape analysis to determine hydrophilicity of printing substrates and their encapsulants. The static water CA measurements were performed with DataPhysics OCA 15 Plus (Filderstadt, Germany), using 2 µL deionized water droplets. The side view of the droplet was acquired with a camera operating in a monochromatic regime, and the CA was determined using the Laplace-Young approximation model.

3.2.7 Simultaneous Thermal Analysis

A simultaneous thermal analyser (STA) can perform a thermogravimetric analysis (TGA) and a differential scanning calorimetric (DSC) measurement of a sample in the same instrument at the same time. This way, it is possible to ensure identical conditions for both characterizations.

In TGA the mass variation is monitored as a function of the temperature. In DSC, the difference between the heat flow rate to the sample and a reference material is measured. With this technique, it is possible to determine the changes in the enthalpy of the samples, specific heat, and the temperatures at which these occur [143].

This thermal characterization was performed for the encapsulant materials used in **Chapter 4**, ethyl cellulose, polyvinyl alcohol, and laminated plastic, giving particular attention to thermogravimetry analysis. The measurements were conducted in a simultaneous thermal analyser from Netzsch (TGA-DSC-STA STA 449 F3 Jupiter), **Figure 3.10** under air atmosphere, between 20 and 500 °C, with a 10 °C/min heating rate, in an aluminium crucible.

Figure 3.10 - The STA 449 F3 Jupiter equipment at Cenimat facilities.

4

SCREEN-PRINTED GRAPHITE INKS ON FLEXIBLE SUBSTRATES FOR TOUCH DETECTION

Disclaimer

Some excerpts of this section have been published in the following publication:

Figueira, J.; Bonito, R. M.; Carvalho, J. T.; Vieira, E. M. F.; Gaspar, C.; Loureiro, J.; Correia, J. H.; Fortunato, E.; Martins, R.; Pereira, L. *Screen-printed, flexible, and eco-friendly thermoelectric touch sensors based on ethyl cellulose and graphite flakes inks*. Flexible and Printed Electronics **2023**, 8 (2). https://doi.org/10.1088/2058-8585/acc114.

4.1 Introduction

This section is dedicated to the results of optimizing ethyl cellulose and graphite flakes (G_{Flakes}) inks to be used as a functional material for flexible thermal touch sensors produced by screen-printing. Graphite concentrations of 10, 20 and 30 wt% in an EC ink's base were tested with 1, 2 and 3 screen-printed layers. The TE inks were printed on four different substrates: (i) cotton (Cot), (ii) organic cotton (OrgCot), (iii) office paper (OP) and (iv) sticker label paper (SL). It was assumed that each substrate has a characteristic *k* that would interfere with the sensors' response time and other distinctive properties that would vary the ink's adhesion and printed layers' quality, consequently leading to different sensor responses. For instance, and as can be seen in **Figure 4.1**, the two chosen fabrics show a difference in the mesh apertures, and the two papers show differences in the fibre's diameters and binder compounds. Likewise, depending on the wt% of G_{Flakes} and the number of printed layers, the printability of the inks and the films' electrical and TE properties differ.

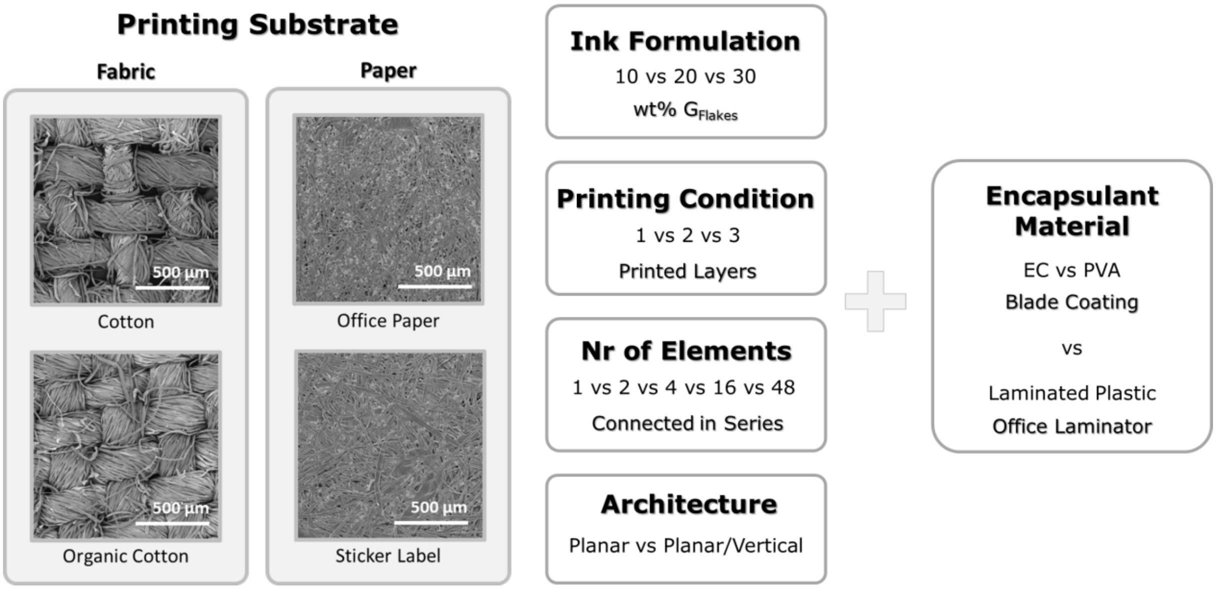

Figure 4.1 - Scheme of the studied variables in this chapter about ethyl cellulose and graphite screen-printing inks.

Besides the chosen materials and printing conditions, the architecture adopted to fabricate the touch sensors is also very important in terms of the number of connected elements, heat collection, and thermal stabilization towards incrementing the maximum ON state voltage (V_{ON}).

The conjugation of these variables (**Figure 4.1**) was assessed regarding printability, sheet resistance, and thermoelectric response. The first main goal was to optimize the SNR of the sensor when stimulated with just one finger touch, promoting a ΔT along the sample.

In this work, a study was conducted to evaluate different materials for encapsulating these flexible and printed TE touch sensors on paper and cotton substrates: EC and PVA, using blade-coating, and laminated plastic with a commercial office laminator machine. Thus, the second main goal was to reach an adequate encapsulant material, which maintained the flexibility of the devices while adding a relevant degree of water impermeability.

4.2 Experimental Details

4.2.1 Materials

4.2.1.1 Printed TE Sensors

Ethyl cellulose (Sigma-Aldrich, extent of labelling: 48% ethoxyl) and diacetone alcohol (DAA, 4-Hydroxy-4methyl-2-pentanone 99% from Aldrich) were used to create the screen-printing ink base. Graphite flakes (mesh 325, 99.8 %, metal basis from Alfa Aesar®) were added as received. Commercial carbon screen paste (CRSN2644, from SunChemical®, see **Appendix Figure 1**) and commercial aluminium foil were used to create the electrodes and conductive paths between the TE elements.

Four different substrates were tested: multi-function paper (office paper) with an 80 g.m^{-2} grammage from Inapa Tecno; commercial thermal labels from Staples (referred to as sticker labels); organic cotton poplin fabric (referred to as organic cotton) by Bo Weevil with a weight of 125-130 g.m^{-2} and a 168-thread count, and natural cotton fabric (referred to as cotton) from Fiacri.

4.2.1.2 Encapsulation Studies

Sensors with 2 printed layers of ink with 20 wt% of G_{Flakes} were produced using substrates of multi-function paper (office paper) with an 80 g.m^{-2} grammage from The Navigator Company and natural cotton fabric from Fiacri.

Two encapsulant materials were deposited using blade-coating (see **section 3.1.2**): 7.5 wt% EC dissolved in a mixture of 80:20 (V/V) of EtOH and DAA (EtOH, CAS: 64-17-5, from Carlo Erba Reagents), and PVA (CAS: 9002-89-5, from EVO-STIK) mixed with milli-Q water (1:7 or 3:2 V/V). A commercial plastic pouch (thickness range of 80-125 µm, from QUIGG) was also tested as an encapsulant material.

4.2.2 Samples and Devices Preparation

4.2.2.1 Inks formulation and screen-printing

A screen-printing TE ink was produced, dissolving 5 wt% of EC in DAA, with a stirring step of 300 rpm at 140 °C, to form the ink base, and then adding three different concentrations of G_{Flakes}, 10, 20 and 30 wt%. The EC supplier refers to the use of a mixture of toluene and ethanol (80:20 v/v) to dissolve the EC to achieve a specific viscosity of 300 cP. However, these solvents are very volatile (boiling points 111 °C and 78 °C, respectively). This implies a high evaporation rate, promoting the fast drying of the solution and possible clogging of the mesh while printing. Another disadvantage of this solvent mix is that toluene might be problematic [206]. During the internship at Swansea University, it was learned that DAA could dissolve the EC as well, being considered a green solvent and with a higher boiling point (166 °C) [111], [206]–[208], making it the chosen solvent for the TE inks. **Figure 4.2** - **(a)** describes the procedure followed to obtain these screen-printable inks.

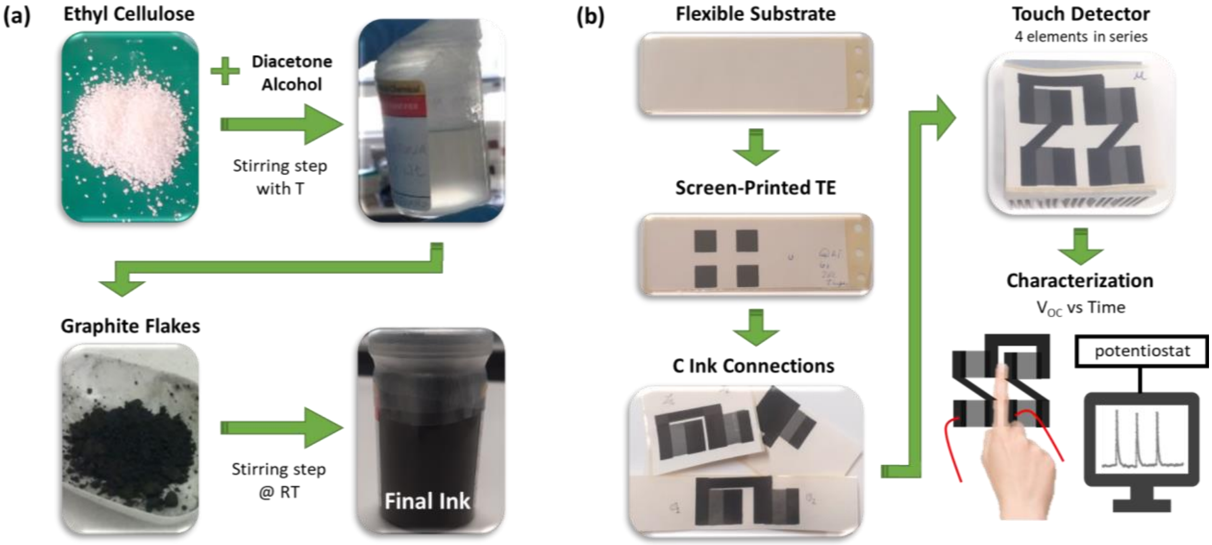

Figure 4.2 - Scheme of the: **(a)** ink production steps and **(b)** printing steps to obtain the thermoelectric planar sensors, exemplifying the characterization method of touch detectors using a potentiostat.

The formulated TE inks were screen-printed using a mesh model 77-55 (mesh count 190, aperture 81 µm, thread diameter 55 µm), varying the number of printed layers and the type of substrate. The printed TE elements were left to dry at RT. Carbon paths between them were then printed with a mesh model 120-34 (mesh count 305, aperture 45 µm, and thread diameter 34 µm) and cured for 30 min at 100 °C using a hot plate. Schematic representations of the fabrication steps for the fully screen-printed TE touch sensors and characterization can be seen in **Figure 4.2** - **(b)**, using the example of printing a 4-elements device on sticker label paper as the substrate.

4.2.2.2 Geometries

Figure 4.3 shows an illustration of the printing patterns used to obtain the TE sensors. Firstly, the TE ink was printed **(i),** followed by the C_{ink} printing for electrical connections **(ii).** In **(iii)** there is the final printing result, conjugating both patterns in the referred order.

For the 16 TE elements arrays, after the screen-printing, there was an additional production step of coiling the printed films around a hollow core made with a piece of cardboard straw with a diameter of 7 mm **(iv)**; this way, passing from a planar architecture to a planar/vertical one.

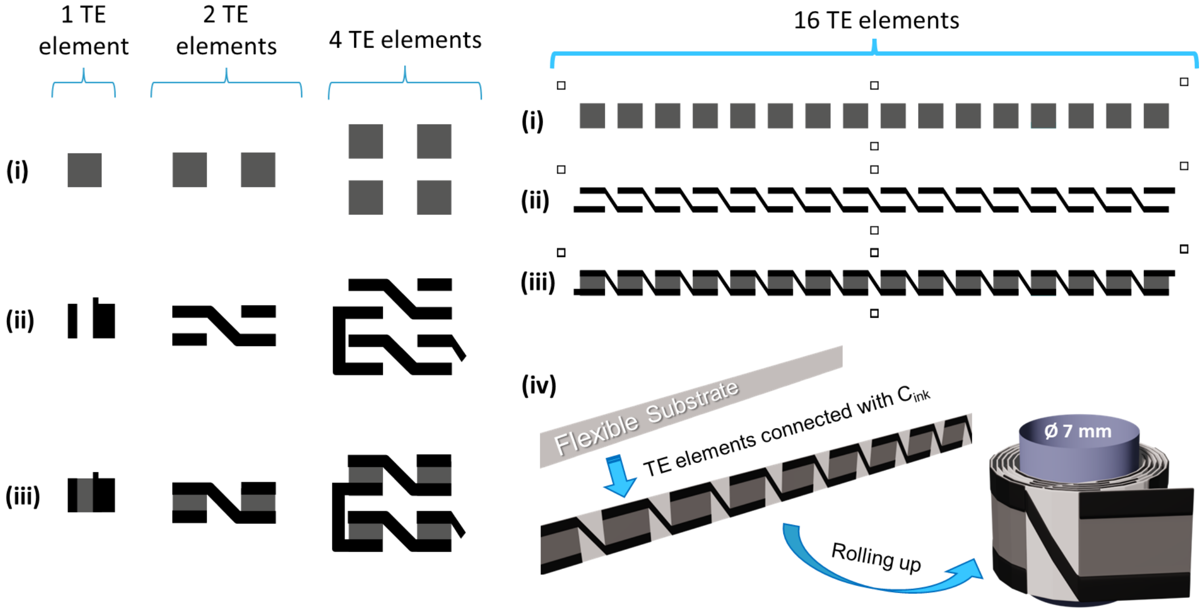

Figure 4.3 - Illustration of the printing patterns used to obtain TE sensors with 1, 2, 4 or 16 elements: **(i)** printing patterns for the TE elements, **(ii)** printing patterns for the C_{ink} connections and **(iii)** the final conjugation of both patterns. The step **(iv)**, regarding the 16-elements arrays, illustrates the rolling process to obtain planar-vertical architectures.

4.2.2.3 Encapsulation Step

The blade coater was used with a 4 µm or a 90 µm wet thickness rod or film applicator. The depositions were made with a bed temperature of 60 °C, at a speed level of 2 and 4 for EC and PVA mixtures, respectively.

Regarding EC encapsulation, after depositing one side and allowing it to dry for five minutes at 60 °C, the back was coated similarly. The PVA samples' back was coated after the first side had dried for 24 hours at RT. According to the manufacturer, the commercial plastic pouches were laminated with a 400 mm/min operating speed, operating at a temperature of roughly 135 °C.

4.2.3 Characterization and Testing

4.2.3.1 Substrates, Inks, and Samples Characterization

A SEM analysis (**section 3.2.5**) was used to assess the printing quality of printed layers, substrate coverage, and pristine substrates. Since the substrates are insulators, an Iridium layer was deposited for better image acquisition.

A screen-printable ink should have relatively high viscosities, typically between 1000 to 25 000 cP, when compared with other printing techniques like inkjet or flexography [209], [210]. The measured viscosity values at 25 °C (see **section 3.2.4**) were 1945 cP ± 9 %, 3150 cP ± 14 % and 10795 ± 25 %, for 10 wt%, 20 wt% and 30 wt% G_{Flakes} ink, respectively, meaning they are suitable for SP.

The Seebeck coefficients of the printed G/EC films were measured at RT in a planar configuration (as explained in **section 3.2.3**).

The sheet resistance (R_{Sheet}) was measured (**section 3.2.2**) using samples cut in quadrangular shapes and covered with Ag ink at the corners. The measurements were conducted at RT (temperature kept between 22.5 °C and 23.1 °C) at relative humidity (RH) of 38 % and 46 % for the organic cotton and cotton substrates, respectively. Regarding the paper substrates, the RT was kept between 22.7 °C and 23.1 °C, while the RH was 40 % and 44 % for office paper and the sticker label substrates, respectively.

4.2.3.2 Encapsulant Materials

EC ink viscosity was measured at 25 and 60 °C (**section 3.2.4**). A DSC analysis was conducted in air from 25 to 500 °C (heating ramp 10 °C/min) to analyse the thermal properties of the chosen encapsulant materials. For surface imaging, SEM was used to see the differences between the substrates as purchased, after encapsulation and after the bending tests. Static water CA measurements were performed using 2 µL droplets of deionized water (more details in **section 3.2.6**).

4.2.3.3 Devices Characterization

Before Encapsulation:

The non-encapsulated TE sensor's response to touch events was characterized by measuring the V_{OC} over time in a potentiostat (**section 3.2.1**) while touching (or not) the sample with a gloved finger. To perform this characterization, two electrodes of C_{ink} were screen-printed on opposite sides of the quadrangular TE planar elements and aluminium foils were added (glueing them to the Cink zones) to extend the device's electrical contacts. To test the scalability of the process, the C_{ink} was also used to connect TE elements in series. Mechanical stress tests were performed by bending the sensors with controlled curvature radii (7, 15 and 25 mm) and measuring their response over time (up to 800 h).

After Encapsulation:

The encapsulated TE sensor's response to touch events was characterized by measuring the V_{OC} over time in the potentiostat in the same way as for the non-encapsulated samples. Bending tests were conducted using a 15 mm curvature radius (CR), and water submersion tests were performed for 1 minute, with the sensors being remeasured afterward.

4.3 Results and Discussion

4.3.1 Electrical and Morphological Characterization

4.3.1.1 Cotton and Organic Cotton Substrates

Figure 4.4 presents the average of the measured R_{Sheet} values for both fabric substrates, considering different combinations of variables (10 to 30 wt% G_{Flakes} and 1 to 3 printed layers). As expected, the measurements show that increasing G_{Flakes} wt% in the ink results in a higher electrical conductivity for the printed elements. In addition, regardless of the substrate, it is possible to conclude that the R_{Sheet} values of the samples are also reduced with the number of printed layers. This happens due to a better substrate coverage, increasing the percolation between the conductive flaked particles.

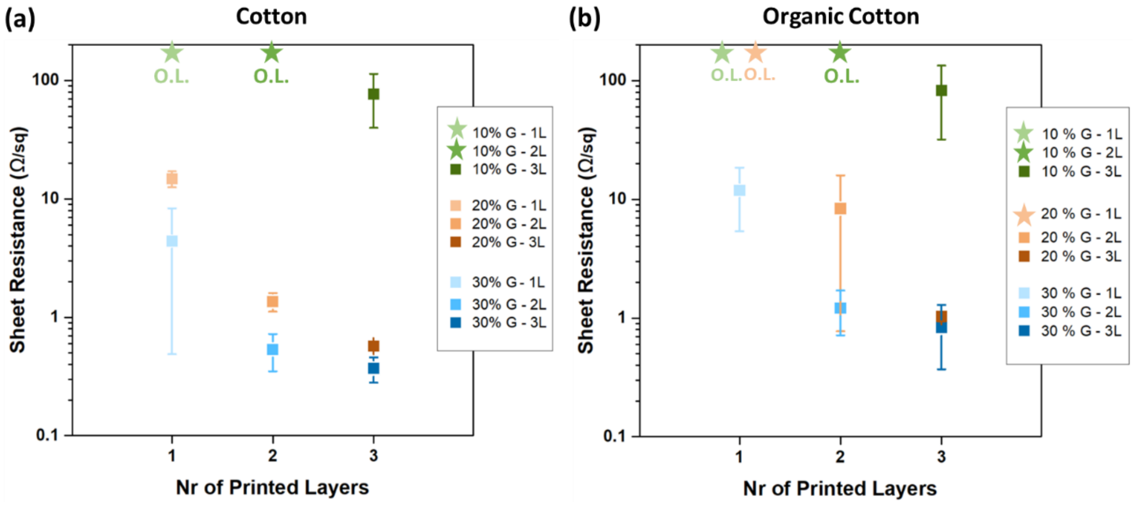

Figure 4.4 - Average R_{Sheet} values for different number of printed layers (1, 2or 3 layers) and graphite wt% composition (10, 20 and 30 wt%) on: **(a)** cotton, and **(b)** organic cotton substrates. The star symbols represent samples that were too electrically resistive (overload (OL) situations) to perform the R_{Sheet} measurements.

Comparing the two fabric substrates, the films printed on OrgCot have consistently higher R_{Sheet} values and associated errors, independently of the studied conditions, which means that Cot allows better and more repeatable results. The SEM images (**Figure 4.5**) help to understand how the fabric woven structure affects the printability and coverage of both fabric substrates. The first image of each set of **Figure 4.5** - **(a)** and **(b)** presents the substrates before coating, while the ensuing images are for different printing conditions and ink formulations (the extreme conditions - 1 layer of 10 wt% vs 3 layers of 30 wt% - and three images in between - 2 layers of 10, 20 and 30 wt%).

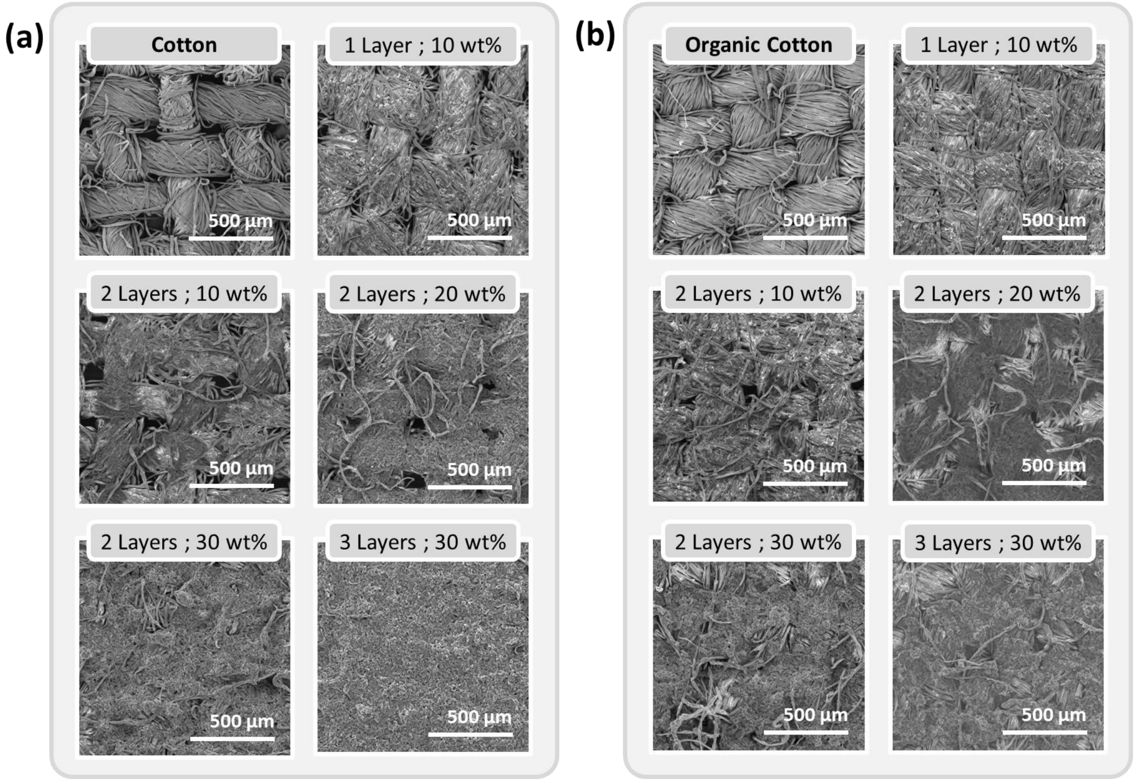

Figure 4.5 - Surface SEM images of screen-printed TE films with different printing conditions (number of printed layers and wt% of G_{Flakes}) on: **(a)** cotton, and **(b)** organic cotton substrates. For comparison purposes, the first image of each set presents both fabric substrates without TE material (pre-printing).

For the condition of 3 printed layers of the 30 wt% G_{Flakes} ink, it is observed a uniform coverage of the surface on the Cot substrate, barely leaving any thread or hole exposed, while in the OrgCot substrate, the fabric threads are easily identified and spotted. This can be due to different factors such as fibre staple length, weaving method, number of twisted fibres, degree of twisting or fibre treatment, leading to a lower printing quality [211], [212]. Although OrgCot initially appears to have a more closed mesh and a smoother surface, the Cot substrate promotes better ink adhesion and G_{Flakes} assembling, increasing the layer uniformity and a more efficient formation of electrical paths, which matches their R_{Sheet} values, that have the lowest value for 3 layers of 30 wt% of 270 ± 24 Ω/sq and 831 ± 55 Ω/sq for Cot and OrgCot, respectively.

4.3.1.2 Office Paper and Sticker Label

Similar conditions were implemented on paper substrates and used for comparison with fabric substrates. The R_{Sheet} was measured on samples with 1 to 3 layers combined with G_{Flakes} concentrations of 10, 20 and 30 wt% (**Figure 4.6**). Similarly to what was observed for the fabric substrates, the increase in the number of layers and G_{Flakes} wt% led to a decrease in the R_{Sheet} values of the printed sensing elements. For paper substrates, the observed R_{Sheet} values are not distinctive, probably because they are similar in terms of roughness, porosity, and fibre distribution.

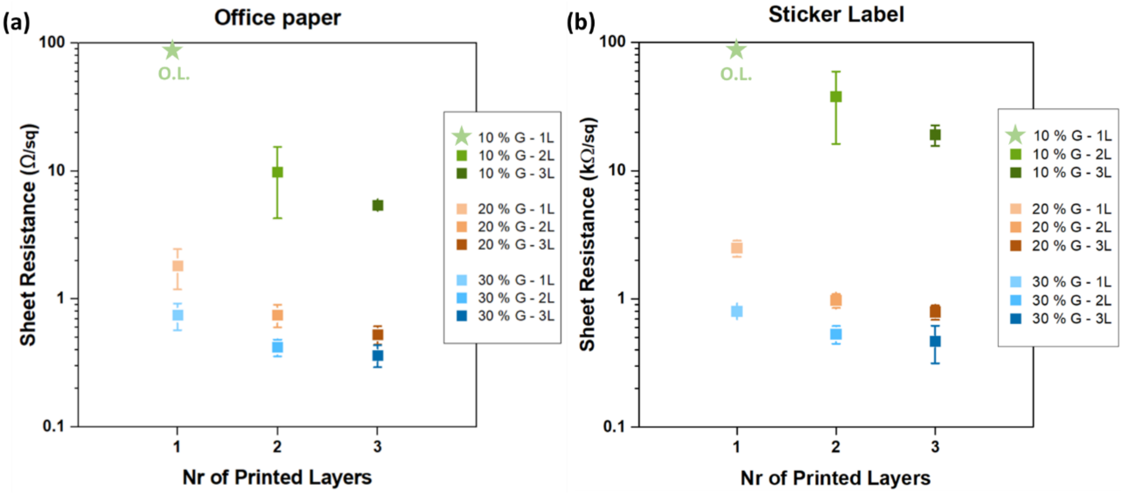

Figure 4.6 - Average sheet resistance values for each number of printed layers (1, 2 or 3 layers) and graphite wt% composition (10%, 20 or to 30 wt%), on: **(a)** office paper, and **(b)** sticker label substrates. The star symbols represent samples that were too electrically resistive (OL situations) to perform the R_{Sheet} measurements.

The SEM images in **Figure 4.7** - **a)** and **b)** show clear differences in the surface topography when compared to the printed fabrics (**Figure 4.5**). The results show a highly efficient fibre covering from 2 printed layers with the 10 wt% of G_{Flakes}, resulting in an immediate electrical percolation. Thus, the ink saturation is more prevalent in paper substrates, which can be explained by the fibre ink absorption as well as the production method of the fabric substrates, which undergo a weaving process leading to higher apertures in between the threads, hence more porous. In contrast, in the paper fibres, the porous size is significantly smaller, and the fibres are more randomly compressed. The ink uptake of the substrate is then controlled by the porosity and fibre absorption, making the fabric substrates better candidates for ink absorption, thus lowering layer saturation and reducing ink consumption. In the extreme condition of 3 layers of 30 wt%, there is an excess in G_{Flakes} ink on the paper substrates, resulting in a common screen-printing defect where the printed layer surface showcases the mesh aperture, like small dots. Although this translates into a rougher surface and ink waste, the R_{Sheet} presents its lowest values of 364 ± 20 Ω/sq and 467 ± 33 Ω/sq for OP and SL, respectively.

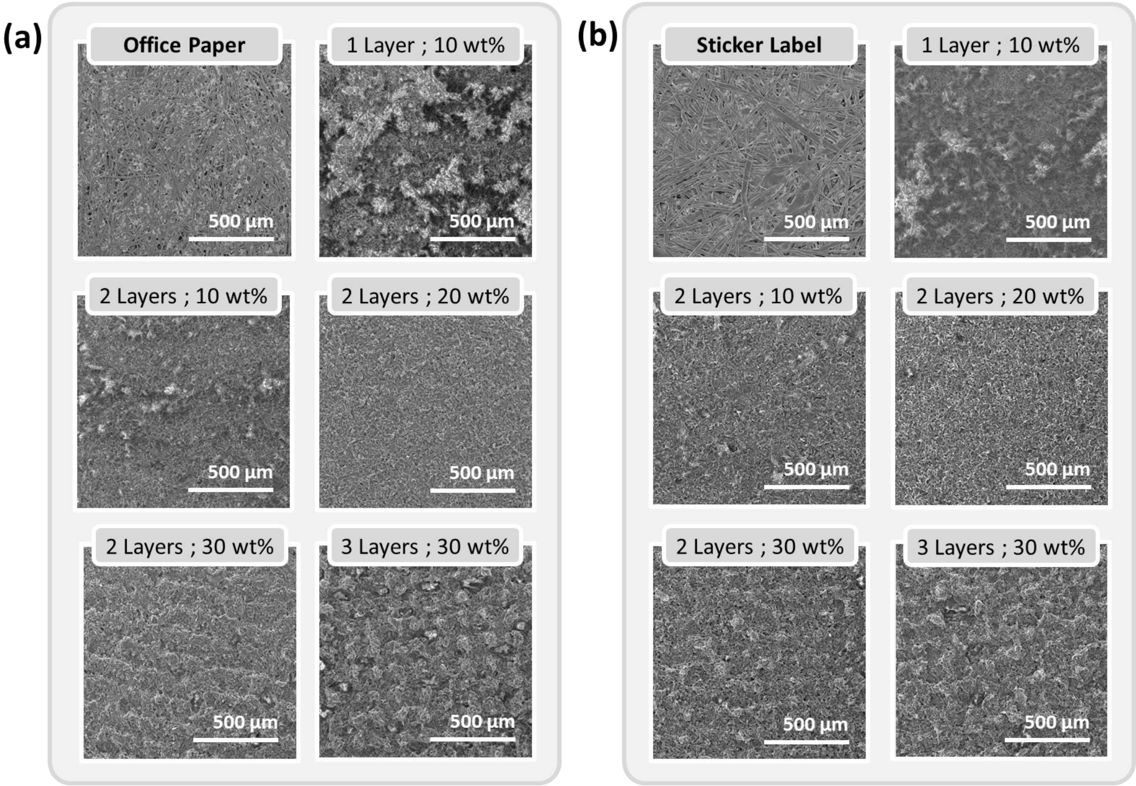

Figure 4.7 - Surface SEM images of screen-printed TE films with different printing conditions (number of printed layers and wt% of G_{Flakes}) on: **(a)** office paper and **(b)** sticker label substrates. For comparison purposes, the first image of each set presents both fabric substrates without TE material (pre-printing).

4.3.2 Touch Detection Tests

The electrical and morphological characterization indicated Cot and OP as the prime printing substrate options and the clear influence of the number of printed layers and G_{Flakes} wt%. Combining both aspects, the optimal conditions for both substrates are 3 printed layers of 30 wt% ink. However, aiming for a reduced device processing time and less expense of the active material amount, as well as a higher flexibility, the option of 2 layers of 20 wt% ink was also addressed on OP (R_{Sheet} of 751 ± 20 Ω/sq) to produce some of the final touch sensors.

The S measurement was performed for elements printed with different conditions to complement the characterization of the samples printed on OP and Cot (**Appendix Figure 2**, **3** and **4**). As expected [98], [114], all values were positive (graphite is reported as a p-type material) and around 20 µV/°C, regardless of the substrate and printing conditions, **Figure 4.8**, showcasing that notwithstanding the differences in R_{Sheet}, for this specific application, we will have similar responses.

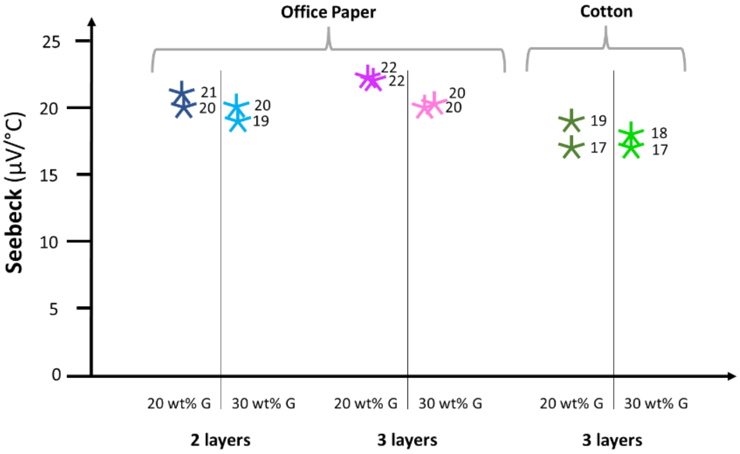

Figure 4.8 - Seebeck coefficient measurement values for different printing conditions using OP and Cot substrates.

The V_{OC} of the samples was measured over time to study the gloved finger touches response of the TE elements. The V_{ON} is the V_{OC} when the sample is experiencing a ΔT due to a finger touch, while V_{OFF} is the V_{OC} when there is no ΔT present. At the beginning of each test, the sample was measured for at least 30 seconds with no ΔT applied to acquire a baseline. After this stabilization time, the stimulation of the sensors began, and the V_{OC} was left to reset to its initial value between touches.

4.3.2.1 Cotton sensors with different number of elements

Figure 4.9 - **(a)** exhibits the positive and negative V_{OC} peaks, which correspond to touches (around 2 s) on each sensor's positive and negative terminals, respectively, where the same sensor can generate two different responses. When TE materials are exposed to a ΔT, the majority of carriers move from the hot side to the cold side, originating an electrical response; hence, the carrier movement will also invert when there is an inversion of the said gradient. Depending on which side the user touches the sensor, this behaviour can be used for a Yes or No application.

Figure 4.9 - b) shows the V_{OC} increase when connecting elements electrically in series, using 1, 2 and 4 elements. The used geometries are shown in the inset images, and the corresponding SNR values, voltage amplitudes (V_{AMP}) and rise/fall times (T_{rise} and T_{fall}, respectively) can be found in **Table 2**. The SNR parameter of a sensor relates the signal amplitude to the background noise (measuring V_{OFF} over time), and its values were calculated using the following **Equation 4.1** [103]:

$$SNR = \frac{V_{ON} - V_{OFF\_mean}}{V_{OFF\_stdev}} \qquad 4.1$$

where V_{OFF_mean} is the average of the background noise before the peak and V_{OFF_stdev} is the standard variation of those V_{OFF} values.

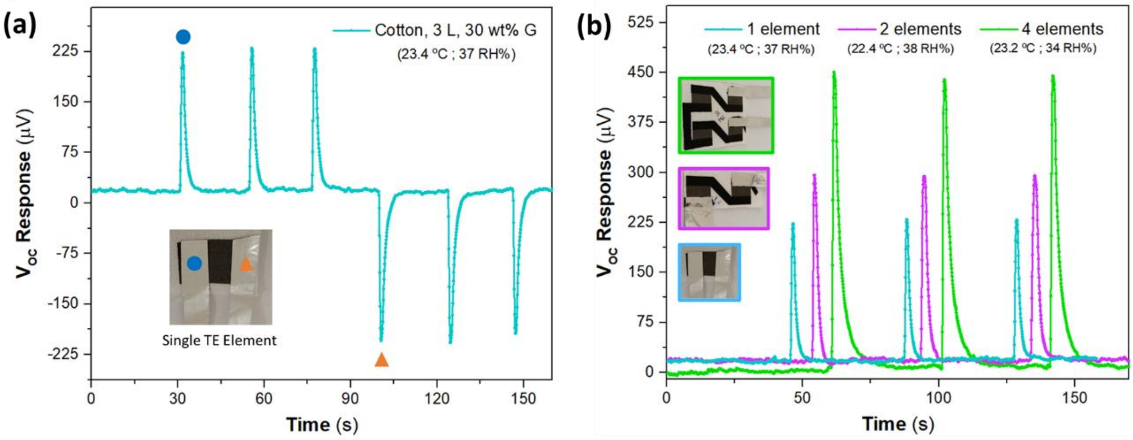

Figure 4.9 - **(a)** Gloved finger touch test for a Yes or No response based on symmetric ΔT – the first three peaks were obtained when touching the left electrode (blue circle) and the last three peaks when touching the right electrode (orange triangle) and **(b)** Comparison of the TE response for touch sensors printed on cotton with 1, 2 and 4 elements connected electrically in series – 3 layers, and 30 wt% G_{Flakes}.

When increasing the number of elements, it raises the SNR value since the maximum V_{ON} increases due to the S sum. At the same time, the noise remains similar for the three cases. Data shows that all tested geometries have a noticeable V_{out} when thermally stimulated (touch ~2 s) and could be used as touch sensors with reproducible V_{OC} responses.

Table 2 - Average values of the SNR, V_{AMP}, T_{rise} ,and T_{fall} for the peaks in **Figure 4.9-b)**.

Number of TE Elements	SNR	V_{AMP} (µV)	Rise Time (s)	Fall Time (s)
1	162 ± 11	209 ± 4	0.63 ± 0.01	4.3 ± 0.5
2	205 ± 50	277 ± 1	0.73 ± 0.23	3.6 ± 0.6
4	244 ± 30	439 ± 10	0.51 ± 0.01	6.2 ± 0.1

The V_{AMP} values scale with the sensor's increasing number of TE elements. In theory [59], when adding in series equal TE elements consisting of p-n junctions, the sum of each element's S value and its electrical resistance will lead to a proportional increase in V_{AMP}. Nevertheless, unlike regular TE devices, these printed sensors have single type TE elements, and the observed behaviour is not the same. The C_{ink} used to connect different elements is responsible for the electrons' diffusion from hot to cold regions, and this is why our carbon paths are diagonal across the sensors with multiple elements. Since C_{ink} has a small S and is p-type, there is a loss in the yield and efficiency of the sensor, escalating with the insertion of more elements. Ideally, using n-type electrical connections between sensing elements instead would overcome this issue. Furthermore, it is essential to consider that the geometry of the serialized elements still needs optimization: firstly, the often-long carbon tracks printed onto an insulator substrate offer additional resistance to the sensor; secondly, as the number of elements increases it becomes more difficult for the finger to touch all the elements uniformly.

The response time is characterized by τ_{rise} and τ_{fall} values, obtained by normalizing the curves and measuring the time required for the voltage to grow from 10 to 90% and decrease from 90 to 10%, respectively [141]. It is observed that the number of elements does not appear to influence the τ_{rise} significantly. However, when it comes to τ_{fall} values, there is a slight decrease when adding sensing elements. We attribute this to the non-uniform stimulation of the sensing elements that will generate differences in ΔT between the hot and cold sides.

4.3.2.2 Cotton and office paper sensors with different printing conditions

Although the initial touch detection tests were performed using the optimal conditions of 3 printed layers of the ink with 30 wt% of G_{Flakes}, a comparison of sensors with different ink formulations and number of printed layers was made using OP as substrate, **Figure 4.10 (a)**. Three faster touches were performed (~2 s) followed by a longer touch (~20 s) to evaluate the V_{OC} and τ_{fall} behaviours for the different sensors.

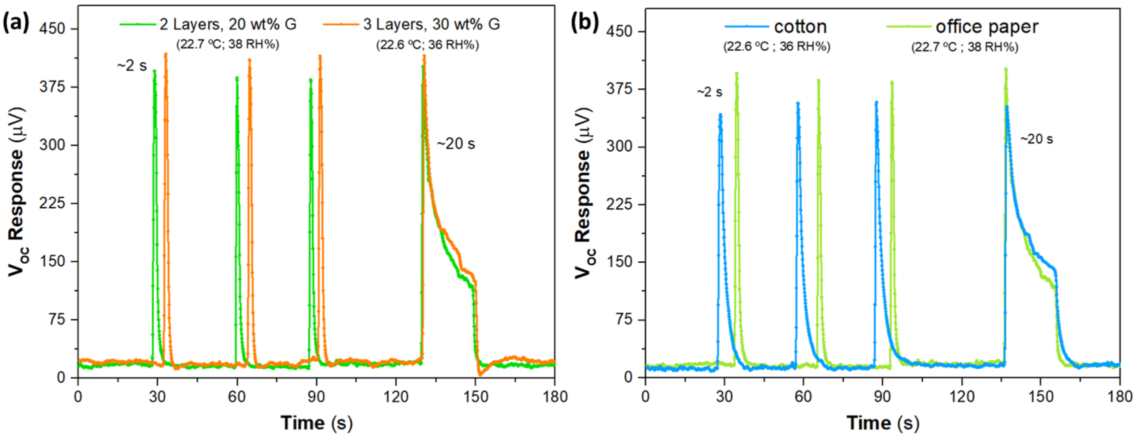

Figure 4.10 - **(a)** Comparison of 4-elements touch sensors printed on office paper with 2 layers of 20 wt% of G_{Flakes}, and 3 layers of 30 wt% of G_{Flakes}, and **(b)** 4-elements touch sensors with 2 layers of 20 wt% of G_{Flakes}, printed on office paper and cotton, for comparison of substrates. In both plots, the initial 3 peaks correspond to fast touches of ~2 s and the fourth peak corresponds to a longer touch during ~20 s.

In general, less resistive TE elements are obtained when the number of printed layers and the G_{Flakes} wt% in inks formulations are increased. Nonetheless, when comparing the SNR values and response times (**Table 3**) of 2 printed layers with 20 wt% of G_{Flakes} and 3 printed layers with 30 wt% of G_{Flakes}, it does not justify using more material to produce each sensor since the S values are similar (**Figure 4.8**). Therefore, to save material and have a faster process, the condition of 2 printed layers with 20 wt% of G_{Flakes} was chosen to perform a test comparing the Cot and OP substrates, **Figure 4.10 (b)**.

Table 3 - Average values of the SNR, V_{AMP}, τ_{rise} and τ_{fall} for the 4-element paper sensors printed with different conditions, **Figure 4.10 (a),** and for **Figure 4.10 (b)**, where sensors printed with 2 layers of 20 wt% of G, printed in different substrates are compared.

Substrates	**Conditions**	**SNR**	**V_{AMP}** (µV)	**Rise Time** (s)	**Fall Time** (s)
Office Paper	2 Layers, 20 wt%	340 ± 51	374 ± 4	0.40 ± 0.12	1.82 ± 0.07
	3 Layers, 30 wt%	295 ± 73	396 ± 3	0.46 ± 0.03	1.36 ± 0.09
Cotton	2 Layers, 20 wt%	326 ± 36	341 ± 9	0.56 ± 0.06	5.67 ± 0.74
Office Paper		322 ± 106	374 ± 5	0.47 ± 0.12	1.85 ± 0.06

Furthermore, the inks with more G_{Flakes} content are expected to have higher *k*, interfering with the response speed in apparently higher V_{AMP} value. However, for a longer touch time and considering the experimental errors introduced by the manual test and possible variation in RT, the difference in the signal is not significant. Thus, the performance of 4-element sensors printed on OP and Cot using 2 layers with 20 wt% of G_{Flakes} was compared (**Figure 4.10 (b)**). **Table 3** presents the SNR, V_{AMP}, τ_{rise} and τ_{fall} values for those samples indicating that the OP substrate is better than Cot, both in terms of V_{AMP} and response times. The response speed is related to the *k* of the TE film/substrate combination, and it is expected that cotton shows a higher thermal resistance, both in absorbing the thermal stimuli and in freeing it back to the environment, since it is thicker than paper and has patterned apertures along the material. To check if faster responses could be achieved, even with small V_{AMP} and SNR values, a touch detection test for shorter touch times was performed using a single element sensor in **Appendix Figure 6**.

4.3.2.3 Bending and Durability

A mechanical bending test was performed to evaluate the endurance of the thermal touch sensor printed with 3 layers of 30 wt% G_{Flakes} on the cotton substrate. These printing conditions were chosen assuming that for thicker films and higher amounts of printed material, the impacts of the cyclic bending tests would be magnified, inducing more surface defects and reducing the performance of the sensor. The 4-element sample was measured before any bending effort and after 50 (red curve) and 100 (blue curve) bending cycles, as can be seen in **Figure 4.11** - **(a)**. Although the recovery time and the electrical resistances increase with the bending stress, we can see that the sensor endured after the 100 bending cycles, maintaining its response.

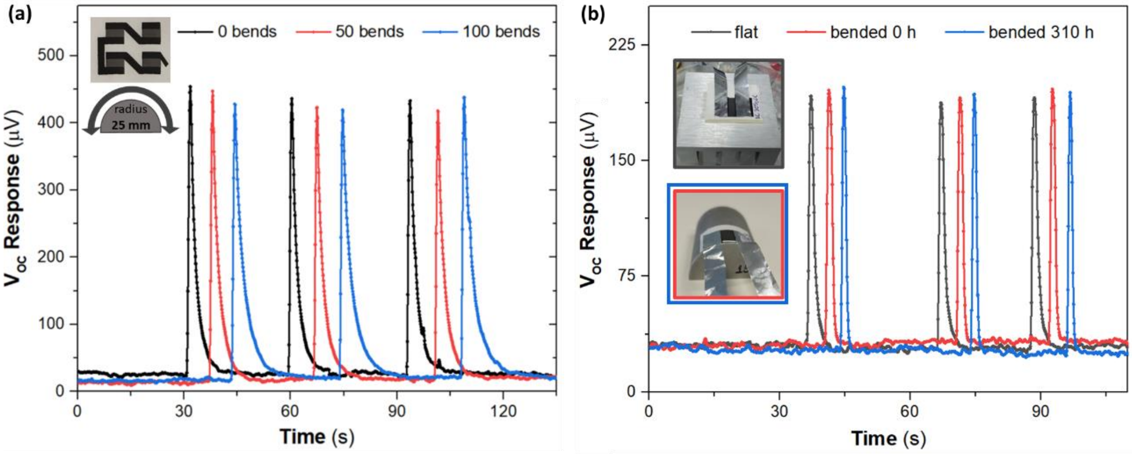

Figure 4.11 - **(a)** Results for a dynamic bending test using a cylinder with 25 mm of curvature radius, with a 4-element sample printed on cotton (3 layers, 30 wt% G_{Flakes}), and **(b)** Static bending test for a single element touch sensor using a sticker label substrate - 3 layers of 30 wt% G_{Flakes} - A cylinder with a 15 mm curvature radius was used.

A single element sensor printed on sticker label substrate, with 3 layers and 30 wt% G_{Flakes}, was tested continuously over a longer bending period of 310 h, with a smaller CR of 15 mm, **Figure 4.11** - **(b)**. The results indicated that the sensor's performance was not affected by this mechanical bending test, and this type of sensor can be used in flexible applications.

Due to the V_{AMP} increase, a series of 16 TE elements was printed and connected to evaluate if it is possible to increase the SNR values. The devices were rolled around a hollow cylindric shape as core, a piece of cardboard straw with 7 mm of diameter (**Figure 4.3 (iv)**), to facilitate the heat collection from a single finger touch. **Figure 4.12** - **(a)** shows the comparison of the output response of sensors printed on OP with different conditions: 2 layers of 20 wt% of G_{Flakes} (purple curve) vs 3 layers of 30 wt% of G_{Flakes} (pink curve) for different touch durations. **Figure 4.12** - **(b)** shows the results for the sample printed with 2 layers and 20 wt% G_{Flakes} after being rolled up for 800 h and stored in a non-vacuum environment. The graphic indicates that the differences between the samples are insignificant, and the sensors' bendability and durability are demonstrated. The embedded image is of a sensor printed on cotton instead of paper so that the printed elements can be seen transparently, and the temperature gradient and electron flow scheme can be better understood.

For the final proof-of-concept of output signal improvement, 48 elements were connected electrically in series (3x16 elements arrays), using OP as substrate (**Figure 4.13**). With this planar-vertical configuration, the response for one gloved finger touch was maximized, surpassing 4.5 mV.

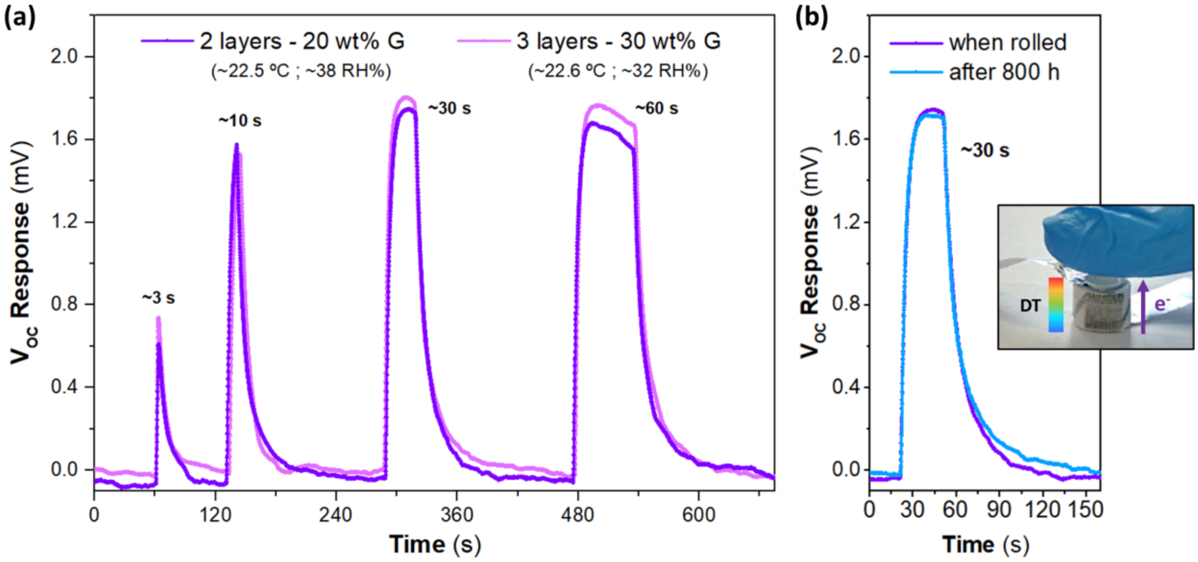

Figure 4.12 - Comparison of 16-elements connected electrically in series, printed on paper with different conditions: **(a)** the dark purple curve is of a sample with 2 printed layers of 20 wt% G_{Flakes}, and the light purple is of a sample with 3 layers of 30 wt% G_{Flakes}, both measured for four different time lapses and **(b)** the sample in dark purple being remeasured for a ~30 s touch stimulus after 800 h rolled up. An inset image of a planar/vertical sensor printed on cotton being subjected to a gloved finger touch is shown.

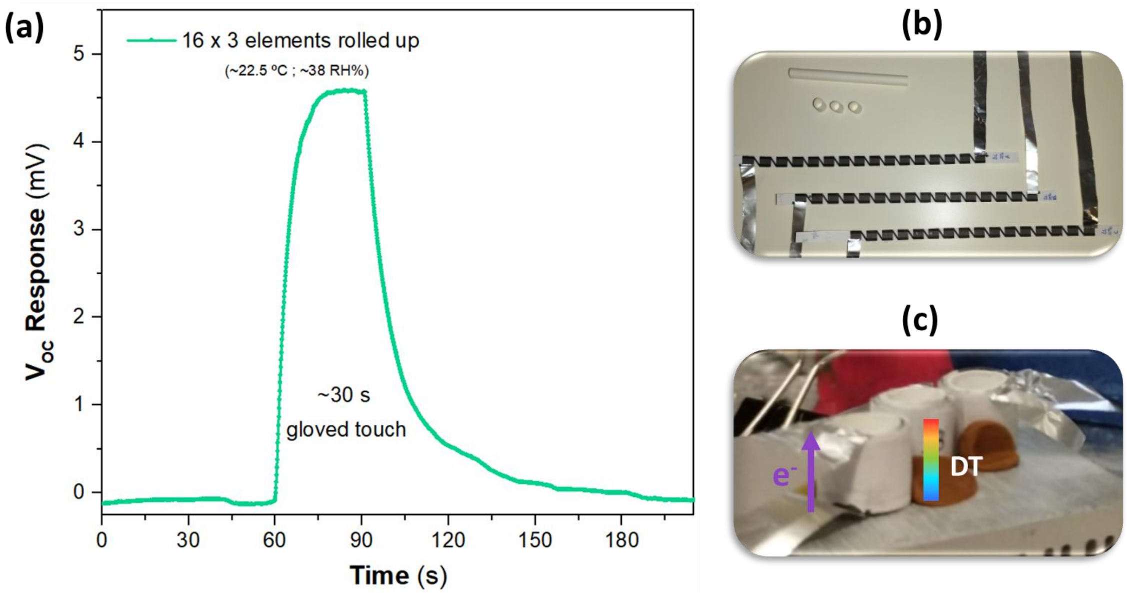

Figure 4.13 - **(a)** Voltage response (V_{OC}) of 3 rolled arrays of 16 TE elements, totalling 48 elements connected electrically in series, printed on office paper, with 2 layers and 20 wt% G_{Flakes}, with the touch stimulus during for ~30 s; **(b)** the 16-elements printed arrays before the wrapping step around cardboard hollow cylinders and **(c)** the 3 rolled arrays in the potentiostat characterization setup.

4.3.3 Encapsulation Step

This section presents the results for three different encapsulant materials for flexible and screen-printed TE touch sensors on paper and cotton substrates. The chosen encapsulant materials were ethyl cellulose and polyvinyl alcohol - deposited using blade-coating - and commercial plastic pouches utilising an office laminator. The EC and PVA are flexible encapsulants and compatible with printing techniques. Since EC is a cellulose-based material, it is an eco-friendlier choice that, to the best of our knowledge, was used for the first time as an encapsulant for flexible electronic devices.

Before going deeper into the results, we must consider two aspects: the used paper as printing substrate and the user performing the touch tests (see **Appendix Figure 5**) were different from the previous sections.

4.3.3.1 SEM Imaging

SEM images in **Figure 4.14** - **(a)** and - **(b)** reveal the differences between the two substrates used to print the TE sensors before and after the PVA and EC encapsulation step. It was assumed that the laminated samples present a smooth and good surface coverage independently of the substrate used, as the laminator equipment applies a thicker plastic cover to substrates using pressure, heat, and their internal roller mechanism. So, their SEM evaluation is not addressed.

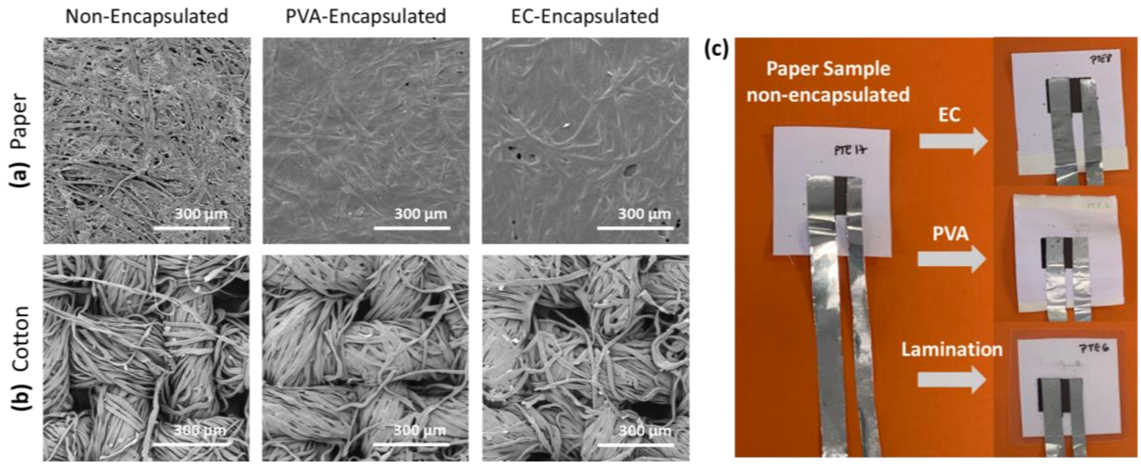

Figure 4.14 - **(a)** and **(b)** SEM images for paper samples and cotton samples, respectively, before encapsulation, and after PVA and EC encapsulation; **(c)** Real images of the TE sensors, before and after the encapsulation with EC, PVA and plastic pouch lamination, where the transparency of all the tested encapsulant materials can be attested.

PVA and EC covered the paper surface uniformly, filling the pores between the fibres and lining their walls. As for the cotton substrate, although the fibre threads seem to be covered, the gaps between them are too big to be filled with the encapsulant material, so the cotton remains porous. However, as seen in a previous section regarding the production of TE sensors, the TE ink itself helps to cover the substrates, which will make the encapsulation more effective on top of an already printed paper or cotton. Encapsulated samples after bending were also analysed, but there were no visible differences from the non-bent samples. In **Figure 4.14** - **(c)**, we can confirm that both EC and PVA result in transparent encapsulation layers. The samples encapsulated with a laminated plastic pouch are also presented for comparison.

4.3.3.2 DSC Analysis and Viscosity

The DSC analysis of the three encapsulant materials studied in this work and the results are shown in **Figure 4.15** - **(a)**, demonstrating that all of them are thermally stable up to 150 °C. For applications that require higher process and/or working temperatures, it is necessary to consider a loss of 2% of mass registered at 162 °C, 276 °C and 381 °C for PVA, EC and plastic lamination, respectively. Moreover, a loss of 10% of mass was detected at 307 °C, 315 °C and 408 °C for PVA, EC and plastic lamination, respectively. That being said, the PVA shows a faster degradation when compared with EC, while the plastic lamination is suitable if higher temperatures (> 250 °C) are needed, despite the loss in flexibility.

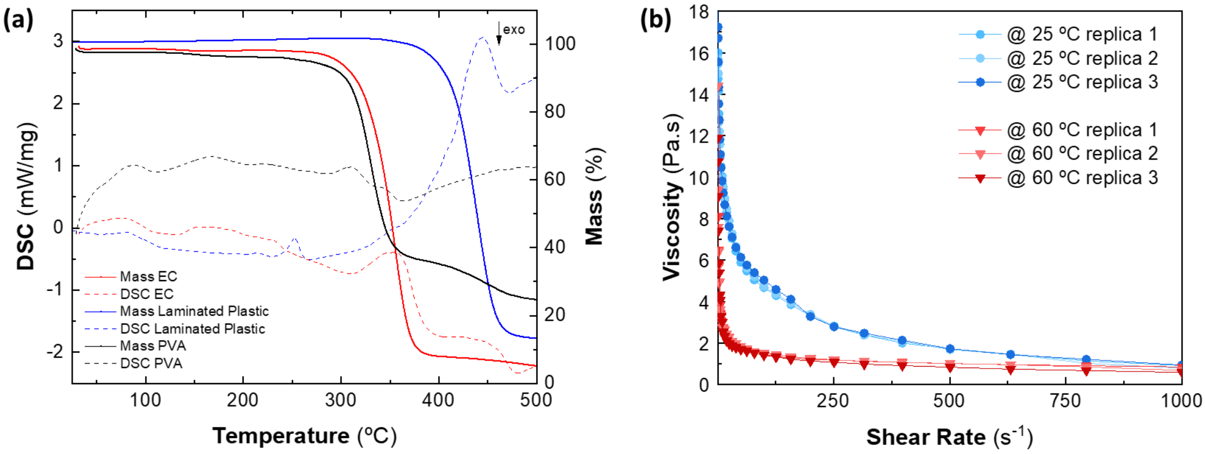

Figure 4.15 - **(a)** DSC analysis for the 3 used encapsulant materials and **(b)** viscosity results for the EC solution, at 25 and 60 °C.

The dynamic viscosity of commercial PVA is 9000-15000 mPa.s (depending on the dilution), according to the manufacturer's technical datasheet [213]. The EC ink absolute viscosity measured in the rheometer for a shear rate of 500 s^{-1} was 1711 ± 26 mPa.s at 25 °C and 955 ± 118 mPa.s at 60 °C (by the production and deposition temperatures, respectively), **Figure 4.15** - **(b)**. These results show that both inks are compatible and suitable for different printed techniques, such as screen-printing, dispenser-printing and blade coating, making the encapsulation process easily up-scalable [209], [210].

4.3.3.3 Contact Angle

Contact angle measurements were performed to assess the wettability of the substrates before and after the encapsulation step. The CA was also determined after 100 bending cycles with a 15 mm curvature radius. Finally, it was assessed the devices' water resistance submerging them in water for

1 min. Before encapsulation, and as expected [214], [215], paper and cotton were extremely hydrophilic, quickly absorbing the water droplets, meaning the measured CA was close to zero. Consequently, this shows that if the non-encapsulated sensors were wet or submerged in water, they would degrade quickly in terms of electrical performance or even fail to work. The CA values are compiled in **Figure 4.16**, where we can easily conclude that all the encapsulant materials promoted considerable changes in sample surface wettability. The light-coloured columns correspond to measurements after 1 min (to let the droplet stabilize on the surface), and the darker columns refer to measurements after 5 min (to see if there were significant changes).

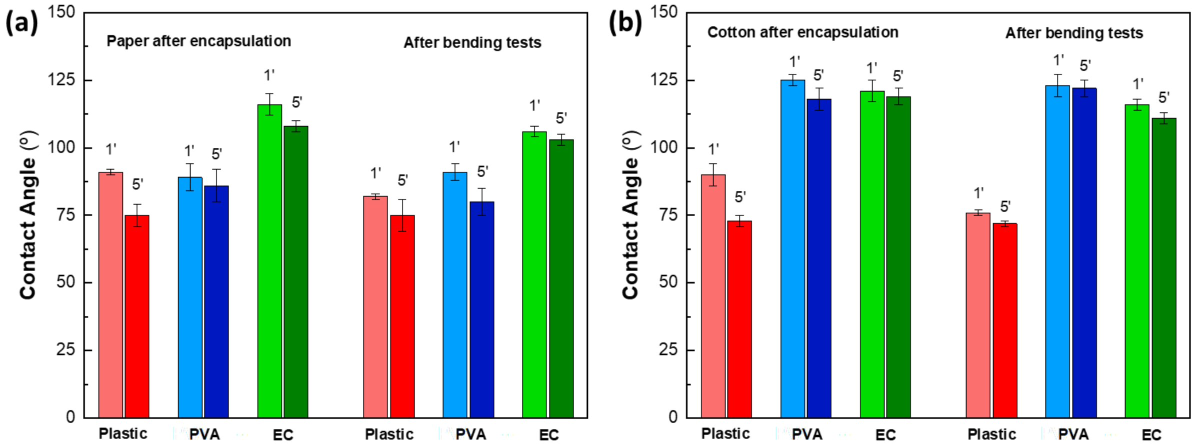

Figure 4.16 - Contact angle values measured with three different encapsulant materials, after 1 and 5 minutes of having the water droplet on the samples surface, for **(a)** paper and **(b)** cotton samples. The first three column sets are prior to bending tests, and the last three were measured after.

Regarding the laminated samples, the CA was very similar for both substrates, as expected. Thus, unlike the other two types of encapsulation materials, the laminated plastic surface gives smaller CA values after 5 minutes due to evaporation and spreading of water on the surface itself due to the low surface energy of the laminated plastic.

Considering the cotton sample with PVA and EC encapsulation, the CA values are higher when compared with laminated plastic, meaning that, although the plastic surface is entirely impermeable to water, the encapsulating materials EC and PVA make the surface more hydrophobic, increasing the CA value and keeping it for longer. The EC mixture worked well for both substrates using a blade-coated layer with a 4 µm rod. Although the PVA encapsulation for cotton showed slightly higher CA values, the difference is not significant.

Contrary to what happened with the cotton samples, the PVA encapsulation (1:7 ratio) with a single 4 µm rod passage was inefficient in promoting an effective water barrier on paper substrates, which absorbed the water droplet completely, resulting in a CA value close to zero after 5 min (see **Appendix Table 1**). Since PVA was highly diluted in water, and despite the deposition being made at 60 °C, the fibres immediately soaked the solvent and the PVA encapsulated sensors' performance was very different compared to the cotton ones. To overcome this issue, various approaches were experimented. Initially, a 90 µm film applicator was employed to explore the possibility of enhancing PVA deposition and improving results. Additionally, a new PVA: water ratio (3:2 V/V) in the solution's formulation was tested, increasing the polymer in the mixture. Unfortunately, none of these attempts yielded compelling results. Consequently, the following strategy was to increase the number of printed layers while maintaining a constant 4 µm thickness. This adjustment significantly enhanced the encapsulation of the paper samples, leading to higher CA values compared to the previous attempts (see **Appendix Table 1**), but it made the encapsulation step much longer due to the drying times between passages and sides. Although this approach improved the results, the CA values were ~30° lower than for the cotton samples for all the tests. As for the EC encapsulation, the CA was very similar for both substrates and proved to be the more efficient encapsulant for all the tested scenarios, even after 1 min water submersion (see **Figure 4.21 - (b)**).

4.3.3.4 Encapsulated TE Touch Detectors

The V_{OC} response of the encapsulated TE sensors to gloved finger touches was measured over time, being the V_{AMP}, the difference between the V_{ON} and V_{OFF} states of the sensor's response.

The bending tests performed with paper and cotton TE sensors encapsulated with EC show that the sensors worked even after 100 dynamic bending cycles with a 15 mm CR, **Figure 4.17**. Although they presented smaller V_{AMP} and longer τ_{fall}, the response signal was still relevant (~100 µV), and the τ_{Rise} remained below 1 s.

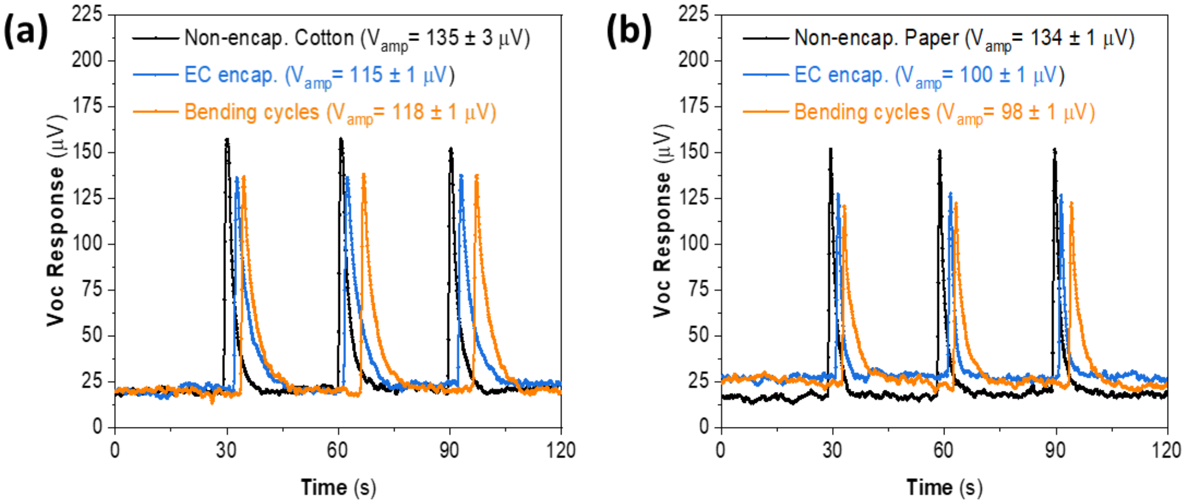

Figure 4.17 - Open circuit potential results for three consecutive finger touch events (~2 s each). Both samples were characterized before and after the EC encapsulation, and after 100 bending cycles for: **(a)** encapsulated cotton and **(b)** encapsulated paper samples.

In each plot, we can see that part of the V_{AMP} loss occurs right after the encapsulation step. This happens because one more layer is added to the sensor, making it harder for the thermal stimulus to reach the electrode and making it difficult for the heat to dissipate after the finger removal, increasing the off-state recovery times.

In the case of cotton samples encapsulated with one layer of PVA, **Figure 4.18** - **(a)**, the performance of the sensors after bending is similar to the EC encapsulation. However, for encapsulated paper samples with two PVA passages (the explanation can be found in the CA discussion in section **4.3.3.3**), the results show a relevant decrease in V_{AMP} with the bending stress test for PVA encapsulation, **Figure 4.18** - **(b)**. Therefore, the EC encapsulation is better suited for flexible paper sensors not only because it has a lower impact on their performance but also due to its more straightforward and faster process.

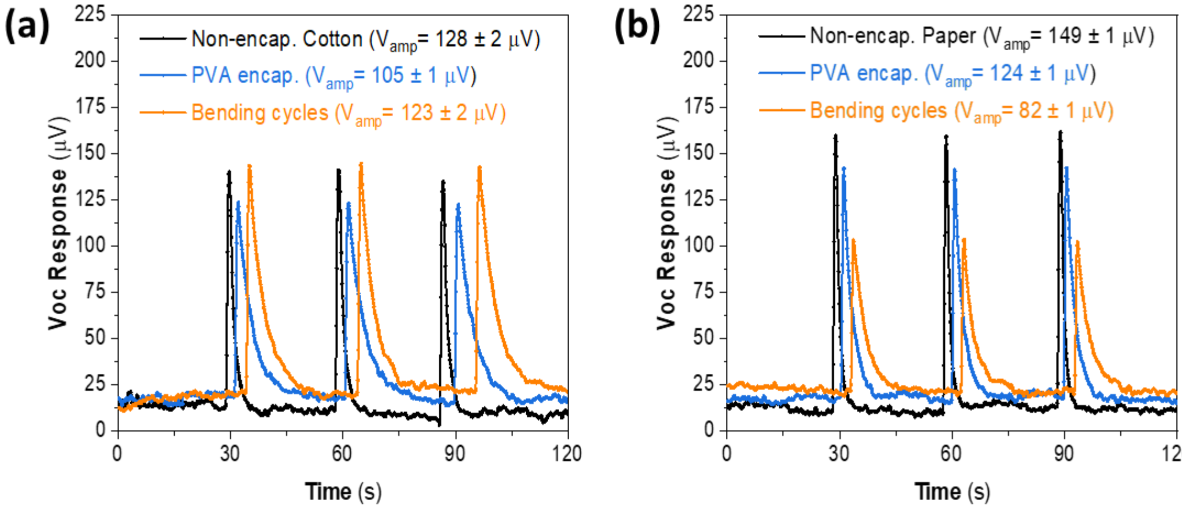

Figure 4.18 - Open circuit potential results for three consecutive finger touch events (~2 s each). Both samples were characterized before and after the PVA encapsulation, and after the bending tests for: **(a)** encapsulated cotton sample and **(b)** encapsulated paper sample.

For comparison purposes, cotton and paper samples encapsulated with laminated plastic were also studied for the same tests used for EC and PVA, as shown in **Figure 4.19**. There was no gain in using laminated plastic to encapsulate these TE sensors once the results showed that the V_{AMP} still decreased, and the response times also got longer. Even in terms of transparency, all the studied encapsulants are transparent, as can be seen in **Figure 4.14** - **(c)**. Moreover, the thicker plastic encapsulant layer makes the samples seem more rigid and heavier than the other encapsulants. This can be relevant for some applications where flexibility and weight can be crucial.

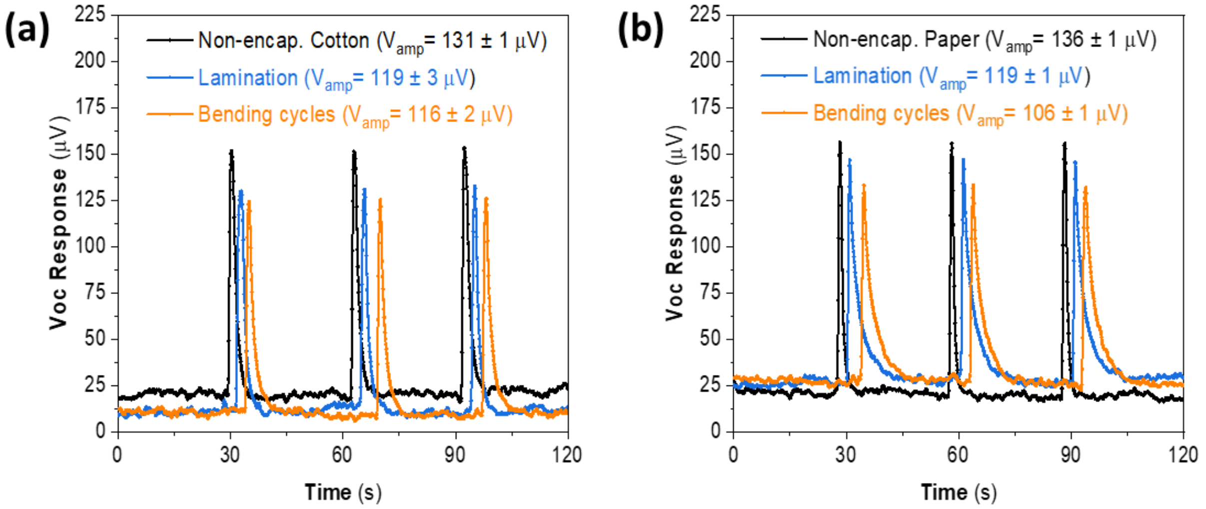

Figure 4.19 - Open circuit potential results for three consecutive finger touch events (~2 s each). Both samples were characterised before and after the plastic lamination, and after the bending tests: **(a)** cotton and **(b)** paper samples.

Figure 4.20 presents the remeasurement of two cotton samples after 10 weeks (in the air) of their initial characterization; one was encapsulated with EC and the other with PVA. Despite the already mentioned V_{AMP} decrease induced by the encapsulation layer, the ageing test for the EC encapsulation seems to add another V_{AMP} loss, **Figure 4.20** - **(a)**, which appears not to be the case when evaluating the PVA encapsulation in **Figure 4.20** - **(b)**. However, since these are manual tests and the RT can have little variations, these differences are not significant, and these results show that both sensors remained functional, retaining their responsiveness.

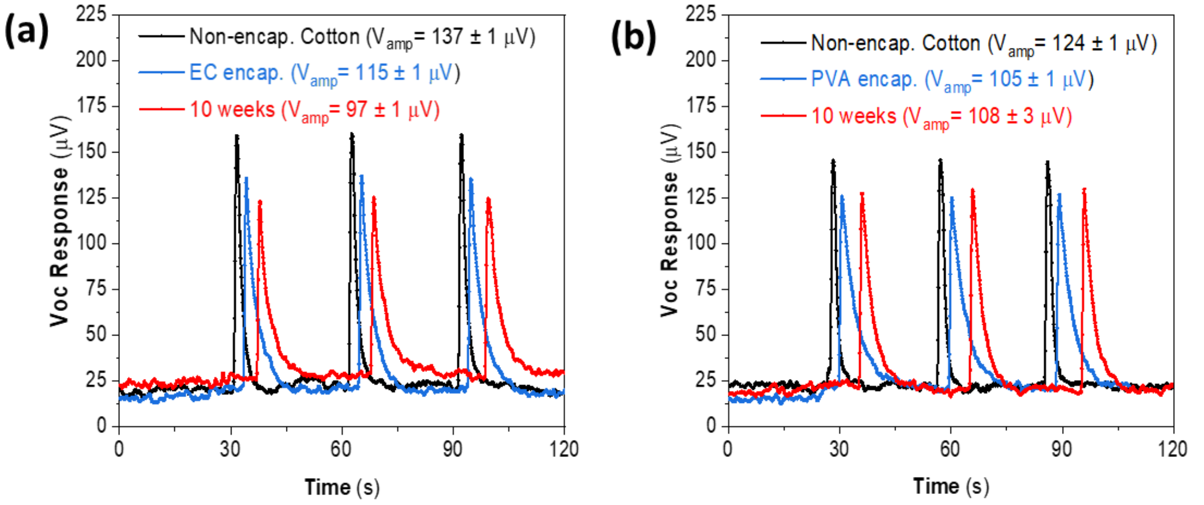

Figure 4.20 - Open circuit potential results for three consecutive finger touch events (~2 s each). Characterization of cotton samples before and after the encapsulation, and remeasurement after 10 weeks, for **(a)** EC and **(b)** PVA encapsulations.

Another finger touch test was done with a paper sample, encapsulated with EC, and submitted to the water submersion test, **Figure 4.21**. Once again, there is a V_{AMP} loss after the encapsulation step and after the submersion test, and τ_{fall} increases from 2.7 (initial) to 4.7 s (after submersion). Nonetheless, the τ_{rise} maintains (~0.5 s), and the peaks are still very well discriminated.

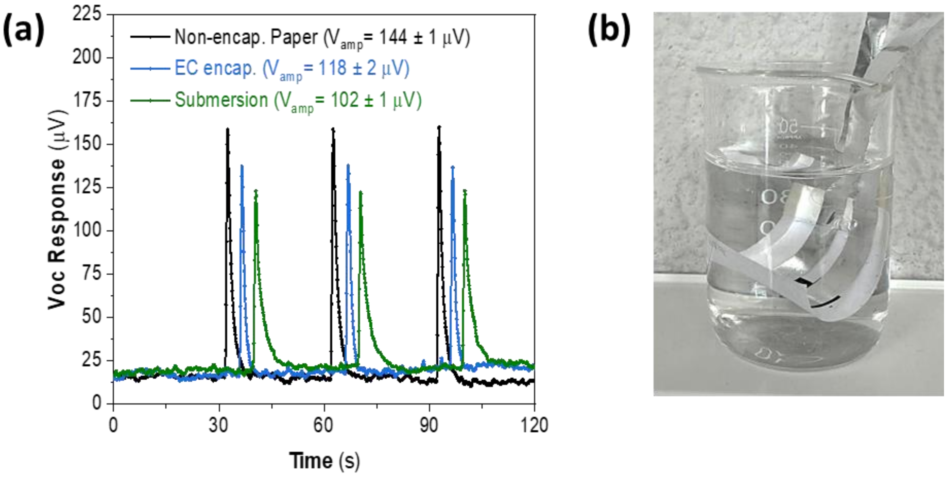

Figure 4.21 - **(a)** Open circuit potential results for three consecutive finger touch events (~2 s each) - Characterization of a paper sample before and after the EC encapsulation and remeasurement after 1 minute submerged in water. **(b)** Image of the sample during the submersion test.

4.4 Conclusions

4.4.1 Printed and Flexible TE Touch Detectors

In previous sections, the formulation and screen-printing of inks based on G_{Flakes}/EC were studied, varying the G concentration (10, 20 and 30 wt%), the number of printed layers (1, 2 or 3 layers) and the printing substrate (OP, SL, Cot and OrgCot). The optimization of these sensors involved the choice of the ideal ink formulation, printing conditions and substrate set, and the adequate architecture/geometry for the determined application – detect human gloved touches.

The optimal printing conditions were two printed layers with 20 wt% of G_{Flakes} since they allow the saving of material and a faster production process, on office paper substrate, showing an excellent electrical-thermoelectric output combination.

The bending tests showed that the sensor performance was not affected by the mechanical stress, revealing a high flexibility with curvature radii down to 7 mm. Indeed, it was demonstrated that with sensors with up to 48 elements rolled up, it was possible to reach more than 4.5 mV of output voltage response promoted by gloved finger touch. Fast and repeatable touch recognition was obtained in optimized devices with a signal-to-noise ratio of up to 340 and rise times below 0.5 s.

However, for fast and repeatable touch recognition, the best choice suggests fewer elements, where response times below half a second can be achieved.

For low-T applications, flexible, lightweight, and low-cost TE devices were obtained using eco-friendly materials and processes. The results prove that the screen-printed graphite-based inks are highly suitable for flexible TE sensing applications. Different combinations of TE elements can be designed and printed using compatible and up-scalable R2R technologies.

Thermoelectric sensors can discriminate different finger temperatures and can distinguish fast touches from long touches. Remarkably, the thermoelectric devices allow the user to read two responses, depending on which side/electrode they touch. The twist of the thermal gradient direction between the electrodes of the sensor could be interesting in applications such as Yes or NO responses, namely in communication with patients with diseases (e.g. speech) [216], and this is not possible in other simple and low-cost sensors, resistive or capacitive.

The main goal was to highlight that this kind of flexible sensors combines the advantages of simplicity of production and operation, functioning for naked or gloved finger touches without pressure. They incorporate eco-friendly and low-cost materials, are easily available, and are produced without needing p-n junctions or several film layers and complex geometric microstructure designs [217], [218]. Therewithal, they do not require vacuum systems or high temperatures in their manufacturing process. This is relevant because it promotes alternatives for the commonly used thermoelectric materials and processes [147], [219].

4.4.2 Encapsulant Materials

The ethyl cellulose showed promising flexibility, water resistance, and transparency properties while presenting a low carbon footprint. Thermoelectric touch sensors encapsulated with this green material maintained their electric characteristics even after submersion in water and bending cycles (response times below 1 s and signals ~100 µV). These achievements with this new application of EC as an encapsulant are highly promising and desirable towards large-area manufacturing compatibility for the future of printed electronics.

Although the laminated plastic provides a water-impermeable surface independent of the substrate, the contact angle measurements showed that the EC and the PVA promote a complete change in the wettability of nonencapsulated paper and cotton, increasing its waterproof ability. Additionally, after full submersion in water the measured contact angles were higher than in laminated plastic, revealing a higher surface hydrophobicity. SEM surface imaging shows a smoother and less porous surface for both paper and cotton samples after EC and PVA encapsulation.

The laminated plastic and EC showed excellent thermal stabilities for lower temperatures (up to 200 °C), compatible with the chosen application for these studies and other flexible substrates.

As for applying these encapsulants in flexible TE sensors, we found that regardless of the encapsulation approach, there was a loss in V_{OC} and longer recovery times, after the encapsulation step, which was expected, since we are adding thermal resistance to the system. Nonetheless, all three encapsulation approaches allowed for proper touch detection. The response signal remained relevant (~100 µV), and the rise times kept below 1 s.

The EC was defined as the desirable encapsulant not only due to the electrical response of the TE touch sensors both on paper and on cotton substrates but also because, unlike PVA, it is an eco-friendly choice. Moreover, it required only a single blade coating deposition step (a desirable feature for large-scale manufacturing). Due to its viscosity, it can be applied in future using other techniques such as screen-printing and dispenser-printing, for instance. This proposed encapsulation material is expected to be useful for TE touch sensors and other printed and flexible electronic devices using diverse substrates.

5

PDMS AND GRAPHITE COMPOSITES

Disclaimer

Some excerpts of this section have been published in the following publications:

Figueira, J.; Loureiro, J.; Vieira, E. M. F.; Fortunato, E.; Martins, R.; Pereira, L. *Flexible, scalable, and efficient thermoelectric touch detector based on PDMS and graphite flakes.* Flexible and Printed Electronics **2021**, 6 (4). https://doi.org/10.1088/2058-8585/ac45de.

Figueira, J.; Vieira, E. M. F.; Loureiro, J.; Correia, J. H.; Fortunato, E.; Martins, R.; Pereira, L. *Composites Based on PDMS and Graphite Flakes for Thermoelectric Sensing Applications*. Materials Proceedings **2022**, 8 (1), 42. https://doi.org/10.3390/materproc2022008042.

5.1 Introduction

As explored in the previous **Chapter 4**, after testing the use of G_{Flakes} in SP ink formulations in paper and cotton substrates, it was found that this material has a p-type conduction, with S around 20 µV/K and R_{Sheet} that could go lower than 400 Ω/sq. The flexible and low-cost TE sensors produced with these inks were stable, showing fast and repeatable touch recognition.

This chapter presents another method to produce flexible and biocompatible TE sensors with G_{Flakes}, using them as a filler in PDMS matrices. This way, different geometries can be easily moulded, and flexible architectures with TE properties can be achieved, requiring only a low T curing step.

In the first section, planar architectures with single TE elements are studied, varying the G_{Flakes} filling content, and their flexibility is assessed. A proof-of-concept for a *Yes* or *No* application is explored. In the following section, vertical sensors are presented with a fixed composition while varying their thickness and thermal contact areas. Touch detection and temperature sensing are evaluated as proof-of-concept for the latter architecture. Also, a new composite made with PDMS and cork granules, involving 16 vertical elements connected in series, is tested as an encapsulant material.

5.2 Planar Sensors

This section presents planar and freestanding (no substrate needed) thermoelectric touch detectors of conductive G_{Flakes} (functional material) into a PDMS matrix.

The device enables a *Yes* or *No* response depending on the touched pad. Different composites were developed by changing the graphite flakes weight concentration (40, 45 and 50 wt%). The TE performance was evaluated and correlated with the morphological results. Moreover, the touch detector properties were investigated for the 45 wt% G_{Flakes} composite with optimized properties.

5.2.1 Experimental Details

5.2.1.1 Materials

PDMS (184 Silicone Elastomer Base and 184 Silicone Elastomer Curing Agent) was purchased from SYLGARD™, and graphite flakes, G_{Flakes} (mesh 325, 99.8 %, metal basis) were purchased from Alfa Aesar®, and used as received. Commercial carbon screen paste (CRSN2644, from SunChemical®) and commercial aluminium foil (12 µm thick) were used to create the electrodes and conductive paths.

5.2.1.2 Samples and Devices Preparation Materials

To prepare the PDMS, the elastomer base and the curing agent were mixed (in a 10:1 ratio) and taken to the exicator to remove the air bubbles formed during their reaction. Different amounts of G_{Flakes} (10, 40, 45 and 50 wt%) were manually mixed till a homogeneous mixture was achieved. This mixture was once again put in the exicator, although this time, much less air bubbles can come out since the viscosity in most cases is extremely high at this point. The experiments observed that composites with wt% of G_{Flakes} higher than 50% become very difficult to dispense due to the high viscosity. Therefore, the composite tends to break, since the PDMS can no longer agglomerate the G_{Flakes}. On the other hand, below 40 wt% of G_{Flakes}, the composites become highly resistive (≈ few M Ω), which makes it impossible to connect several elements in a series, for example. Furthermore, when increasing the PDMS content, the deformations on PDMS due to volumetric contractions and expansions when varying the medium temperature will break the electrical connection between the graphite flakes, leading to variations in the resistance of the composites, which is not desirable in this case of study.

To achieve homogeneous thin films, the samples were obtained by blade coating or film casting the composite mixtures (depending on the amount of graphite flakes) and then cured at 70 °C in an oven, the time dependent on the thickness of the samples (usually between 35 and 50 minutes). After the curing step, the material was detached from the support substrate (acetate sheet), and robust samples with thicknesses between ≈ 0.2 and ≈ 1.1 mm were obtained without any need for substrate. Afterwards, these films were cut in the desired shape, and the electrical connections between elements were made, using C_{ink} to glue the Al foil, having a drying/curing step of 30 minutes at 100 °C in a hot plate. The mixture and blade coating processes and the desiccator and oven steps were optimized to obtain homogeneous mats and cut samples, with reproducible results for the tested thicknesses.

A scheme of the described process can be seen in **Figure 5.1**. The graphite supplier specifies that the morphology is flaked, and that the particles size is adequate for the 325-mesh used in screen printing process, meaning that particles need to have a dimension bellow 44 µm to pass its openings. This information is confirmed by SEM image (**Figure 5.1**, left side), where we observe G_{Flakes} with a wide range of sizes but not exceeding ≈ 40 µm.

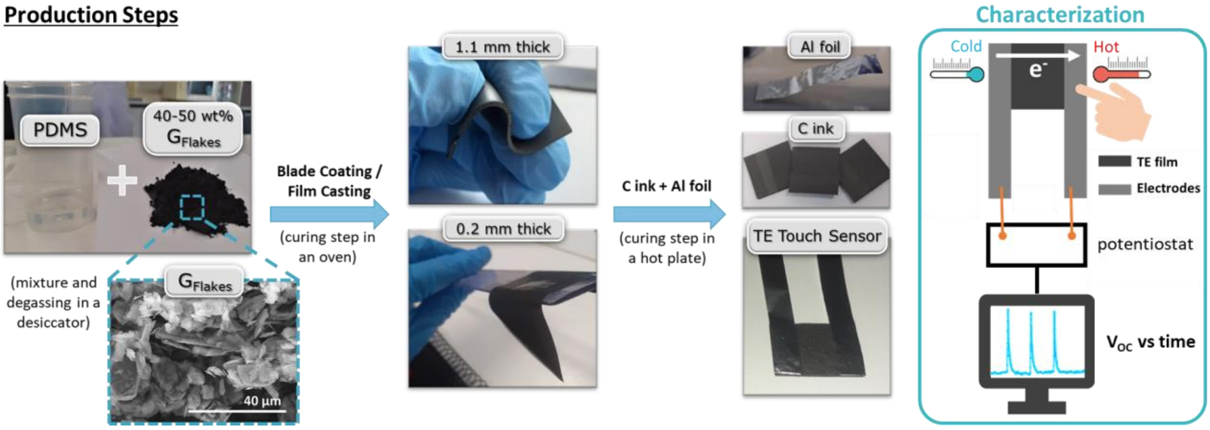

Figure 5.1 - Scheme of the production steps to obtain PDMS/G composite planar samples and an exemplification of a gloved touch event during characterization. A representative SEM image of the used commercial G_{Flakes} is also shown.

5.2.1.3 Samples and Devices Characterization

The morphology of G_{Flakes} of the casted films was examined by SEM (**section 3.2.5**). The Seebeck coefficient of PDMS: G_{Flakes} samples was measured at RT in a planar configuration using a homemade setup based on the 'two-probe' method (**section 3.2.3**). The carrier Hall mobility, electrical conductivity and carrier concentration were measured with the Hall effect system using van der Pauw contact geometry (**section 3.2.2**).

The TE responses of the samples were obtained using a potentiostat in a configuration where the open circuit potential (V_{OC}) is measured over time while touching (or not touching) the sample with the gloved finger (**section 3.2.1**).

Flexibility tests were done by touch detection characterization while resorting the device to static and dynamic bending stresses, using cylinders with curvature radii of 45, 25 and 15 mm. The effect of long-period bending stress was also evaluated by fixing the device over the smallest curvature radius cylinder (15 mm) and characterizing the evolution of its touch detection performance and electrical properties over time.

5.2.2 Results and Discussion

In **Figure 5.2** - **(a)**, **(b)**, and **(c)** we can see SEM images, with the same magnification, showing the G_{Flakes} as purchased, the composite produced with the less wt% of G_{Flakes} (electrical insulant) and the composite with the maximum G_{Flakes} content (electrical conductor), respectively. In another set of SEM images with a smaller magnification, **Figure 5.2** - **(d)**, **(e)** and **(f)**, we can see the surface of the three composites characterized in this section, with G_{Flakes} contents of 40, 45 and 50 wt%, respectively. As can be seen, the viscosity of the PDMS mixture increases with the G_{Flakes}' weight content, therefore, the ability to originate a smooth surface drastically decreases from 40 up to 50 wt% G_{Flakes}.

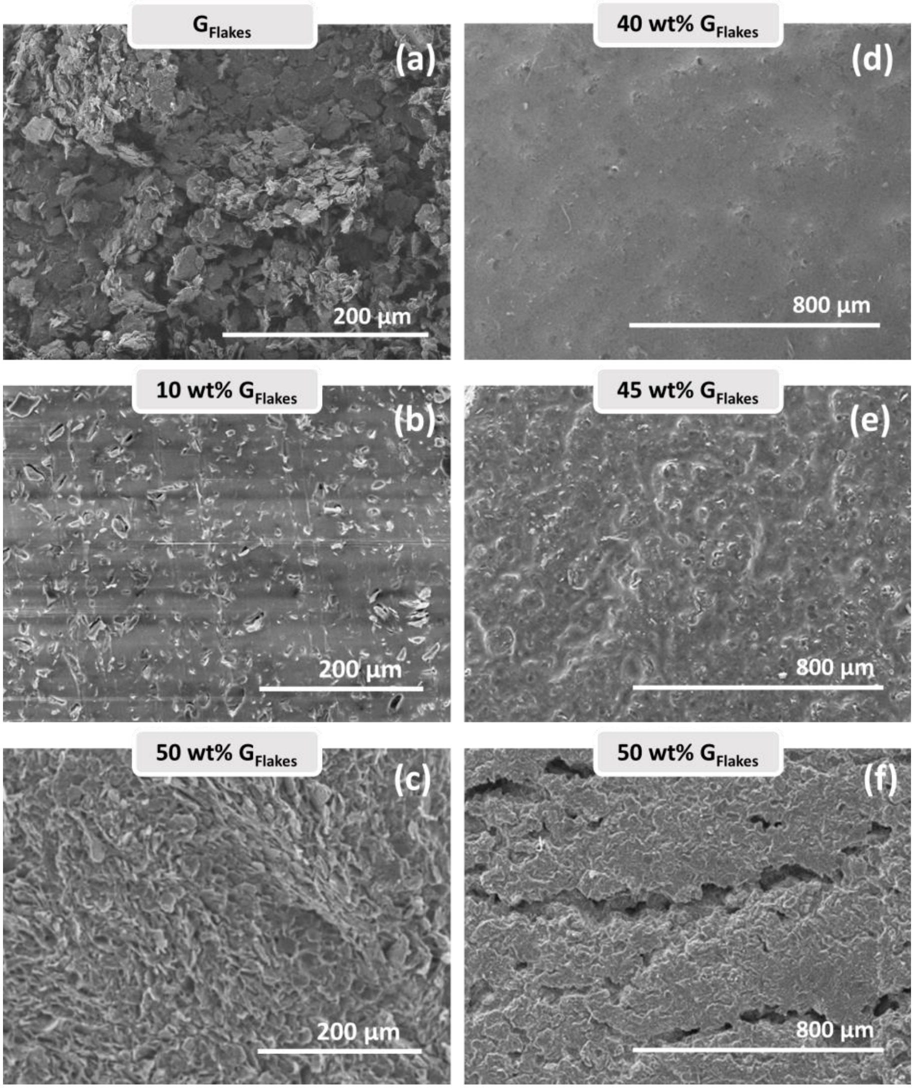

Figure 5.2 - Morphological characterization using SEM analysis of the: **(a)** G_{Flakes} as purchased; **(b)** and **(c)** composites with the minimum (10 wt%) and maximum (50 wt%) of G_{Flakes} contents, respectively; **(d)**, **(e)** and **(f)** characterized composites, with G_{Flakes} content of 40, 45 and 50 wt%, respectively.

Regarding processability, it is much easier to mix and cast mixtures up to 45 wt%, leading to more robust and homogeneous samples than with 50 wt% (where the cohesion limits are being surpassed). Mixtures up to 45 wt% enabled the film casting technique, with an adjustable micrometer film applicator moved by an automatic arm. With this method, films with thickness down to 0.2 mm were obtained for the 40 wt% G_{Flakes}. For the 50 wt% mixture, a blade coating technique had to be used instead of the film casting one because the film started to break apart while being cast.

Hall effect measurements were carried out on samples with different G_{Flakes} wt%, and the main results are depicted in **Figure 5.3** - **(a)**. When the G_{Flakes} wt% increased from 40 to 50 wt%, the mobility of the majority carriers decreased from 2.7 to 0.1 $cm^2.V^{-1}.s^{-1}$ (orange triangles) while their concentration maintained a similar increase. Increasing the G_{Flakes} wt% in the composite results in a loss of the polymer content, which significantly enhances the carriers' concentration of the material and, at the same time, reduces their mobility even with fewer interfaces between the two different materials [220]. Although this so-called trade-off happens because the collisions between carriers increase with the increase of carrier concentration [221], there is an electrical conductivity improvement by almost two orders of magnitude (green stars).

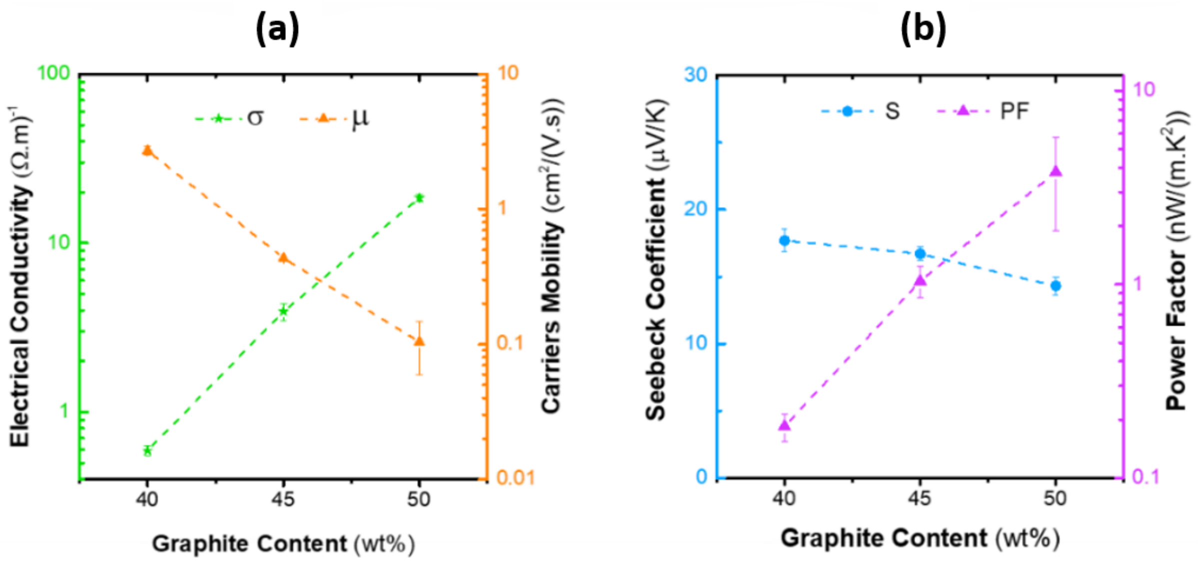

Figure 5.3 - Graphics of **(a)** Electrical conductivity and carriers' mobility, obtained through Hall Effect measurement, and **(b)** Seebeck coefficient and Power Factor of composite samples, as function of the G_{Flakes} content. Error bars are also shown.

As expected and presented in **Figure 5.3** - **(b)**, the S is positive (blue circles), indicating a p-type material (meaning the majority carriers are holes), and it slightly decreases as the G_{Flakes} wt% increases. These S values are in accordance with previously published results [114], where a similar value (+18 μV/K) was described for bulk graphite samples. The slight S decrease from 18 μV/K to 14 μV/K alongside the σ increment is once again a well-known trade-off due to the existence of more carriers [222], [223]. Evaluating these graphite percentage-dependent properties, we conclude that there is a PF enhancement (purple triangles), from 0.19 to 3.8 nW/(m.K^2) for G_{Flakes} wt% from 40 to 50, respectively. Besides these interesting TE results, it is essential to emphasize that this composite is low-cost, environmentally friendly, flexible, available, biocompatible, and benefits easy processing. Furthermore, this composite can be used to build TE elements that do not need any substrate, therefore minimizing the thermal contact resistance between the electrical device and the heat sink [222].

Human touch detection was chosen as the proof-of-concept application for the developed composites. In **Figure 5.4**, the open circuit voltage shows the effect of touching (1-2 s of thermal contact) on one of the electrodes, V_{ON}. Briefly, after the event, the signal returns to the initial state, V_{OFF}. The touch response was the same despite the wt% G_{Flakes}. The on-state voltage is the response to the temperature rise caused by the finger touch and has no relation to skin interaction since equivalent results were obtained with the finger covered. In **Figure 5.4**, the SNR value is presented for each touching peak, which evaluates the signal's amplitude against the noise. The maximum of 130.4 is achieved for the 45 wt% G_{Flakes} device (green curve).

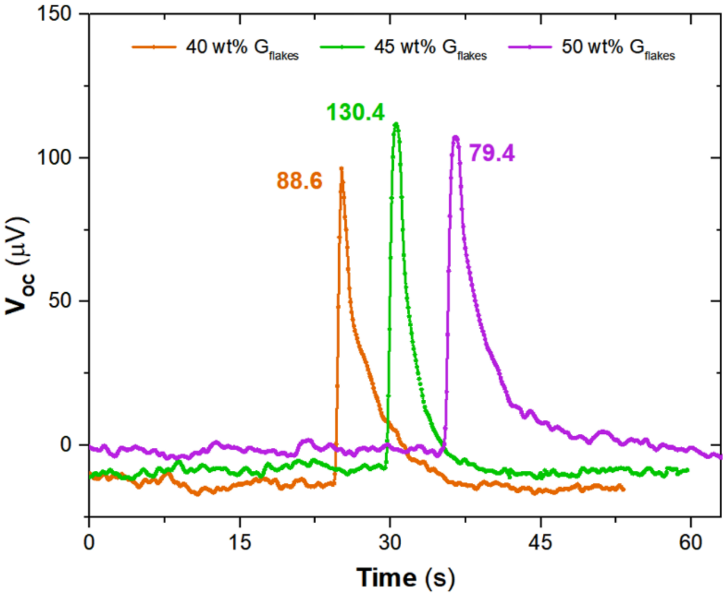

Figure 5.4 - Thermoelectric voltage response of the PDMS/G_{Flakes} devices to finger touch events during ~2 s. Each colour corresponds to different G_{Flakes} wt%. Signal-to-noise ratio values are depicted for each touching peak. The difference in time between the signal peaks is promoted for better visualization.

The 50 wt% device is the one with the lowest SNR, and this composite presented the highest PF but the lowest S of the three being tested. Although the 50 wt% composite has shown the best PF, it also reveals the lowest S value, which is more important than σ when referring to this type of application. Regarding thermal conductivity, the higher the composite *k*, the higher the risk of interferences in the thermal gradient created by the finger touch. Based on the literature [224], we can predict that *k* increases with the amount of G_{Flakes} added to the PDMS. The PDMS *k* is around 0.2 W/(m.K) [114], [124], while for bulk graphite flakes, a k ~ 1.4 W/(m.k) was reported [114]. This said, and because SEM images also show that the 45 wt% G_{Flakes} samples are more homogeneous and without visible cracks, this was the chosen composition to perform other touching tests.

A device with 45 wt% G_{Flakes} was characterized in different bending configurations to check the possibility of being used in applications where bending is relevant. In the first test, the device was measured while bent with three different curvature radii, using metallic cylinders (**Figure 5.5** - **(a)**) with a CR of 15, 25 and 45 mm. In **Figure 5.5** - **(b)** it is shown the device voltage response to touch while being bent, starting with the largest curvature radius, 45 mm (blue curve), passing to 25 mm (orange curve) and ending with the smallest CR, 15 mm (purple curve). The results show that the device's behaviour is not affected by the curvature radii, neither in terms of time response nor in the SNR value (showing only a slight decrease of 10% when the CR decreased to 15 mm).

An extended static test was performed with the device being characterized over 40 h while fixed on a surface with a curvature radius of 15 mm. **Figure 5.5** - **(c)** shows the results immediately after the bending step (light green curve), 20 h after it (yellow curve) and finally 40 h after (orange curve). It was observed that even when bent with a 15 mm CR during 40 h, continuously, the device behaviour keeps similar to the planar measurement one, both in terms of time response and SNR values. The only characteristic that slightly changed is the V_{OFF}, which is correlated to increased device resistance due to the bending stress (which is triplicated when comparing the starting time point with the 40 h time point). However, it does not affect the device SNR.

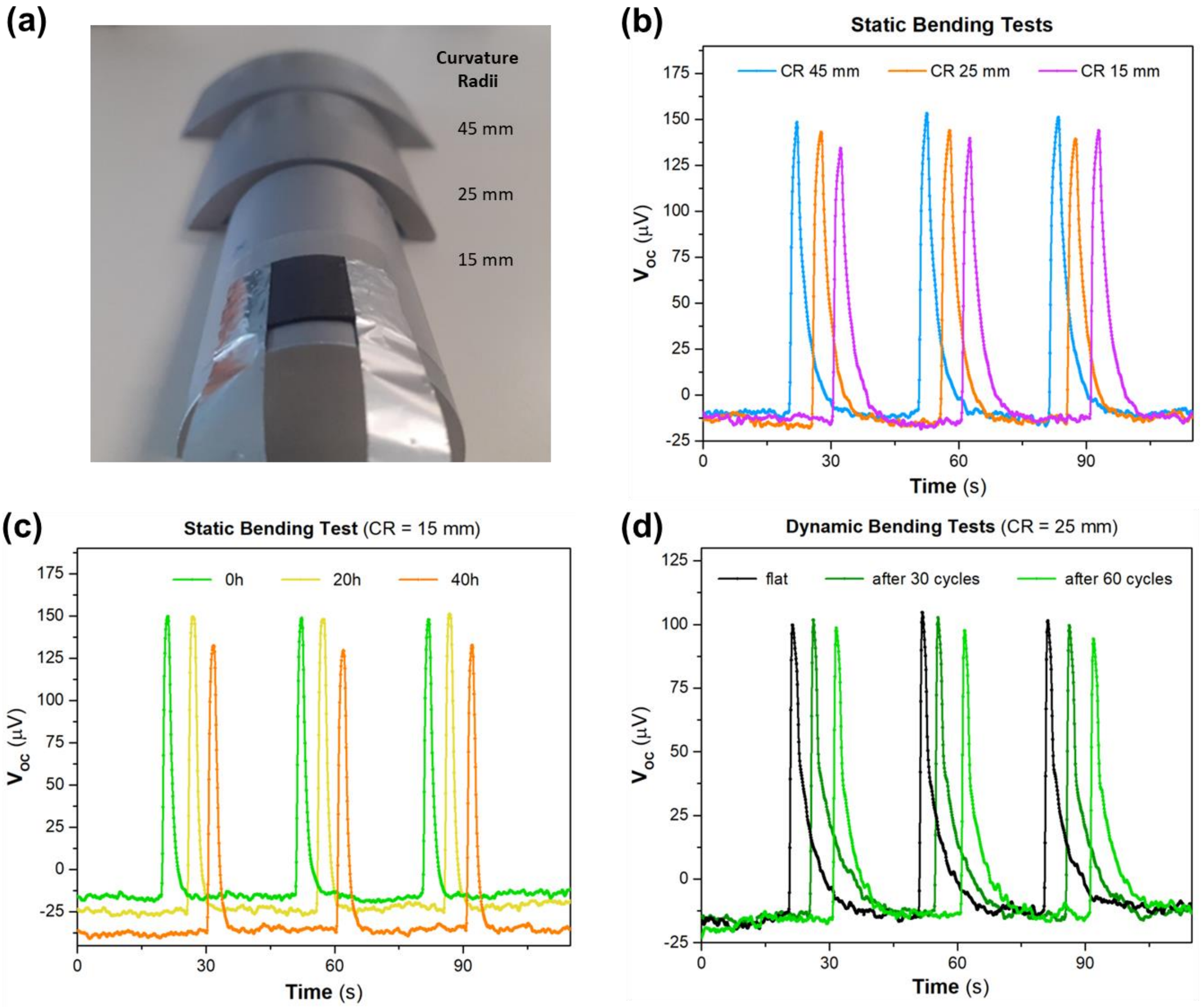

Figure 5.5 - **(a)** Metallic cylinders with different curvature radii, 45, 25 and 15 mm; **(b)** static bending test results using the three different metallic cylinders; **(c)** static bending tests on the 15 mm cylinder, over time, up to 40 h and **(d)** dynamic bending tests using the 25 mm cylinder, up to 60 bending cycles. The difference in time between the signal peaks is promoted for better visualization.

Regarding dynamic stress evaluation (**Figure 5.5** - **(d)**), the test started with the device being characterized in a flat mode (black curve). It was submitted to 30 bending cycles with 25 mm CR and, once again, characterized in a flat mode (dark green curve). Afterwards, the same sequence was repeated, completing 60 cycles in total (light green curve). As in the two previous bending tests, it can be observed that the device behaviour is not affected by the dynamic bending test (the SNR and time responses are kept constant over the cycling).

The bending tests performed and depicted in **Figure 5.5** also show that the V_{ON} value is larger when the device is measured over a curved surface rather than measured in a flat mode. This is probably explained by the type of surface where the device is characterized rather than any explanation associated with the curvature itself. The cylinders used for the bending tests are metallic, which means they act as dissipators and contribute to an increase of the thermal gradient arising from the finger touch, consequently increasing the V_{ON}.

5.2.2.1 *Yes* or *No* Application

When a TE material is subjected to a thermal gradient, the majority of carriers move from the hot to the cold side, which means that when we have a p-type material, the holes flow from the hot to the cold side, and electrons go the other way around. If the thermal gradient direction is inverted, carriers will also invert their path, originating a symmetric electrical response (if the measurement system remains unchanged).

The distance between contacts has an influence on the thermal gradient since it affects the time needed to reach a thermal equilibrium between sites. Decreasing the contact distance means decreasing the thermal gradient and, consequently, the V_{ON} value. The area of the electrodes, which is available for heat collection, also interferes with the V_{ON} value. Larger metallic pads can collect heat more efficiently than smaller ones (as the finger touch area increases). This said electrode design plays a vital role in the device performance, and they can be optimized for higher and faster SNR values or even manipulated to have asymmetric positive/negative peaks.

In **Figure 5.6** - **(a)**, there is a scheme of the quick *Yes* or *No* response test, showing the results from a sample tested in a flat mode (**Figure 5.6** - **(b)**) and bended with a 15 mm curvature radius (**Figure 5.6** - **(c)**). Besides the previously explained differences in the V_{ON} (due to the metallic surface of the cylinder), the performance of the device is the same in the two situations, with SNR consistently above 100, proving again that it can be used both in flat mode and bent (at least down to a 15 mm curvature radius). The touch detector response time, which is reflected in the τ_{rise} and τ_{fall}, was calculated by normalizing the curves and measuring the time required for the V_{OC} to increase from 10 to 90 %, and then to decrease from 90 to 10 % of its maximum value.

Results show fast rise times, always below 1 s for both configurations. Regarding the recovery times, and because the thermal conductivity of the characterization supports is different, values below 7 s were observed for the flat mode, which has a lower *k*. Smaller values, below 3 s, were observed for the bent mode, which has a higher k that helps the thermal gradient ~ 0 K state recovery. These results mean that these devices can be used for fast/real-time human touch electrical trigger/detectors using standard electronics (like Arduino) to read the output voltages.

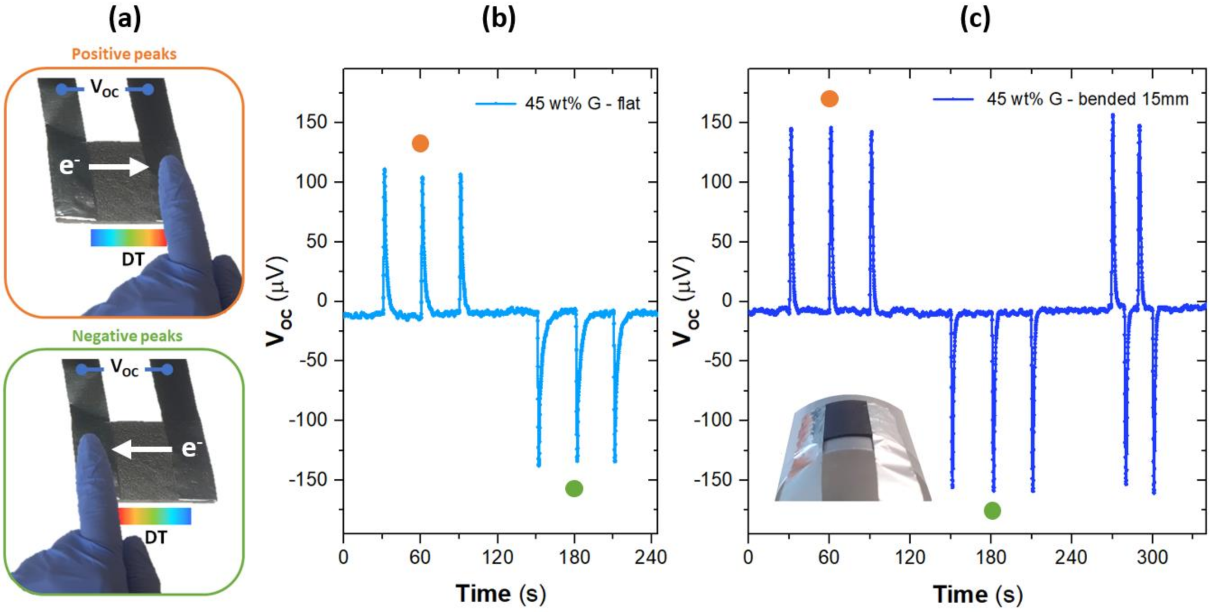

Figure 5.6 - **(a)** Gloved finger touch scheme for a *Yes* and *No* response test based on symmetric thermal gradients and inverse electrons movement directions; V_{OC} electrical characterization during a touch detection test where both electrodes were stimulated (in an alternate manner) in: **(b)** a flat configuration and **(c)** in a bended configuration with a 15 mm curvature radius.

5.3 Vertical Sensors

The previous section reported the production of flexible planar TE touch detectors based on PDMS/G_{Flakes} composites, studying the influence of the graphite content variation in the mixture. Here, the results of TE sensors based on the composite with 45 wt% of G_{Flakes} (see **Appendix Figure 7**) and vertically assembled will be presented. These sensors are used for touch detection and temperature-sensing applications. In this study, the geometries of the TE elements change, and the electrical connection of several elements in a series was assessed. An encapsulation step was included, using an electrical and thermal insulator made of a PDMS/cork composite.

5.3.1 Experimental Details

5.3.1.1 Materials

PDMS (184 Silicone Elastomer Base and 184 Silicone Elastomer Curing Agent) was purchased from SYLGARD™, and graphite flakes, G_{Flakes} (mesh 325, 99.8 %, metal basis) were purchased from Alfa

Aesar®, and used as received. Commercial carbon screen paste (CRSN2644, from SunChemical®) and commercial aluminium foil (12 µm thick) were used to create the electrodes and conductive paths. Commercial wine cork stoppers waste is chosen based on their non-agglomerated nature, i.e., single pieces of natural cork.

5.3.1.2 Samples and Devices Preparation

Figure 5.7 shows the thermoelectric devices' manufacturing process, from the synthesis of the composite (with 45 wt% of G_{Flakes}) to the device assembling and characterization, with photographs of each step to obtain vertical flexible thermoelectric devices. A detailed process to obtain these composite mixtures was explained in **section 5.2.1**. The PDMS/G_{Flakes} samples were prepared through a blade coating process, reaching different thicknesses, and cut into small blocks with other areas. Afterwards, electrical connections were made with carbon ink + Al foil to form different thermoelectric detecting/sensing devices.

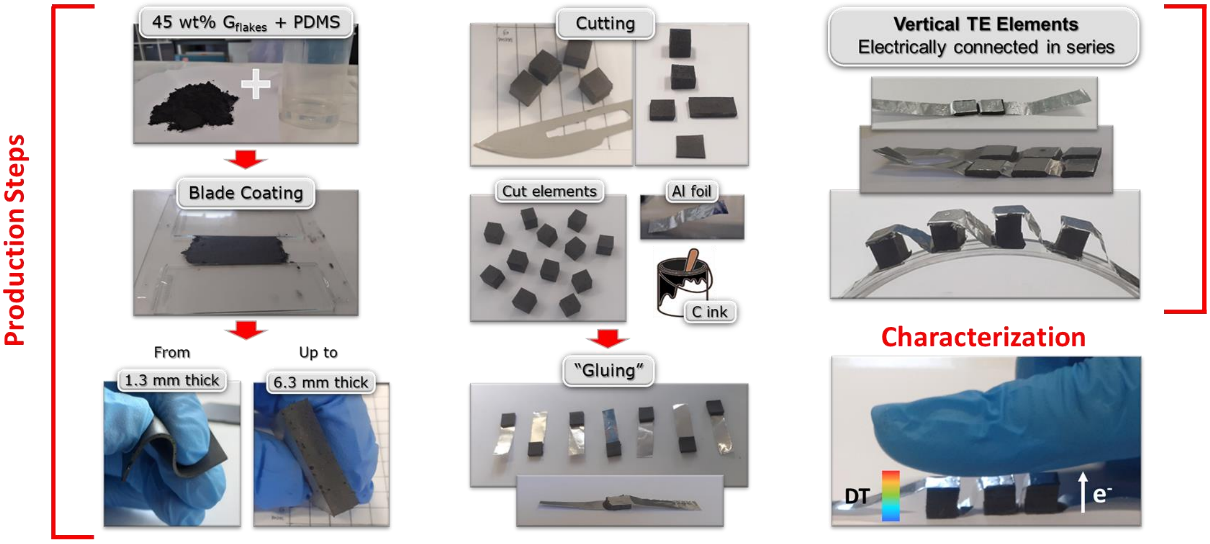

Figure 5.7 - Scheme of the production steps to obtain blade coated PDMS/G composite vertical samples, varying their thicknesses, and an exemplification of a gloved touch event during the characterization of a 3-elements sensor.

5.3.1.3 Encapsulation Step

The encapsulant material tested as a gap-filler for vertical PDMS/G_{Flakes} sensors was a PDMS/cork composite, produced as described in **Figure 5.8**.

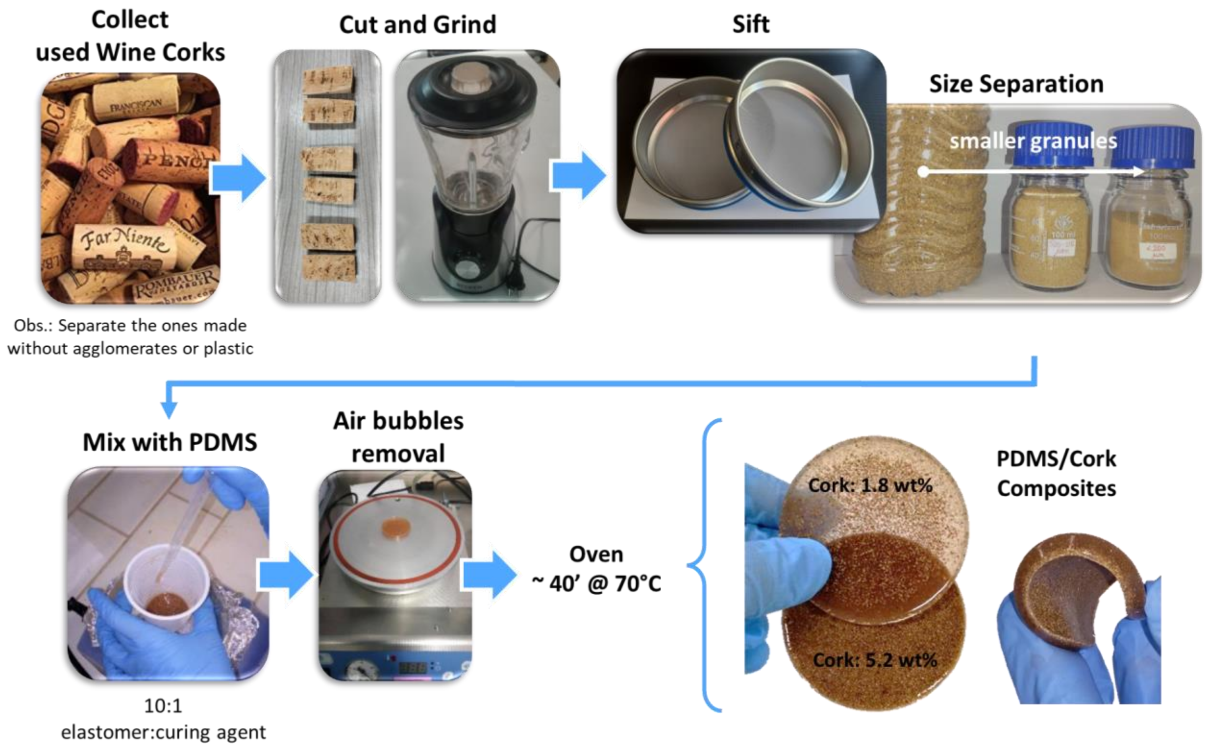

Figure 5.8 - Schematic of the production steps to obtain the PDMS/Cork composite samples, from the cork wastes griding to the manipulation process of PDMS. Examples of final samples with cork granulates <500 µm, varying the wt% of cork.

The optimized PDMS/cork composite was used to evolve the TE sensor elements, filling the gaps between them, as seen in **Figure 5.9**.

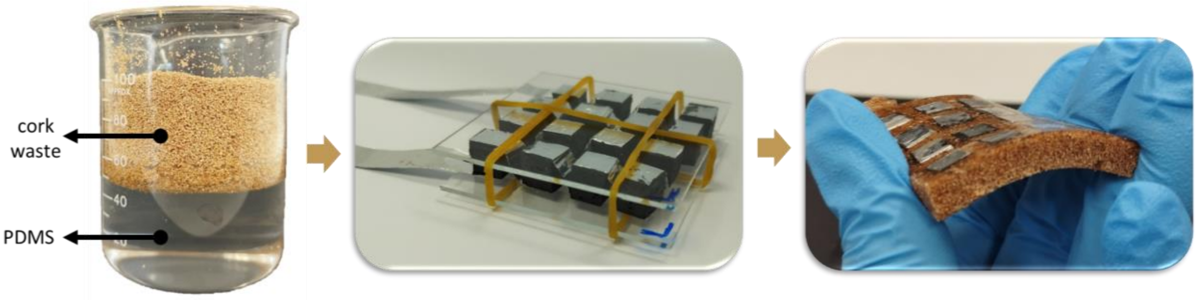

Figure 5.9 - Encapsulation process to obtain a dual PDMS composite: PDMS/G_{Flakes} elements (an electrical conductor with thermoelectric properties) surrounded by a PDMS/cork mixture (an electrical and thermal insulant material).

5.3.1.4 Samples and Devices Characterization

The TE responses of the samples were obtained using a potentiostat in a configuration where the open circuit potential (V_{OC}) is measured over time while touching (or not touching) the sample with the gloved finger (**section 3.2.1**). The PDMS/cork composite was examined by SEM (**section 3.2.5**). The volumetric mass density of each PDMS/cork composite composition was calculated by measuring the weight for 6 replicas of cubes cut with dimensions of 5x5x5 mm^3.

5.3.2 Results and Discussion

5.3.2.1 TE Elements with Different Thicknesses

We studied the response to a gloved touch by using devices with single elements with the same thermal contact area while changing their thicknesses, 1.2 mm, 3.6 mm, and 6.3 mm (**Figure 5.10**), to compare the V_{ON} values (open circuit voltages when stimulated with temperature gradients), as well as rise and fall times. We conclude that for thicker elements, the maximum V_{ON} is higher and, therefore, it needs more time to be achieved, but then it is stable for more extended periods, while the thinner ones are faster to respond, but they cannot sustain the temperature gradient for more than a few seconds.

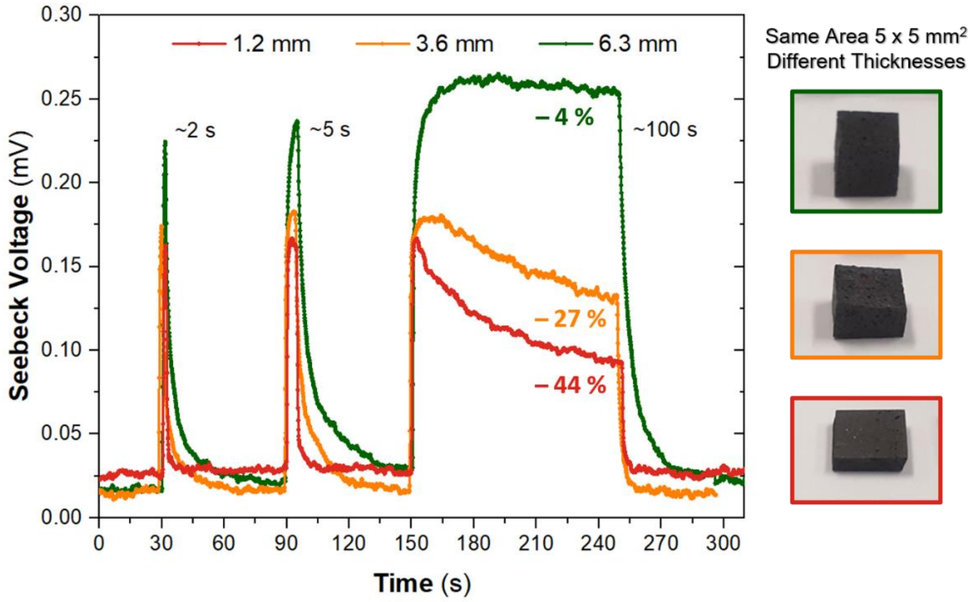

Figure 5.10 - Thermoelectric response of single elements with the same thermal contact area but different thicknesses when subjected to short and long gloved touches, evidencing the loss of signal over time for the longer touches.

5.3.2.2 Vertical TE Elements Connected in Series

Thinner samples presented faster responses to touch events, and so, for TE elements with 1.2 mm of thickness, there was an attempt to maximize the V_{ON} value for an area equivalent to the area of an index finger thermal contact, connecting TE legs electrically in series. In **Figure 5.11**, there are the results for three different TE touch detectors - the red curve is relative to a single element with a touch area of 5 x 5 mm^2, the orange curve corresponds to six TE elements connected in series, each with an area of 5 x 5 mm^2, and the green curve gives the result for fourteen connected TE elements, each with an area of 5 x 2 mm^2. Note that the test included touch events 30, 15, and 5 s apart, showing that the more elements connected and the higher the V_{ON} response, the more recovery time is required, which means that, for the faster touch repetition (5 s apart), only the single element sensor was able to return to its OFF state between touches. Thus, the signal can be increased more than 8 times, comparing the 14-element sensor with the starting point, due to the sum of each S, and can have good repeatability of peaks, notwithstanding that the recovery time needs to be longer.

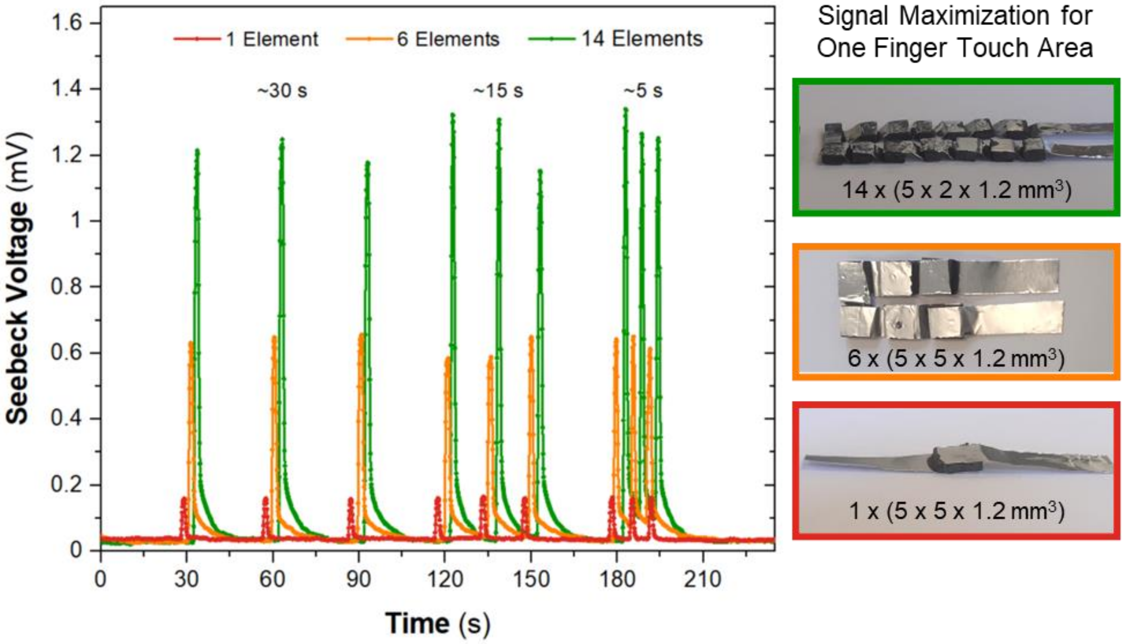

Figure 5.11 - Touch detection results for three different TE sensors (real images on the right side of the figure), separated by decreasing gap times. The red curve is relative to a single element with and area of 5x5 mm^2, to serve as comparison; the orange curve is correspondent to six elements with the previous area connected electrically in series and the green curve corresponds to a miniaturization of fourteen TE legs, with each one having a thermal contact area of 5x2 mm^2. All the TE elements had the same thickness, 1.2 mm.

To confirm that the signal output of these sensors was merely due to thermal stimulus and not, for instance, pressure or mechanical deformation, the sample with 6 elements connected electrically in series was submitted to a complementary test. The V_{OC} over time was measured while the sample was experiencing a stimulation with a hot water glass and a RT water glass (see **Appendix Figure 8**). It was observed that the sensor only responds to the hot water glass stimulation, meaning that the weight of the water glass itself did not interfere with the output response.

Since the thicker samples can maintain the V_{ON} for longer periods, **Figure 5.12** - **(a)** shows the results of gloved touches for 60 s for 1, 3, 6 and 16 electrically connected elements with 6 × 6 × 6.3 mm^3 of volume. The devices with 1, 3 and 6 connected elements could be stimulated with just one finger touch, while the sensor with 16 elements needed the thermal contact of a palm.

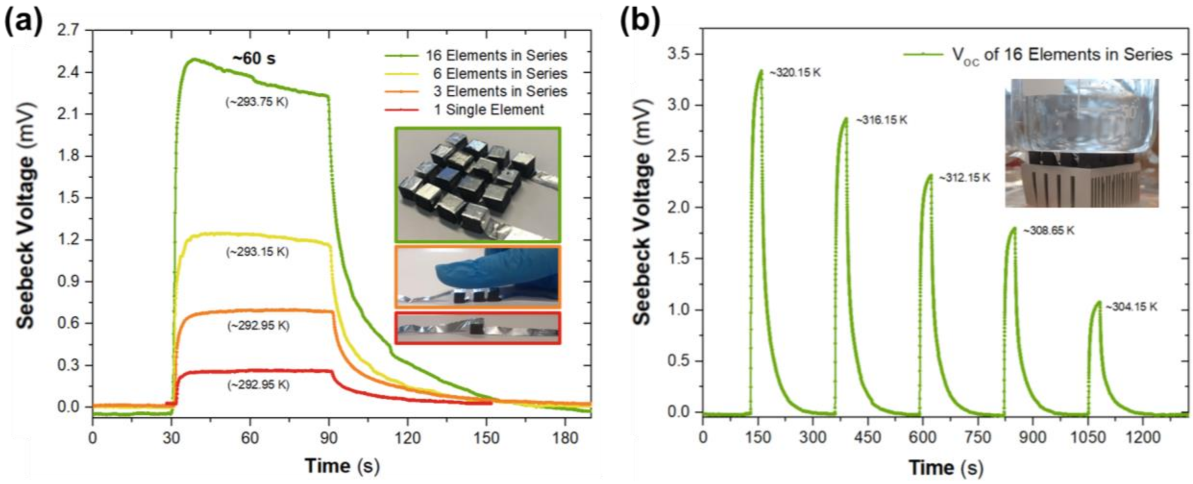

Figure 5.12 - Thermoelectric response for: **(a)** gloved touch detection tests of sensors with the same element geometries but increasing number of electrically connected in series elements (up to 16-elements) and **(b)** a hot water test with the 16-elements sensor.

As we can see, the V_{ON} response increases when more elements are electrically connected in series since the S of the device is the sum of each S. Due to its relevant thermoelectric signal, the device with 16 elements was submitted to hot water sensing, in which several water temperatures were tested, having discriminated V_{ON} values, **Figure 5.12** - **(b)**. The measured samples can be seen in the inset photographs.

5.3.2.3 Encapsulation Step

In contrast to the TE sensors produced by SP on paper and fabric substrates, the PDMS/G_{Flakes} composites do not have the problem of water absorption by their structure over time due to the characteristic hydrophobicity of the PDMS, and their performance is maintained, even after years have passed. However, although the planar single-element sensors are robust, the vertical devices with several TE legs electrically connected in series presented a low robustness once no substrate was used, and the electrical paths presented some fragility (aluminium foil). Thus, an attempt to encapsulate these TE elements using a "gap filler" approach was made using a PDMS/cork composite (see the experimental details in **section 5.3.1.3**), envisioning a flexible and lightweight device.

The initial composite samples were produced with granulated cork below 500 µm, varying their concentrations (~6 and ~11 wt%), and measuring their volumetric mass density (blue square and blue triangle in **Figure 5.13**).

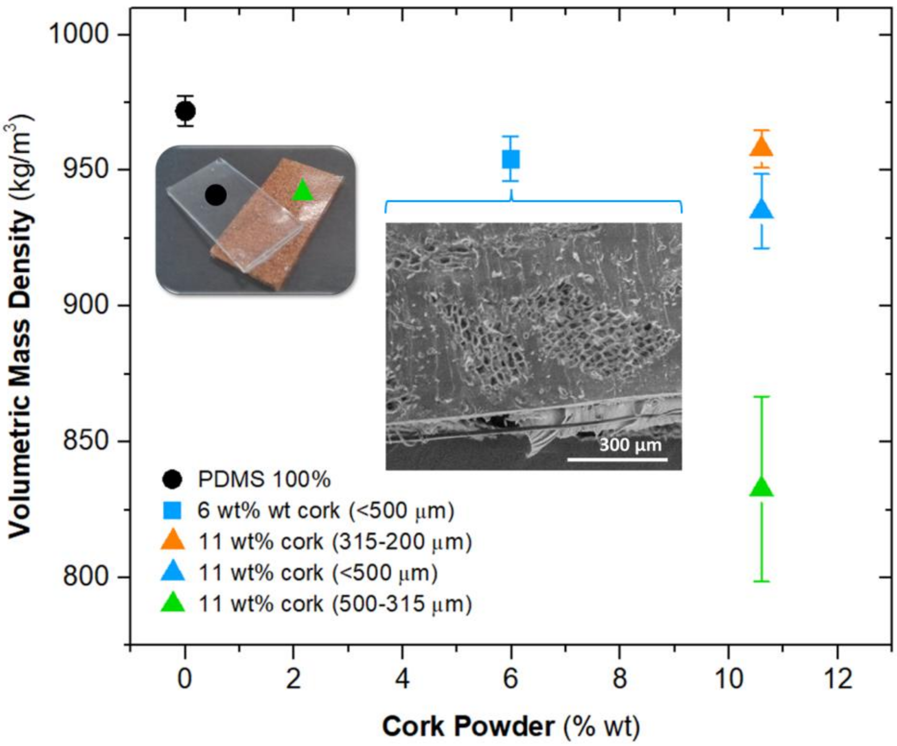

Figure 5.13 - Volumetric mass density for different PDMS/cork composites, varying the size and distribution of the cork granulates. The left inset image shows the optical differences between a sample of 100% of PDMS and a composite sample with 11 wt% of cork granules and the right inset image was acquired by SEM, emphasising the alveolar structure of cork.

It was found that this "eco" incorporation led to a 4% decrease in volumetric mass density when comparing the composite having ~11 wt% of cork filler and pure PDMS (black circle), which was less than expected. In subsequent tests, samples with different size distribution of grinded cork were produced, mixing with the PDMS the same ~11 wt% of cork between 500-315 µm and cork between 315-200 µm. Bellow 200 µm it was assumed that the cork structure would be excessively damaged (see SEM inset image).

Although with an associated variation higher than the other two granulometries, the results showed that a decrease of 14% in volumetric mass density could be achieved using the cork granulates between 500-315 µm (green triangle). Using cork with smaller dimensions between 315-200 µm does not make a relevant difference (orange triangle) in the volumetric mass density of PDMS itself. This means that the grinding and sieving process to obtain smaller grains is too destructive of the alveolar structure of the cork, responsible for its lightness.

Figure 5.14 shows the temperature variation in PDMS samples and PDMS/Cork depicted as an inset in **Figure 5.13**, as a function of the planar distance to the heat source (a Peltier element). Although this was a simple test, incorporating cork allows larger ΔT in shorter distances (see the gap between the curves plotted in **Figure 5.14**, most probably due to a lower k value). In conclusion, the cork granules addition creates a lighter material that will also have its thermal conductivity lowered, being a perfect candidate for the substitution of PDMS parts where, for instance, the high geometry definition is not a priority.

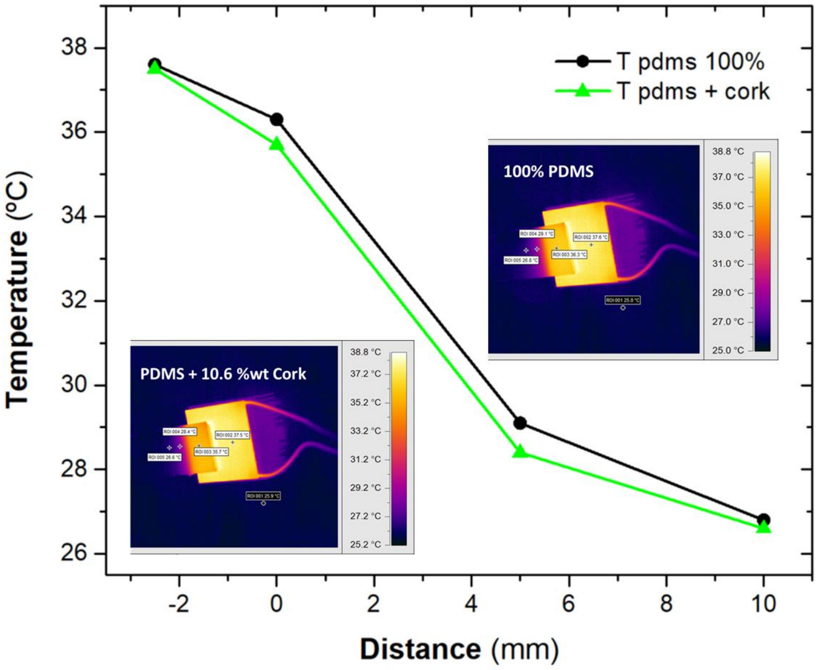

Figure 5.14 - Test comparing the temperature propagation in samples with and without the cork incorporation when heated on one side using a Peltier element as heat source.

After analysing the preliminary results, a mixture of 7.5 wt% of cork granules with dimensions between 315-500 µm was chosen to test as gap-filler. The reason behind selecting a lower cork content is that, in this case, it was difficult to fill all the holes in the sensor, and a higher amount of PDMS would facilitate the mixture to penetrate better between the TE elements and electrical connections. In **Figure 5.15**, we can see the gloved touch detection results for the 16-element encapsulated vertical sensor, corresponding to the green curves sample in **Figure 5.12**, before the encapsulation test. Both touches had a duration of 60 s, but the first V_{OC} peak corresponds to the response of all the 16 elements touched, while the second peak measured the response of a single 4-element row being touched. In addition to discerning the duration of touch events, this sensor can also differentiate between various numbers of touched elements, thereby expanding its capability to distinguish between different thermal stimuli.

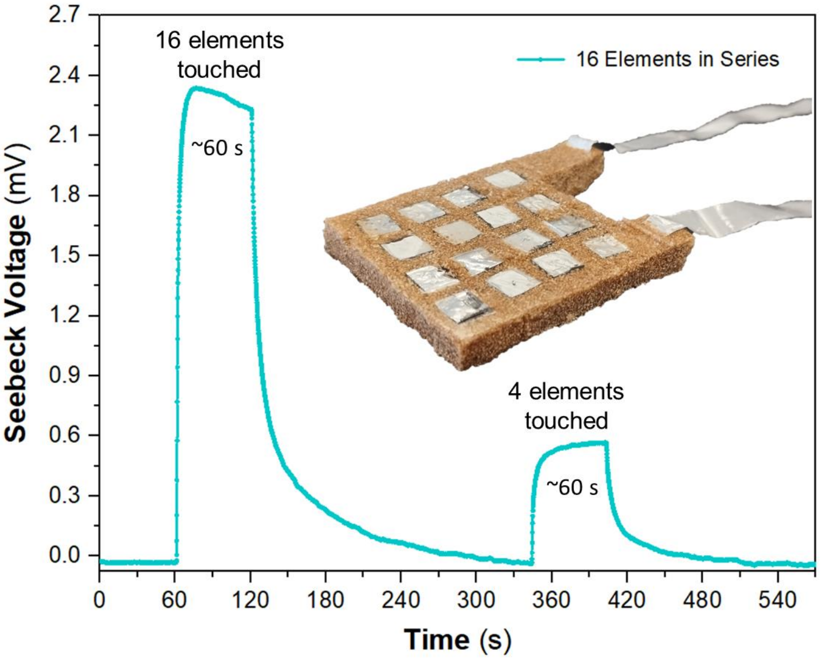

Figure 5.15 - Touch detection results for a 16-elements vertical sensor based on two distinct PDMS composites - thermoelectric elements produced with a PDMS/G_{Flakes} composite encapsulated with an insulator PDMS/Cork composite - the first peak corresponds to a palm touch reaching every element and the second peak corresponds to a finger touch reaching a whole row of 4 elements

5.3.3 Conclusions

The design, production, characterization, and optimization of planar and vertical touch detectors based on PDMS/G_{Flakes} composites were showcased. These devices offer simple and cost-effective fabrication advantages, employing low-temperature processes while achieving reliable performance. Furthermore, planar devices do not require the support of an additional substrate, and vertical architectures with multiple elements can be made more robust using a gap filler.

Various composites were studied, varying the concentration of G_{Flakes} (40, 45, and 50 wt%). All compositions exhibit major p-type electrical conductivity, with an increase in graphite concentration leading to higher carrier concentration and electrical conductivity, accompanied by a decrease in the Seebeck coefficient value. The optimum concentration was found to be 45 wt% G_{Flakes}, striking a balance between electrical conductivity and processability.

Single-element planar sensors with 45 wt% G_{Flakes} yield robust and homogeneous detectors with SNR values of up to 170 and rise and fall times below 1 s and 7 s, respectively. These composites were evaluated for 'Yes' or 'No' applications in both flat and bent configurations, demonstrating their suitability for flexible applications. Regarding vertical architectures, the number of connected elements was varied up to 16 using C_{ink} and aluminium foil for interconnections, achieving a maximum response of

>2.4 mV for touch detection. These sensors were encapsulated with a PDMS/cork composite to enhance robustness while maintaining flexibility, biocompatibility, low weight, and thermal conduction.

All the detectors function effectively, with short response times, returning to the initial V_{OFF} values (open circuit voltages when no temperature gradient is applied), enabling repeated thermal stimuli. The V_{ON} results reach 10^{-4} to 10^{-3} V even for the fastest touches and small temperature gradients, making these devices suitable for various IoT applications. Furthermore, capacitive touch sensors require a conductive object to operate, eliminating many other touch objects, such as gloved fingers.

6

FINAL CONSIDERATIONS AND FUTURE PERSPECTIVES

6.1 Main Conclusions

The pursuit of production methods that sidestep the need for high temperatures or vacuum conditions has gained remarkable importance in reducing environmental impact and conserving energy [175], [225]. Within this context, the domain of printed and flexible electronics has emerged, and the development of electronic circuits and devices onto flexible substrates is achieved through innovative printing techniques. The advantages of printed and flexible electronics include their lightweight design, low manufacturing costs, and seamless compatibility with non-standard surfaces and shapes [226]. On the other hand, some sustainable thermoelectric materials have very interesting properties to be used in green energy generation or sensing applications, and printing offers a potential route to manufacture TE devices at a lower price point and allows a custom-built approach to meet the waste heat source requirements [5]. This PhD work explored eco-materials for touch detection and temperature sensing flexible applications using printing techniques and low-temperature processes. In **Figure 6.1**, the keywords of this PhD work are represented.

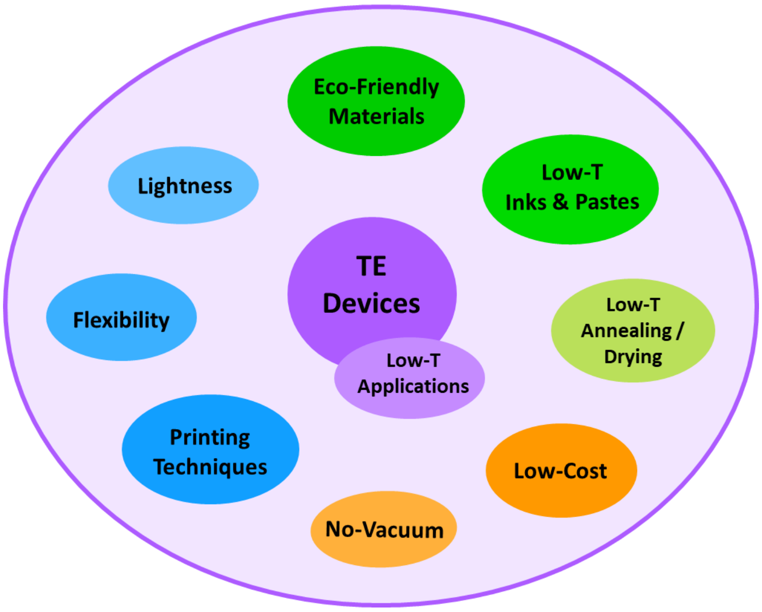

Figure 6.1 - Schematic of the PhD workplan addressed topics.

6.1.1 Screen-Printable TE sensors with inks based on EC/G$_{\mathrm{Flakes}}$

The G/EC formulated inks are suitable for screen-printing, using distinct types of paper or cotton, originating lightweight and flexible TE sensors through a simple and low-cost fabrication. It was possible to achieve sensors with fast response times (bellow 1 s) and to have a V_{ON} optimization surpassing 4.5 mV (when connecting multiple elements in series) and high SNR values (> 300), **Figure 6.2**. The printed elements were tested and approved for flexible applications, with curvature radii down to 3 mm. These are promising results regarding eco-friendliness, flexibility, availability, and simplicity. Also, with screen-printing and low-T (without the need for vacuum systems), we can consider this technology as potentially portable.

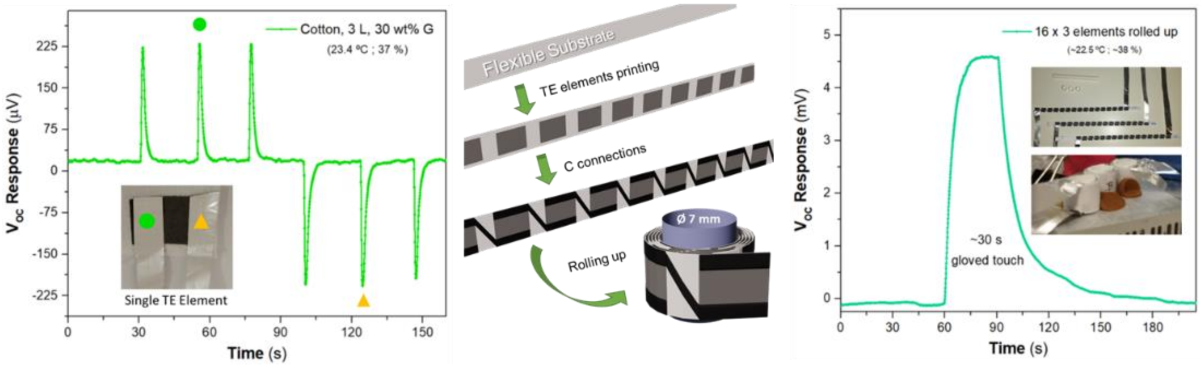

Figure 6.2 - Graphical table of contents for the EC/G$_{Flakes}$ screen-printable inks study, demonstrating a sensor with fast responses and other with high SNR.

The TE sensors printed on paper and cotton substrates were encapsulated with EC, PVA, and laminated plastic. All three materials exhibited good thermal stability for T up to 150 °C, i.e., they are compatible with the studied application but can also be used with other flexible substrates. CA measurements revealed that, while laminated plastic provides inherent water impermeability independently of the substrate, EC and PVA encapsulation radically transformed the wettability of non-encapsulated paper and cotton, enhancing their waterproof ability, see **Figure 6.3**. Additionally, after submersion in water, EC and PVA-encapsulated substrates displayed higher CA values than laminated plastic, indicating higher hydrophobicity.

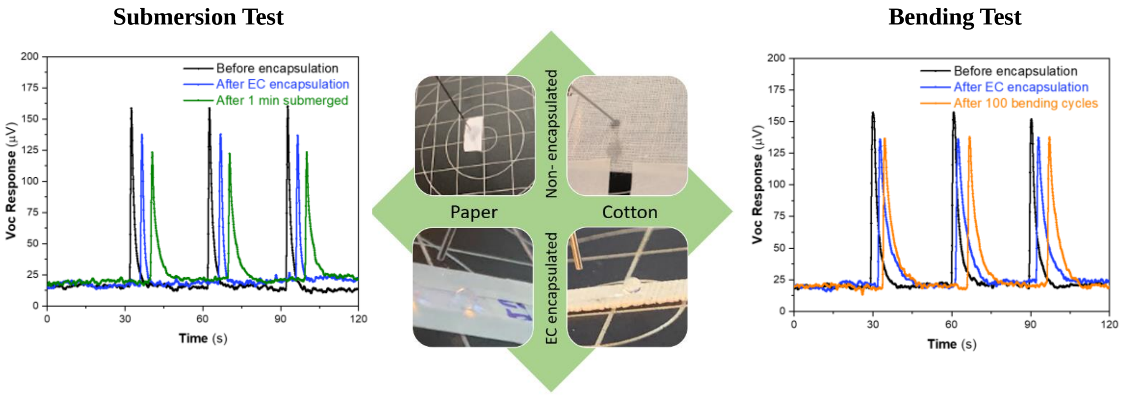

Figure 6.3 - Graphical table of contents for the encapsulation studies performed for the screen-printed planar TE sensors.

Regardless of the encapsulation approach, there was a predictable loss in V_{OC} and longer recovery times after the encapsulation step due to the additional thermal resistance introduced by the encapsulation layer. However, all three encapsulants enabled proper touch detection, maintaining relevant response signals (~100 µV) and rapid rise times (below 1 s). The EC was defined as the preferred encapsulant material due to its eco-friendliness and minimal interference with electrical response.

Moreover, its single-blade coating deposition step on both substrates offered a favourable feature for large-scale manufacturing.

6.1.2 PDMS/G$_{\text{Flakes}}$ TE Sensors

This work reported the production of TE composites based on PDMS/G$_{\text{Flakes}}$ for touch detection and temperature sensing for the first time. This PDMS/G$_{\text{Flakes}}$ composite is suitable for film casting and blade coating techniques, allowing great freedom of geometries (area and thickness) and architectures (planar and vertical), as seen in **Figure 6.4**. The fabrication process is simple and low-cost, and the sensors were tested and approved for flexible applications.

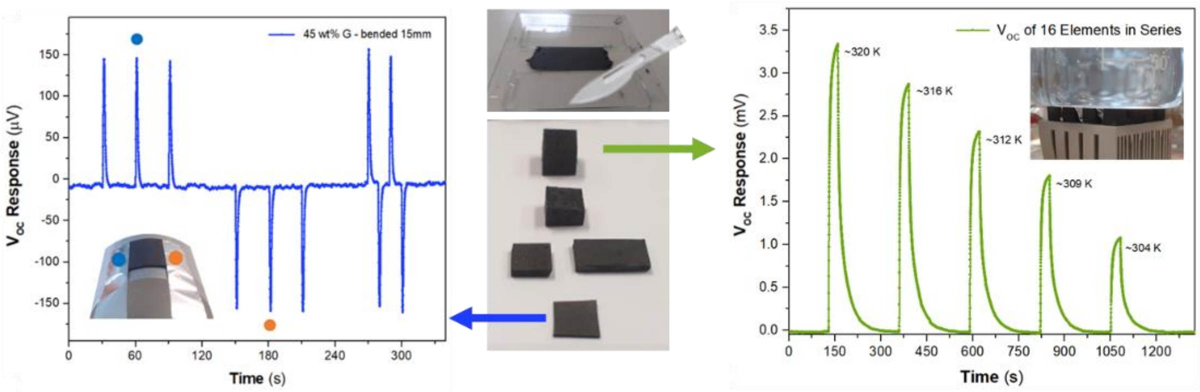

Figure 6.4 - Graphical table of contents for the PDMS/G$_{\text{Flakes}}$ composites study, highlighting the proof-of-concepts for different geometries.

The planar TE sensors showed relevant and reproducible performances, not needing any extra substrate. An optimal concentration of G$_{\text{Flakes}}$ (45 wt%) led to robust and homogeneous detectors that exhibited SNR values up to 170 with rise and falling times below 1 s and 7 s, respectively. The proof-of-concept evaluated an optimized sensor for a binary (Yes or No) application in its flat and bent configurations. The results revealed short rise and fall times, with relevant SNR values, which is highly promising for fast real-time human touch applications.

As for the vertical TE sensors, V_{ON} responses reaching 10^{-3} V were achieved when connecting multiple elements in series, which allowed a considerable discrimination of V_{OC} values for different temperature stimuli. A 16-element vertical TE sensor was encapsulated with a composite based on PDMS and cork granules, making it possible to conclude that the device remains functional and flexible.

6.2 Upcoming Possibilities

6.2.1 New Eco-friendly Materials

As mentioned throughout this thesis, sustainable choices are increasingly important, and it is crucial to research environmentally friendly materials and production techniques that allow low energy consumption. In exploratory work, molybdenum disulfide nanostructures were grown directly on cork substrates (from used wine bottle corks) via microwave-assisted hydrothermal synthesis, following the procedure described in published works reporting the MoS_2 nanostructures growth on paper substrates [127], [227].

The most used synthesis methods of the two-dimensional MoS_2 are exfoliation (liquid and mechanical), chemical vapor deposition (CVD), and hydrothermal. Due to a better relationship between uniformity, the quantity of produced material and production cost, the hydrothermal method has been the most applied in synthesising MoS_2 nanostructures, usually presenting synthesis times between 20 and 24 h. The microwave-assisted hydrothermal approach allows shorter synthesis times and lower energy consumption than the conventional hydrothermal method due to “molecular heating”, consequently lower energy consumption, enhanced reaction selectivity, and homogeneous volumetric heating [127]. This method also allows the direct growth of the material on a substrate, being an alternative to conventional deposition or costly transfer methods. Using a synthesis substrate, cork wastes, in this case, promotes a better synthesis efficiency and can be seen as a step for the circular economy concept, **Figure 6.5**.

Figure 6.5 - Giving cork a second life: Use wine bottle stoppers wastes as a raw material for a new application.

Figure 6.6 shows a schematic of the process to reach the MoS_2/cork composite thermoelectric disc, including the MoS_2 precursors, synthesis parameters and products, and the creation of the electrode (with aluminium foil and C_{ink}). Two different synthesis substrates were tested: cork splinters, simply cut from the wine corks, and cork granules, obtained as described in **section 5.3.1.3**, **Figure 5.8**. After synthesis, the material was slightly ground in the case of splinters and cold pressed to obtain a robust disc that was characterised as a thermoelectric touch sensor.

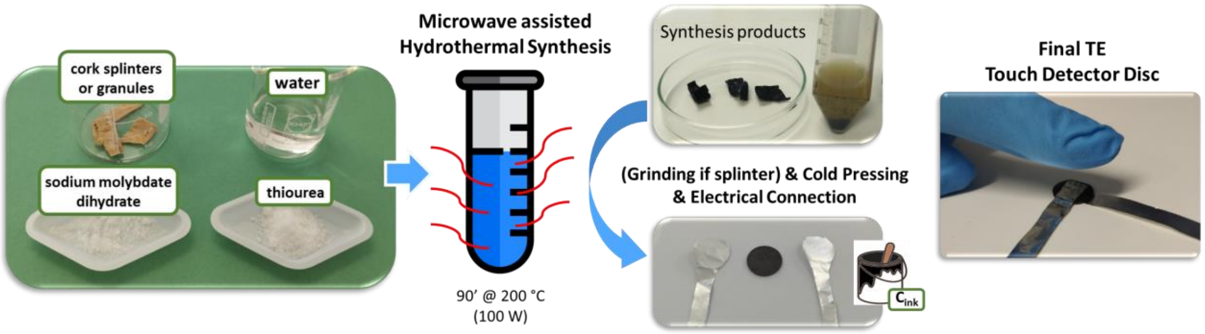

Figure 6.6 - Schematic of the production process to obtain the MoS_2/cork thermoelectric discs through microwave assisted hydrothermal synthesis and cold pressing.

In **Figure 6.7**, there are some SEM images of the used cork granules as synthesis substrates and of the MoS_2 synthesis results without any substrate and using cork as substrate (acquired with a Hitachi Regulus SU8220, with a pre-deposited iridium layer of 20 nm). The identical MoS_2 nanostructures that grow without a substrate, **Figure 6.7** - **(b)**, are the same that grow around the cork substrate, **Figure 6.7** - **(c)**.

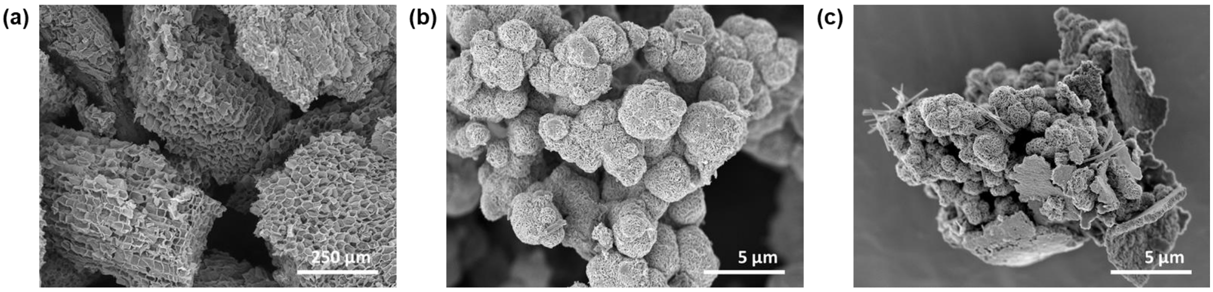

Figure 6.7 - SEM images for: **(a)** cork granules after wine corks grinding, **(b)** MoS_2 obtained without any substrate and **(c)** MoS_2 obtained with cork as substrate through microwave assisted hydrothermal synthesis.

An X-ray diffraction (XRD) analysis was performed on the samples, with the resultant patterns presented in **Figure 6.8**. Compared to bulk 2H MoS_2 (JCPDS card nr 37-1492), there is no match to the (002) plane positioned at 14.4°, the most intense peak. However, it is possible to identify the appearance of two new peaks, one at 9° and 9.2° for both synthesis and another at 18.4° for the cork substrate synthesis. These two peaks have been usually assigned to the intercalation of molecules and ions between the MoS_2 layers [228], [229]. The cork substrate before synthesis showed a broad peak centered at around $2\theta = 21°$, as reported in the literature [230]. This peak disappears in the diffractogram after synthesis.

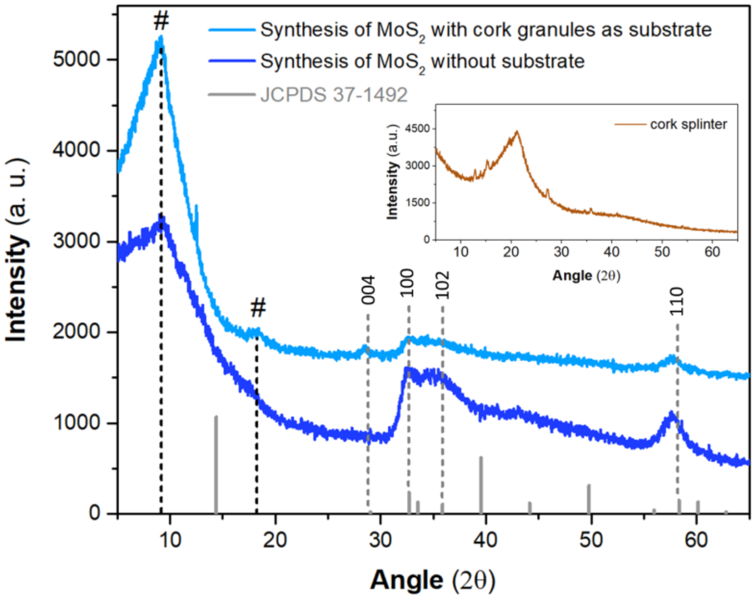

Figure 6.8 - XRD analysis for samples of natural cork (brown), MoS₂ synthesised without any substrate (dark blue) and MoS₂ synthesised with cork as substrate (light blue).

The composite discs were characterised using a potentiostat (**section 3.2.1**), measuring the open circuit potential over time. The thermoelectric samples were submitted to gloved finger touch events, and the electrical response was recorded, **Figure 6.9**.

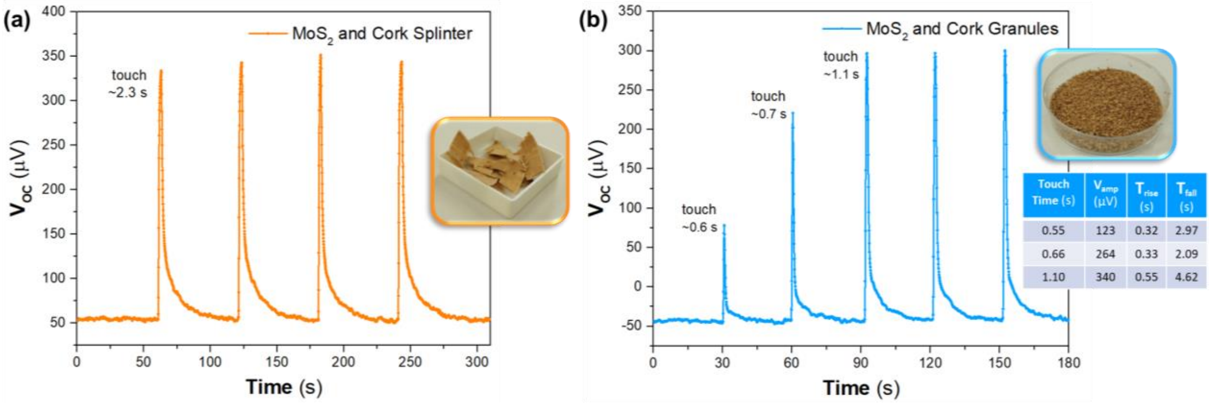

Touch Time (s)	V_{amp} (μV)	T_{rise} (s)	T_{fall} (s)
0.55	123	0.32	2.97
0.66	264	0.33	2.09
1.10	340	0.55	4.62

Figure 6.9 - Open circuit potential results for finger touch events. **(a)** Composite sample produced with cork splinters (inset image) during microwave synthesis, stimulated with similar touch times and **(b)** composite sample produced using cork granules (inset image) during the microwave synthesis, stimulated with different touch times.

In **Figure 6.9** - **(a)**, a good repeatability of results can be observed for the same touch time, with the composite showing signal-to-noise values of 277 ± 6 and rise and fall response times of 1.1 ± 0.2 and 11.3 ± 1.2 s, respectively. In another test, **Figure 6.9** - **(b)**, the thermoelectric disc was touched during different periods. The longer the thermal contact, the higher the response amplitude and the slowest the response times, as seen in the inset table. The positive peaks revealed a p-type material; however, further tests need to be conducted to understand this electrical behaviour since no intentional doping or surface modifications were induced, and MoS_2 is commonly reported as a n-type semiconductor [231], [232].

Due to the simplicity of the process and the possibility of grinding the composite after synthesis or even introducing already ground cork on the microwave system, these results pave the way for formulating printable thermoelectric inks and achieving planar architectures. An upcoming possibility could be introducing smaller granules in the microwave synthesis container to achieve composite geometries compatible with screen-printing meshes.

6.2.2 Optimization of the Devices Architecture

Since the TE response increases with the connection of multiple TE elements in series (for the same T stimulus), a significant improvement would be the miniaturization of each TE leg. This way, it would be possible to increase the number of connected elements per area and volume, or at least have the same number of interconnected elements with less material expenditure.

Since the covered applications depend on small T gradients and fast periods of response, it would be possible to miniaturize the TE legs without interfering with the performance of the sensor (if the ΔT are high, one of two things need to happen, or both: the existence of a powerful cooling system/heat radiator, and a geometry big enough to sustain a temperature difference between sides).

This desired miniaturization requires new stencil designs for the screen-printed sensors and casting moulds, or different cutting methods, for the PDMS composites.

The next step to pursue, changing the used materials, would be the electrical connections between TE elements. As explained in **section 4.3.2.1**, connecting TE elements in series with the same electrical conduction (p-type in this case), without the standard p-n pair structure, decreases the performance of the devices. Using carbon inks as conductive paths between elements, although it fulfils the purpose of moving the electrons from top-to-tail, always ends up being counterproductive because the carbon ink itself has a very small but also p-type Seebeck coefficient. Using silver or copper inks would allow more conductive paths, but the S issue would be the same, or even worse since they present higher p-type values. The solution would pass by using an n-type conductive ink, such as nickel, but besides the complexity of producing it, oxidation problems have been reported [136].

Regarding the use of C_{ink}, future work could test newer and eco-friendly commercially available products, mainly regarding the cleaning solvent needed to clean the meshes after the printing process.

6.2.3 Improvement of the Characterization Setup

The optimization of the characterization setup is a relevant aspect to consider. The electrical connections between the sensors and the potentiostat terminals are critical in acquiring the V_{OC} vs time results. A future perspective could be to improve those connections, creating a more stable support for the samples assembling during measurements.

Another essential feature to add would be a temperature gradient reading system. An attempt was made to envision this measurement, recurring to an Arduino setup with two PT100 sensors, but it was difficult to position the thermometers in the desired place, and due to lack of time, the experiments were halfway through.

Although the applications for the studied materials relied on temperature sensing and touch detection, it would be essential to measure the maximum output power for a specific thermal gradient to check the TE potential for other applications. For this to happen, there must be a system able to apply an electrical load, varying it between short circuit (<< optimum resistance (R_{opt})) and open circuit (>> R_{opt}), including its optimum resistance in the middle (the useful power reaches its maximum value when the load resistance is equal to the generator resistance [6]).

6.2.4 Optimization of the Encapsulation Step

Future research should focus on optimizing the encapsulating processes and investigating alternate deposition techniques that can also be suitable for large-area manufacturing and/or geometrical complex surfaces, such as spray coating. Regarding the screen-printed sensors, although the encapsulation method tested was successful, it is true that the used samples were planar single-element sensors, which facilitated the process. As for the vertical composite sample encapsulation, it was difficult to pour the encapsulation mixture between the TE cubes without damaging the electrical connections and misplacing the TE legs.

6.2.5 Sustainability Considerations

An evaluation should be carried out to evaluate the sustainability of the proposed TE devices and to estimate the requirements for successful technology development in the future. This tool is used to pinpoint procedures/materials that are simply too energetically demanding to be considered suitable for the technology.

In this PhD work, choices were made considering low-energy consumption, for instance, the use of printing techniques, the drying steps at RT instead of applying temperature to speed up the process, and the absence of annealing stages. Also, using a cellulose derivative for the ink's formulations and substituting toluene for diacetone alcohol as a solvent were advancing towards more sustainable products. Incorporating cork in a PDMS matrix as an encapsulant is another possible approach to decrease the use of avoiding materials and give a second life to natural raw material. Finally, the proposed in **section 6.2.1** is a work that offers an alternative second life to cork wastes, using a technique that also falls into the more sustainable production processes category.

7

OUTPUTS

As a parallel task to the laboratory work, it is essential to disseminate the results achieved in the PhD project to the scientific community for peer validation and scientific outreach. This task has been accomplished through scientific publications developed in collaborative research and posters or oral presentations at scientific conferences. Below is a summary of all major outputs generated during work activities for this PhD thesis. Some other relevant courses and projects are also listed.

Scientific publications

Resulting from the PhD work

- Figueira, J.; Bonito, R. M.; Carvalho, J. T.; Vieira, E. M. F.; Gaspar, C.; Loureiro, J.; Correia, J. H.; Fortunato, E.; Martins, R.; Pereira, L. *Screen-printed, flexible, and eco-friendly thermoelectric touch sensors based on ethyl cellulose and graphite flakes inks*. Flexible and Printed Electronics **2023**, 8 (2). https://doi.org/10.1088/2058-8585/acc114.

- Figueira, J.; Vieira, E. M. F.; Loureiro, J.; Correia, J. H.; Fortunato, E.; Martins, R.; Pereira, L. *Composites Based on PDMS and Graphite Flakes for Thermoelectric Sensing Applications*. Materials Proceedings **2022**, 8 (1), 42. https://doi.org/10.3390/materproc2022008042.

- Figueira, J.; Loureiro, J.; Vieira, E. M. F.; Martins, R.; Pereira, L. *Flexible, scalable, and efficient thermoelectric touch detector based on PDMS and graphite flakes.* Flexible and Printed Electronics **2021**, 6 (4). https://doi.org/10.1088/2058-8585/ac45de.

- Figueira, J.; Gaspar, C.; Carvalho, J. T.; Loureiro, J.; Fortunato, E.; Martins, R.; Pereira, L. *Sustainable Fully Printed UV Sensors on Cork Using Zinc Oxide/Ethylcellulose Inks*. Micromachines **2019**, 10 (9), 601. https://doi.org/10.3390/mi10090601.

Submitted

- Figueira, J.; Peixoto, M.; Gaspar, C.; Loureiro, J.; Martins, R.; Carlos, E.; Pereira, L. *Flexible cellulose-based encapsulation for printed thermoelectric sensors*, IEEE Sensors **2023**. (two first authors)

Other publications during the PhD work

- Vieira, E. M. F.; Figueira, J.; Pires, A. L.; Grilo, J.; Silva, M. F.; Pereira, A. M.; Gonçalves, L. M. *Bi_2Te_3 and Sb_2Te_3 Thin Films with Enhanced Thermoelectric Properties for Flexible Thermal Sensors*, Proceedings of Eurosensors **2018**, 2, 815. https://doi.org/10.3390/proceedings2130815.

- Vieira, E. M. F.; Figueira, J.; Pires, A. L.; Grilo, J.; Silva, M. F.; Pereira, A. M.; Gonçalves, L. M. *Enhanced Thermoelectric Properties of Sb_2Te_3 and Bi_2Te_3 Films for Flexible Thermal Sensors*. Journal of Alloys and Compounds **2018**, 774, 1102-1116. https://doi.org/10.1016/j.jallcom.2018.09.324.

- Loureiro, J.; Mateus, T.; Filonovich, S.; Ferreira, M.; Figueira, J.; Rodrigues, A.; Donovan, B. F.; Hopkins, P. E.; Ferreira, I. *Improved thermoelectric properties of nanocrystalline hydrogenated silicon thin films by post-deposition thermal annealing*, Thin Solid Films **2017**, 642, 276-280. http://dx.doi.org/10.1016/j.tsf.2017.09.047.

Submitted

- Pereira, A.; Marques, M. A.; Alves, J.; Morais, M.; Figueira, J.; Pinto, J. V.; Moreira, F. T. C. *Irreversible colourimetric bio-based curcumin bilayer membrane for smart food packaging temperature control applications*, Food Packaging and Shelf Life **2023**.

In preparation

- Figueira, J.; Morais, M.; Carlos, E.; Peixoto, M.; Corvo, M. C.; Marques, C.; Gonçalves, A.; Martins, R.; Pinto, J. V. *Flexographic-printed hybrid thermochromic stickers for smart sensing applications*. (two first authors)

Scientific conferences

Oral presentations

- Figueira, J.; Morais, M.; Carlos, E.; Corvo, M. C.; Marques, C.; Gonçalves, A.; Martins, R.; Pinto, J. V. *Flexography-printed thermochromic stickers based on nickel complexes and cellulose derivatives Inks for smart sensing*, **MATERIAIS 2023 - Guimarães, Portugal** (3rd to 6th April 2023). (two first authors)

- Figueira, J.; Vieira, E. M. F.; Loureiro, J.; Correia, J. H.; Fortunato, E.; Martins, R.; Pereira, L. *Composites based on PDMS and Graphite Flakes for Thermoelectric Sensing Applications*, **MATERIAIS 2022 - Marinha Grande, Portugal** (10th to 13th April 2022).

Poster presentations

- Figueira, J.; Carvalho, J. T.; Loureiro, J.; Martins, R.; Pereira, L. *Cork and MoS_2 Composite – A Novel Green Material Suitable for Thermoelectric Sensing Applications*, **MATERIAIS 2023 - Guimarães, Portugal** (3rd to 6th April 2023).

- Morais, M.; Figueira, J.; Carlos, E.; Corvo, M. C.; Marques, C.; Gonçalves, A.; Martins, R.; Pinto, J. V. *Flexographic printed thermochromic stickers with visible colour transition for smart sensing applications*, **VIII Annual Meeting i3N** – Leiria, Portugal (3rd to 4th March 2023). (two first authors)

- Figueira, J.; Bonito, R. M.; Carvalho, J. T.; Vieira, E. M. F.; Gaspar, C.; Loureiro, J.; Correia, J. H.; Fortunato, E.; Martins, R.; Pereira, L. *Optimization of Flexible and Eco-friendly Thermoelectric Touch Detectors based on Ethyl Cellulose & Graphite Flakes Inks for Screen-Printing,* **Junior EUROMAT 2022 - Coimbra, Portugal** (19th to 22nd June 2022).

- Figueira, J.; Vieira, E. M. F.; Loureiro, J.; Correia, J. H.; Fortunato, E.; Martins, R.; Pereira, L. *Composites based on PDMS and Graphite Flakes for Thermoelectric Touch Detectors Applications,* **Junior EUROMAT 2022 - Coimbra, Portugal** (19th to 22nd June 2022).

- Figueira, J.; *Printed Eco-Materials for Flexible Thermoelectric Devices*, **Encontro Ciência '20 – Online event, Portugal** (3rd to 4th November 2020).

- Figueira, J.; *Flexible Thermoelectric Generator for Smart Wristwear Devices*, **Encontro Ciência '19 – Lisboa, Portugal** (8th to 10th July 2019).

- Figueira, J.; Gaspar, C.; Carvalho, J. T.; Loureiro, J.; Fortunato, E.; Martins, R.; Pereira, L. *Cork - A Novel Green Substrate Suitable for All-Printed Wearable Technology*, **MATERIAIS 2019 - Lisboa, Portugal** (14th to 17th April 2019).

- Vieira, E. M. F.; Figueira, J.; Pires, A. L.; Grilo, J.; Silva, M. F.; Pereira, A. M.; Gonçalves, L. M. *Bi_2Te_3 and Sb_2Te_3 thin films with enhanced thermoelectric properties for flexible thermal sensors*, **Eurosensors 2018 - Graz, Austria** (9th to 12th September 2018).

Regular attendance (without poster or oral presentation)

- *Encontro Ciência 2022* – Lisbon, Portugal (16th to 18th May 2022).
- "O Ciclo da Vida do Papel", Conferência da Ordem dos Engenheiros, Lisboa, Portugal (13rd November 2019).

Seminars presented by the author of this thesis

- Figueira, J.; *Printed and Flexible Thermoelectric Sensors with Graphite Flakes*, 11th European School for Young Materials Scientists, **2022**.

Academic awards

- Morais, M.; Figueira, J.; Carlos, E.; Corvo, M. C.; Marques, C.; Gonçalves, A.; Martins, R.; Pinto, J. V. - Best Poster Award at the VIII Annual Meeting i3N, Leiria, Portugal (3rd to 4th March 2023).
- Coelho, B. J.; Gaspar, C.; Figueira, J. "Droplet Runners: Digital Microfluidics for point-of-need nutrient assessment." Most Innovative Project at the PrintoCent Innofest – Oulu, Finland (7th and 8th June 2018).

Courses and Projects

- TCM-NET School on Materials for Flexible Electronics, Smart Surfaces and Sensing – Lisbon, Portugal (14th April 2019).
- Internship at Bay Campus, Swansea University, Wales. (January-May 2019).
- PrintoCent Innofest – Oulu, Ideas Competition, Finland (7th and 8th June 2018).
- Research Skills Development course from NOVA Doctoral School – Setúbal, Portugal (20th to 23rd April 2018).
- "Energia e Sustentabilidade Ambiental" (ESA), Bioenergy Doctoral Program, Caparica, Portugal (March to July 2018).
- International Physics Olympiad (IPhO 2018), Lisbon, Portugal

- Design Thinking course from NOVA Doctoral School – Lisbon, Portugal (2nd to 3rd November 2017).
- ERASMUS-ELBYSIER Intensive Program in Graphene technologies & Nanoelectronics, FCT-UNL, CENIMAT, Portugal (9th to 13th October 2017).

BIBLIOGRAPHY

[1] J. J. Urban, A. K. Menon, Z. Tian, A. Jain, and K. Hippalgaonkar, “New horizons in thermoelectric materials: Correlated electrons, organic transport, machine learning, and more,” *J. Appl. Phys.*, vol. 125, no. 18, 2019.

[2] M. Wagner, “Simulation of Thermoelectric Devices,” Vienna University of Technology, 2007.

[3] M. Lundstrom, “Thermoelectric Effects - Physical Approach,” 2011. [Online]. Available: https://nanohub.org/resources/11747/watch?resid=12231. [Accessed: 20-Sep-2023].

[4] H. J. Goldsmid, “The Thermoelectric and Related Effects,” in *Introduction to Thermoelectricity*, Springer-Verlag Berlin Heidelberg, 2010, pp. 1–6.

[5] M. Burton, G. Howells, J. Atoyo, and M. Carnie, “Printed Thermoelectrics,” *Adv. Mater.*, vol. 34, no. 18, 2022.

[6] H. J. Goldsmid, *Introduction to Thermoelectricity*, 2nd ed., vol. 121. Berlin, Heidelberg: Springer Berlin Heidelberg, 2016.

[7] C. Wood, “Materials for thermoelectric energy conversion,” *Reports Prog. Phys.*, vol. 51, no. 4, pp. 459–539, 1988.

[8] M. Wolf, R. Hinterding, and A. Feldhoff, “High power factor vs. high zT-A review of thermoelectric materials for high-temperature application,” *Entropy*, vol. 21, no. 11, 2019.

[9] L. M. Cowen, J. Atoyo, M. J. Carnie, D. Baran, and B. C. Schroeder, “Review—Organic Materials for Thermoelectric Energy Generation,” *ECS J. Solid State Sci. Technol.*, vol. 6, no. 3, pp. N3080–N3088, 2017.

[10] Q. Wei, M. Mukaida, K. Kirihara, Y. Naitoh, and T. Ishida, “Polymer thermoelectric modules screen-printed on paper,” *RSC Adv.*, vol. 4, no. 54, pp. 28802–28806, 2014.

[11] C. Han, Z. Li, and S. Dou, “Recent progress in thermoelectric materials,” *Chinese Sci. Bull.*, vol. 59, no. 18, pp. 2073–2091, 2014.

[12] S. LeBlanc, “Thermoelectric generators: Linking material properties and systems engineering for waste heat recovery applications,” *Sustain. Mater. Technol.*, vol. 1, pp. 26–35, 2014.

[13] T. M. Tritt and M. A. Subramanian, “Thermoelectric Materials, Phenomena, and Applications: A Bird’s Eye View,” *MRS Bull.*, vol. 31, no. May, pp. 188–198, 2006.

[14] X. Liu and Z. Wang, “Printable thermoelectric materials and applications,” *Front. Mater.*, vol. 6, no. April, pp. 1–5, 2019.

[15] M. Rull-Bravo, A. Moure, J. F. Fernández, and M. Martín-González, “Skutterudites as thermoelectric materials: Revisited,” *RSC Adv.*, vol. 5, no. 52, pp. 41653–41667, 2015.

[16] Y. Zhang and S. J. Park, “Flexible organic thermoelectric materials and devices for wearable green energy harvesting,” *Polymers (Basel).*, vol. 11, no. 5, 2019.

[17] M. Orrill and S. LeBlanc, “Printed thermoelectric materials and devices: Fabrication techniques, advantages, and challenges,” *J. Appl. Polym. Sci.*, vol. 134, no. 3, 2017.

[18] C. S. Kim *et al.*, “Structural design of a flexible thermoelectric power generator for wearable applications,” *Appl. Energy*, vol. 214, no. August 2017, pp. 131–138, 2018.

[19] W. Glatz, E. Schwyter, L. Durrer, and C. Hierold, “Bi2Te3-based flexible micro thermoelectric generator with optimized design,” *J. Microelectromechanical Syst.*, vol. 18, no. 3, pp. 763–772, 2009.

[20] Y. Yao *et al.*, “High Thermoelectric Figure of Merit Achieved in Cu2S1- xTex Alloys Synthesized by Mechanical Alloying and Spark Plasma Sintering,” *ACS Appl. Mater. Interfaces*, vol. 10, no. 38, pp. 32201–32211, 2018.

[21] and M. Z. Heng Wang, Jing-Feng Li, Ce-Wen Nan, “High-performance Ag0.8Pb18+xSbTe20 thermoelectric bulk materials fabricated by mechanical alloying and spark plasma sintering,” *Appl. Phys. Lett.*, vol. 88, no. 9, 2006.

[22] M. K. Kim and M. S. Kim, “Wearable thermoelectric generator for human clothing applications,” 2013, no. June, pp. 1376–1379.

[23] A. R. M. Siddique, R. Rabari, S. Mahmud, and B. Van Heyst, “Thermal energy harvesting from the human body using flexible thermoelectric generator (FTEG) fabricated by a dispenser

printing technique," *Energy*, vol. 115, pp. 1081–1091, 2016.

[24] L. Francioso, C. De Pascali, V. Sglavo, A. Grazioli, M. Masieri, and P. Siciliano, "Modelling, fabrication and experimental testing of an heat sink free wearable thermoelectric generator," *Energy Convers. Manag.*, vol. 145, pp. 204–213, 2017.

[25] K. Suemori, S. Hoshino, and T. Kamata, "Flexible and lightweight thermoelectric generators composed of carbon nanotube-polystyrene composites printed on film substrate," *Appl. Phys. Lett.*, vol. 103, no. 15, 2013.

[26] M. R. Burton *et al.*, "3D Printed SnSe Thermoelectric Generators with High Figure of Merit," *Adv. Energy Mater.*, vol. 9, no. 26, 2019.

[27] L. Tzounis, M. Petousis, S. Grammatikos, and N. Vidakis, "3D Printed Thermoelectric Polyurethane/Multiwaled Carbon Nanotube Nanocomposites : A Novel Approach towards the Fabrication of Flexible and Stretchable Organic Thermoelectrics," *Materials (Basel).*, vol. 13, no. 2879, 2020.

[28] F. Kim *et al.*, "3D printing of shape-conformable thermoelectric materials using all-inorganic Bi2Te3-based inks," *Nat. Energy*, vol. 3, no. 4, pp. 301–309, 2018.

[29] R. A. Dorey, "Integrated Powder-Based Thick Films for Energy Harvesting Devices," *IEEE Sens. J.*, vol. 14, no. 7, pp. 2177–2184, 2014.

[30] J. Loureiro *et al.*, "Transparent aluminium zinc oxide thin films with enhanced thermoelectric properties," *J. Mater. Chem. A*, vol. 2, no. 18, pp. 6649–6655, 2014.

[31] J. Loureiro *et al.*, "Hydrogenated nanocrystalline silicon thin films with promising thermoelectric properties," *Appl. Phys. A Mater. Sci. Process.*, vol. 120, no. 4, pp. 1497–1502, 2015.

[32] J. Figueira *et al.*, "Optimization of Cuprous Oxides Thin Films to be used as Thermoelectric Touch Detectors," *ACS Appl. Mater. Interfaces*, vol. 9, no. 7, pp. 6520–6529, 2017.

[33] Z. Cao, E. Koukharenko, M. J. Tudor, R. N. Torah, and S. P. Beeby, "Flexible screen printed thermoelectric generator with enhanced processes and materials," *Sensors Actuators, A Phys.*, vol. 238, pp. 196–206, 2016.

[34] S. Shin *et al.*, "High-Performance Screen-Printed Thermoelectric Films on Fabrics," *Sci. Rep.*, vol. 7, no. 1, pp. 1–9, 2017.

[35] Z. Zhang, J. Qiu, and S. Wang, "Roll-to-roll printing of flexible thin-film organic thermoelectric devices," *Manuf. Lett.*, vol. 8, no. April, pp. 6–10, 2016.

[36] R. R. Søndergaard, M. Hösel, N. Espinosa, M. Jørgensen, and F. C. Krebs, "Practical evaluation of organic polymer thermoelectrics by large-area R2R processing on flexible substrates," *Energy Sci. Eng.*, vol. 1, no. 2, pp. 81–88, 2013.

[37] J. Lee, K. Cho, T. Park, and S. Kim, "Annealing effect on thermoelectric characteristics of Spin-coated Cu2Se nanoparticle thin films," *Chem. Phys. Lett.*, vol. 804, no. July, p. 139893, 2022.

[38] S. H. Lee, H. Park, S. Kim, W. Son, I. W. Cheong, and J. H. Kim, "Transparent and flexible organic semiconductor nanofilms with enhanced thermoelectric efficiency," *J. Mater. Chem. A*, vol. 2, no. 20, pp. 7288–7294, 2014.

[39] I. Cruz, "Development and optimization of thermoelectric devices based on Bi2Te3," Faculty of Sciences, University of Porto, 2016.

[40] Y. Tian, K. Loskoski, S. Meyers, B. Van Hooreweder, and F. Molina-Lopez, "Selective Laser Sintering of Blade-Coated Thermoelectric Materials with Tunable Thickness," *Proc. IEEE Sensors*, vol. 2020-Octob, pp. 14–17, 2020.

[41] G. Karalis *et al.*, "Advanced Glass Fiber Polymer Composite Laminate Operating as a Thermoelectric Generator: A Structural Device for Micropower Generation and Potential Large-Scale Thermal Energy Harvesting," *ACS Appl. Mater. Interfaces*, vol. 13, no. 20, pp. 24138–24153, 2021.

[42] H. Andersson, P. Šuly, G. Thungström, and M. Engholm, "PEDOT : PSS Thermoelectric Generators Printed on Paper Substrates," *J. Low Power Electron. Appl.*, 2019.

[43] L. K. Allison and T. L. Andrew, “A Wearable All-Fabric Thermoelectric Generator,” *Adv. Mater. Technol.*, vol. 4, no. 5, pp. 1–7, 2019.

[44] M. R. Burton *et al.*, “Thin Film Tin Selenide (SnSe) Thermoelectric Generators Exhibiting Ultralow Thermal Conductivity,” 2018.

[45] J. Du *et al.*, “Inkjet Printing Flexible Thermoelectric Devices Using Metal Chalcogenide Nanowires,” *Adv. Funct. Mater.*, 2023.

[46] W. Glatz and C. Hierold, “Flexible Micro Thermoelecrtic Generator,” *MEMS*, no. January, 2007.

[47] K. Gordiz, A. K. Menon, and S. K. Yee, “Interconnect patterns for printed organic thermoelectric devices with large fill factors,” *J. Appl. Phys.*, vol. 122, no. 12, 2017.

[48] N. H. Trung, N. Van Toan, and T. Ono, “Flexible thermoelectric power generator with Y-type structure using electrochemical deposition process,” *Appl. Energy*, vol. 1, pp. 1–10, 2017.

[49] M. Ito, T. Koizumi, H. Kojima, T. Saito, and M. Nakamura, “From materials to device design of a thermoelectric fabric for wearable energy harvesters,” *J. Mater. Chem. A*, vol. 5, no. 24, pp. 12068–12072, 2017.

[50] F. P. Brito, L. Figueiredo, L. A. Rocha, and A. P. Cruz, “Analysis of the Effect of Module Thickness Reduction on Thermoelectric Generator Output,” vol. 45, no. 3, pp. 1711–1729, 2016.

[51] K. Bethke, V. Andrei, and K. Rademann, “Decreasing the effective thermal conductivity in glass supported thermoelectric layers,” *PLoS One*, vol. 11, no. 3, pp. 1–19, 2016.

[52] S. Mortazavinatanzi, A. Rezaniakolaei, and L. Rosendahl, “Printing and folding: A solution for high-throughput processing of organic thin-film thermoelectric devices,” *Sensors (Switzerland)*, vol. 18, no. 4, 2018.

[53] S. Zhu *et al.*, “Simultaneous Realization of Flexibility and Ultrahigh Normalized Power Density in a Heatsink-Free Thermoelectric Generator via Fine Thermal Regulation,” *ACS Appl. Mater. Interfaces*, vol. 14, no. 1, pp. 1045–1055, 2022.

[54] M. Thielen, “Thermal and Electrical Energy Converters and Interfaces for the Internet of Humans,” 2018.

[55] D. P. Arnold, “Review of microscale magnetic power generation,” *IEEE Trans. Magn.*, vol. 43, no. 11, pp. 3940–3951, 2007.

[56] A. R. M. Siddique, S. Mahmud, and B. Van Heyst, “A review of the state of the science on wearable thermoelectric power generators (TEGs) and their existing challenges,” *Renew. Sustain. Energy Rev.*, vol. 73, no. January, pp. 730–744, 2017.

[57] M. Hyland, H. Hunter, J. Liu, E. Veety, and D. Vashaee, “Wearable thermoelectric generators for human body heat harvesting,” *Appl. Energy*, vol. 182, pp. 518–524, 2016.

[58] V. Leonov and R. J. M. Vullers, “Wearable electronics self-powered by using human body heat: The state of the art and the perspective,” *J. Renew. Sustain. Energy*, vol. 1, no. 6, p. 062701, Nov. 2009.

[59] S. Zhu *et al.*, “Review on Wearable Thermoelectric Generators: From Devices to Applications,” *Energies*, vol. 15, no. 9, p. 3375, 2022.

[60] Z. Lu, H. Zhang, C. Mao, and C. M. Li, “Silk fabric-based wearable thermoelectric generator for energy harvesting from the human body,” *Appl. Energy*, vol. 164, pp. 57–63, 2015.

[61] F. Suarez, D. P. Parekh, C. Ladd, D. Vashaee, M. D. Dickey, and M. C. Öztürk, “Flexible thermoelectric generator using bulk legs and liquid metal interconnects for wearable electronics,” *Appl. Energy*, vol. 202, pp. 736–745, 2017.

[62] D. Lee *et al.*, “Liquid-metal-electrode-based compact, flexible, and high-power thermoelectric device,” *Energy*, vol. 188, p. 116019, Dec. 2019.

[63] V. Leonov, T. Torfs, P. Fiorini, and C. Van Hoof, “Thermoelectric converters of human warmth for self-powered wireless sensor nodes,” *IEEE Sens. J.*, vol. 7, no. 5, pp. 650–656, 2007.

[64] H. Park *et al.*, “High power output from body heat harvesting based on flexible thermoelectric system with low thermal contact resistance,” *J. Phys. D. Appl. Phys.*, vol. 51, no. 36, p. 365501, Sep. 2018.

[65] H. Park *et al.*, “Mat-like flexible thermoelectric system based on rigid inorganic bulk materials,” *J. Phys. D. Appl. Phys.*, vol. 50, no. 49, p. 494006, Dec. 2017.

[66] K. T. Settaluri, H. Lo, and R. J. Ram, “Thin thermoelectric generator system for body energy harvesting,” *J. Electron. Mater.*, vol. 41, no. 6, pp. 984–988, 2012.

[67] A. Nozariasbmarz *et al.*, “High Power Density Body Heat Energy Harvesting,” *ACS Appl. Mater. Interfaces*, vol. 11, no. 43, pp. 40107–40113, Oct. 2019.

[68] A. Nozariasbmarz *et al.*, “Thermoelectric generators for wearable body heat harvesting: Material and device concurrent optimization,” *Nano Energy*, vol. 67, p. 104265, Jan. 2020.

[69] M. S. K. and Y. J. K. S.E. Jo, M.K. Kim, “Flexible thermoelectric generator for human body heat energy harvesting,” *Electron. Lett.*, vol. 48, no. 16, pp. 1013–1015, 2012.

[70] V. A. Online, S. J. Kim, J. H. We, and B. J. Cho, “A wearable thermoelectric generator fabricated on a glass fabric,” *Energy Environ. Sci.*, vol. 7, pp. 1959–1965, 2014.

[71] Y. Shi, Y. Wang, D. Mei, B. Feng, and Z. Chen, “Design and Fabrication of Wearable Thermoelectric Generator Device for Heat Harvesting,” no. July, pp. 1–7, 2018.

[72] Y. Wang, Y. Shi, D. Mei, and Z. Chen, “Wearable thermoelectric generator to harvest body heat for powering a miniaturized accelerometer,” *Appl. Energy*, vol. 215, pp. 690–698, Apr. 2018.

[73] J. Yuan and R. Zhu, “A fully self-powered wearable monitoring system with systematically optimized flexible thermoelectric generator,” *Appl. Energy*, vol. 271, p. 115250, Aug. 2020.

[74] S. Hong *et al.*, “Wearable thermoelectrics for personalized thermoregulation,” *Sci. Adv.*, vol. 5, no. 5, May 2019.

[75] Y. Sargolzaeiaval *et al.*, “Flexible thermoelectric generators for body heat harvesting – Enhanced device performance using high thermal conductivity elastomer encapsulation on liquid metal interconnects,” *Appl. Energy*, vol. 262, p. 114370, Mar. 2020.

[76] V. Padmanabhan Ramesh *et al.*, “Flexible thermoelectric generator with liquid metal interconnects and low thermal conductivity silicone filler,” *npj Flex. Electron.*, vol. 5, no. 1, p. 5, Mar. 2021.

[77] Y. Eom, D. Wijethunge, H. Park, S. H. Park, and W. Kim, “Flexible thermoelectric power generation system based on rigid inorganic bulk materials,” *Appl. Energy*, vol. 206, pp. 649–656, Nov. 2017.

[78] Q. Xu *et al.*, “High-performance, flexible thermoelectric generator based on bulk materials,” *Cell Reports Phys. Sci.*, vol. 3, no. 3, p. 100780, Mar. 2022.

[79] J. Kim *et al.*, “Self-charging wearables for continuous health monitoring,” *Nano Energy*, vol. 79, p. 105419, Jan. 2021.

[80] S.-J. Jung *et al.*, “Porous organic filler for high efficiency of flexible thermoelectric generator,” *Nano Energy*, vol. 81, p. 105604, Mar. 2021.

[81] C. S. Kim *et al.*, “Self-Powered Wearable Electrocardiography Using a Wearable Thermoelectric Power Generator,” *ACS Energy Lett.*, vol. 3, no. 3, pp. 501–507, Mar. 2018.

[82] S. Khan, J. Kim, K. Roh, G. Park, and W. Kim, “High power density of radiative-cooled compact thermoelectric generator based on body heat harvesting,” *Nano Energy*, vol. 87, p. 106180, Sep. 2021.

[83] Y. Liu *et al.*, “A wearable real-time power supply with a Mg3Bi2-based thermoelectric module,” *Cell Reports Phys. Sci.*, vol. 2, no. 5, p. 100412, May 2021.

[84] G. Lee, C. S. Kim, S. Kim, Y. J. Kim, H. Choi, and B. J. Cho, “Flexible heatsink based on a phase-change material for a wearable thermoelectric generator,” *Energy*, vol. 179, pp. 12–18, Jul. 2019.

[85] Y. Yang *et al.*, “Stretchable Nanolayered Thermoelectric Energy Harvester on Complex and Dynamic Surfaces,” *Nano Lett.*, vol. 20, no. 6, pp. 4445–4453, Jun. 2020.

[86] Y. Hou *et al.*, “Whole Fabric-Assisted Thermoelectric Devices for Wearable Electronics,” *Adv. Sci.*, vol. 9, no. 1, Jan. 2022.

[87] M. Zadan, M. H. Malakooti, and C. Majidi, “Soft and Stretchable Thermoelectric Generators

Enabled by Liquid Metal Elastomer Composites," *ACS Appl. Mater. Interfaces*, vol. 12, no. 15, pp. 17921–17928, Apr. 2020.

[88] B. Lee *et al.*, "High-performance compliant thermoelectric generators with magnetically self-assembled soft heat conductors for self-powered wearable electronics," *Nat. Commun.*, vol. 11, no. 1, p. 5948, Nov. 2020.

[89] L. Francioso, C. De Pascali, A. Taurino, P. Siciliano, and A. De Risi, "Wearable and flexible thermoelectric generator with enhanced package," vol. 8763, p. 876306, 2013.

[90] F. Suarez, A. Nozariasbmarz, D. Vashaee, and M. C. Öztürk, "Designing thermoelectric generators for self-powered wearable electronics," *Energy Environ. Sci.*, vol. 9, no. 6, pp. 2099–2113, 2016.

[91] I. Stark, "Converting body heat into reliable energy for powering physiological wireless sensors," *Proc. 2nd Conf. Wirel. Heal. - WH '11*, p. 1, 2011.

[92] B. Arman Kuzubasoglu and S. Kursun Bahadir, "Flexible temperature sensors: A review," *Sensors Actuators, A Phys.*, vol. 315, p. 112282, 2020.

[93] C. Bianchi *et al.*, "V 2 O 5 Thin Films for Flexible and High Sensitivity Transparent Temperature Sensor," *Adv. Mater. Technol.*, pp. 1600077–6, 2016.

[94] J. Figueira *et al.*, "Optimization of Cuprous Oxides Thin Films to be used as Thermoelectric Touch Detectors," *ACS Appl. Mater. Interfaces*, vol. 9, no. 7, 2017.

[95] M. Ruoho, T. Juntunen, T. Alasaarela, M. Pudas, and I. Tittonen, "Transparent, Flexible, and Passive Thermal Touch Panel," *Adv. Mater. Technol.*, pp. 1600204–10, 2016.

[96] H. Park, S. H. Lee, F. S. Kim, H. H. Choi, I. W. Cheong, and J. H. Kim, "Enhanced thermoelectric properties of PEDOT:PSS nanofilms by a chemical dedoping process," *J. Mater. Chem. A*, vol. 2, no. 18, pp. 6532–6539, 2014.

[97] E. M. F. Vieira *et al.*, "Enhanced thermoelectric properties of Sb2Te3 and Bi2Te3 films for flexible thermal sensors," *J. Alloys Compd.*, vol. 774, pp. 1102–1116, 2019.

[98] J. Figueira, J. Loureiro, E. Vieira, E. Fortunato, R. Martins, and L. Pereira, "Flexible, scalable, and efficient thermoelectric touch detector based on PDMS and graphite flakes," *Flex. Print. Electron.*, vol. 6, no. 4, 2021.

[99] T. Koskinen, T. Juntunen, and I. Tittonen, "Large-Area Thermal Distribution Sensor Based on Multilayer Graphene Ink," *Sensors*, vol. 20, no. 18, p. 5188, Sep. 2020.

[100] X. Gong, L. Zhang, Y. Huang, S. Wang, G. Pan, and L. Li, "Directly writing flexible temperature sensor with graphene nanoribbons for disposable healthcare devices," *RSC Adv.*, vol. 10, no. 37, pp. 22222–22229, 2020.

[101] Y. M. Lee, A. Lim, R. Park, and H. Kim, "High-performance thermoelectric bracelet based on carbon nanotube ink printed directly onto a flexible cable," pp. 19727–19734, 2018.

[102] I. M. Abdel-Motaleb and S. M. Qadri, "Thermoelectric Devices: Principles and Future Trends," Apr. 2017.

[103] L.(Brun-Conti).Bender, "Chemistry/Trace/Paint and Coating," in *Encyclopedia of Forensic Sciences*, 2nd ed., Elsevier Ltd, 2013, pp. 273–278.

[104] M. Schmitz, M. Khalilbeigi, M. Balwierz, R. Lissermann, M. Mühlhaüser, and J. Steimle, "Capricate: A fabrication pipeline to design and 3D printcapacitive touch sensors for interactive objects," *UIST 2015 - Proc. 28th Annu. ACM Symp. User Interface Softw. Technol.*, pp. 253–258, 2015.

[105] E. M. F. Vieira *et al.*, "Highly sensitive thermoelectric touch sensor based on p-type SnO x thin film," *Nanotechnology*, vol. 30, no. 43, 2019.

[106] European Chemical Society, "Periodic Table Highlighting Elements Scarcity," 2019. [Online]. Available: https://www.euchems.eu/euchems-periodic-table/.

[107] V. V. Popov *et al.*, "Powder bed fusion additive manufacturing using critical raw materials: A review," *Materials (Basel).*, vol. 14, no. 4, pp. 1–37, 2021.

[108] Y. Zhang, Y. Heo, M. Park, and S. Park, "Recent Advances in Organic Thermoelectric Materials :

Principle Mechanisms and Emerging Carbon-Based Green Energy Materials," *Polymers (Basel).*, vol. 11, no. 167, 2019.

[109] E. W. Zaia, M. P. Gordon, P. Yuan, and J. J. Urban, "Progress and Perspective : Soft Thermoelectric Materials for Wearable and Internet-of-Things Applications," *Adv. Electron. Mater.*, vol. 1800823, no. Soft Thermoelectrics, pp. 1–20, 2019.

[110] A. Claypole, J. Claypole, T. Claypole, D. Gethin, and L. Kilduff, "The effect of plasma functionalization on the print performance and time stability of graphite nanoplatelet electrically conducting inks," *J. Coatings Technol. Res.*, vol. 18, no. 1, pp. 193–203, 2021.

[111] A. Claypole, J. Claypole, A. Holder, T. C. Claypole, and L. Kilduff, "Rheology of high-aspect-ratio nanocarbons dispersed in a low-viscosity fluid," *J. Coatings Technol. Res.*, vol. 17, no. 4, pp. 1003–1012, 2020.

[112] L. Gallais, T. Vidal, E. Lescoute, Y. Pontillon, and J. L. Rullier, "High power continuous wave laser heating of graphite in a high temperature range up to 3800 K," *J. Appl. Phys.*, vol. 129, no. 4, 2021.

[113] V. Tran and S. Volz, "High thermoelectric performance of graphite nanofibers," *Nanoscale*, no. 8, 2018.

[114] A. R. Correia, "Tailoring Carbon-Based Materials for Thermoelectric Application," Universidade do Porto, 2019.

[115] C. Phillips, A. Al-Ahmadi, S.-J. Potts, T. Claypole, and D. Deganello, "The effect of graphite and carbon black ratios on conductive ink performance," *J. Mater. Sci.*, vol. 52, no. 16, pp. 9520–9530, 2017.

[116] Y. Du, H. Li, X. Jia, Y. Dou, J. Xu, and P. Eklund, "Preparation and Thermoelectric Properties of Graphite/poly(3,4-ethyenedioxythiophene) Nanocomposites," pp. 4–12, 2018.

[117] R. Mulla, D. R. Jones, and C. W. Dunnill, "Thermoelectric Paper : Graphite Pencil Traces on Paper to Fabricate a Thermoelectric Generator," *Adv. Mater. Technol.*, vol. 5, 2020.

[118] P. K. Rademann *et al.*, "As featured in : copper (I) oxide – graphite – polymer pastes and the applications of such flexible composites †," *Phys. Chem. Chem. Phys.*, 2016.

[119] Y. Du, J. Xu, Y. Wang, and T. Lin, "Thermoelectric properties of graphite-PEDOT : PSS coated flexible polyester fabrics," *J. Mater. Sci. Mater. Electron.*, vol. 28, no. 8, pp. 5796–5801, 2017.

[120] H. R. K. M. Emani *et al.*, "Development of a Screen-Printed Flexible Porous Graphite Electrode for Li-Ion Battery," in *2021 IEEE International Conference on Flexible and Printable Sensors and Systems (FLEPS)*, 2021, pp. 1–4.

[121] R. O. Kadara, N. Jenkinson, B. Li, K. H. Church, and C. E. Banks, "Manufacturing electrochemical platforms : Direct-write dispensing versus screen printing," *Electrochem. commun.*, vol. 10, pp. 1517–1519, 2008.

[122] V. V. Brus, M. Gluba, J. Rappich, F. Lang, P. D. Maryanchuk, and N. H. Nickel, "Fine Art of Thermoelectricity," *ACS Appl. Mater. Interfaces*, vol. 10, no. 5, pp. 4737–4742, 2018.

[123] A. Nag, N. Afasrimanesh, S. Feng, and S. C. Mukhopadhyay, "Strain induced graphite/PDMS sensors for biomedical applications," *Sensors Actuators, A Phys.*, vol. 271, pp. 257–269, 2018.

[124] W. P. Shih *et al.*, "Flexible temperature sensor array based on a Graphite-Polydimethylsiloxane composite," *Sensors*, vol. 10, no. 4, pp. 3597–3610, 2010.

[125] A. K. Gautam, M. Faraz, and N. Khare, "Enhanced thermoelectric properties of MoS2 with the incorporation of reduced graphene oxide (RGO)," *J. Alloys Compd.*, vol. 838, p. 155673, 2020.

[126] G. Tang, K. Cai, J. Cui, J. Yin, and S. Shen, "Preparation and thermoelectric properties of MoS2/Bi2Te3 nanocomposites," *Ceram. Int.*, vol. 42, no. 16, pp. 17972–17977, 2016.

[127] N. J. A. Cordeiro *et al.*, "Fast and low-cost synthesis of MoS2 nanostructures on paper substrates for near-infrared photodetectors," *Appl. Sci.*, vol. 11, no. 3, pp. 1–15, 2021.

[128] "Web of Science." [Online]. Available: https://www.webofscience.com/wos/woscc/advanced-search.

[129] I. Cunha, "Printed and drawn flexible electronics based on cellulose nanocomposites," School

of Science and Technology, NOVA University Lisbon, 2021.

[130] E. Carlos, “Design and synthesis of low temperature printed metal oxide electronics,” School of Science andTechnology, NOVA University Lisbon, 2020.

[131] L. P. R. Barras, I. Cunha, D. Gaspar, E. Fortunato, R. Martins *et al.*, “Printable cellulose-based electroconductive composites for sensing elements in paper electronics,” *Flex. Print. Electron.*, vol. 2, pp. 1–12, 2017.

[132] K. Hasan, O. Nur, M. Willander, K. Hasan, O. Nur, and M. Willander, “Screen printed ZnO ultraviolet photoconductive sensor on pencil drawn circuitry over paper,” *Appl. Phys. Lett.*, vol. 100, 2012.

[133] N. Lezi, S. Economopoulos, M. Prodromidis, A. Economou, and N. Tagmatarchis, “Fabrication of a ‘Green’ and Low-Cost Screen-Printed Graphene Sensor and Its Application to the Determination of Caffeine by Adsorptive Stripping Voltammetry,” *Int. J. Electrochem. Sci.*, vol. 12, pp. 6054–6067, 2017.

[134] J. Ferri, J. Vicente, J. Moreno, G. Martinez, and E. Garcia-Breijo, “A Wearable Textile 2D Touchpad Sensor Based on Screen-Printing Technology,” *Materials (Basel).*, vol. 10, no. 1450, 2017.

[135] B. Tian *et al.*, “Optimization on thermoelectric characteristics of indium tin oxide/indium oxide thin film thermocouples based on screen printing technology,” *Rev. Sci. Instrum.*, vol. 92, no. 10, 2021.

[136] E. Dimitriou and N. Michailidis, “Printable conductive inks used for the fabrication of electronics: An overview,” *Nanotechnology*, vol. 32, no. 50, 2021.

[137] S. Ferhat, C. Domain, J. Vidal, D. Noël, B. Ratier, and B. Lucas, “Flexible thermoelectric device based on TiS2(HA)x n-type nanocomposite printed on paper,” *Org. Electron.*, vol. 68, no. February, pp. 256–263, 2019.

[138] H. Andersson *et al.*, “PEDOT: PSS thermoelectric generators printed on paper substrates,” *J. Low Power Electron. Appl.*, vol. 9, no. 2, 2019.

[139] S. J. Kim, J. H. We, and B. J. Cho, “A wearable thermoelectric generator fabricated on a glass fabric,” *Energy Environ. Sci.*, vol. 7, no. 6, p. 1959, 2014.

[140] T. Carvalho, V. Dubceac, P. Grey, and E. Fortunato, “Fully Printed Zinc Oxide Electrolyte-Gated Transistors on Paper,” pp. 1–9, 2019.

[141] J. Figueira *et al.*, “Sustainable Fully Printed UV Sensors on Cork Using Zinc Oxide / Ethylcellulose Inks,” *Micromachines*, vol. 10, no. 9, pp. 1–10, 2019.

[142] Y. Zhang *et al.*, “Ink formulation, scalable applications and challenging perspectives of screen printing for emerging printed microelectronics,” *J. Energy Chem.*, vol. 63, pp. 498–513, 2021.

[143] D. Gaspar, “Active cellulose-based substrates for application in electronic devices,” School of Science and Technology, NOVA University Lisbon, 2019.

[144] H. Ling, R. Chen, Q. Huang, F. Shen, Y. Wang, and X. Wang, “Transparent, flexible and recyclable nanopaper-based touch sensors fabricated via inkjet-printing,” *Green Chem.*, vol. 22, pp. 3208–3215, 2020.

[145] S. Kanaparthi and S. Badhulika, “Chemical Low cost , flexible and biodegradable touch sensor fabricated by solvent-free processing of graphite on cellulose paper,” *Sensors Actuators B. Chem.*, vol. 242, pp. 857–864, 2017.

[146] J. P. Rojas, D. Conchouso, A. Arevalo, D. Singh, I. G. Foulds, and M. M. Hussain, “Paper-based origami flexible and foldable thermoelectric nanogenerator,” *Nano Energy*, vol. 31, no. October 2016, pp. 296–301, 2017.

[147] Z. Dong *et al.*, “Facile fabrication of paper-based flexible thermoelectric generator,” *npj Flex. Electron.*, pp. 0–5, 2021.

[148] M. Jung, S. Jeon, and J. Bae, “Scalable and facile synthesis of stretchable thermoelectric fabric for wearable self-powered temperature sensors †,” pp. 39992–39999, 2018.

[149] A. J. Karttunen, L. Sarnes, R. Townsend, J. Mikkonen, and M. Karppinen, “Flexible

Thermoelectric ZnO–Organic Superlattices on Cotton Textile Substrates by ALD/MLD," *Adv. Electron. Mater.*, vol. 3, no. 6, 2017.

[150] A. J. Paleo *et al.*, "Vapor grown carbon nanofiber based cotton fabrics with negative thermoelectric power," *Cellulose*, vol. 27, no. 15, pp. 9091–9104, 2020.

[151] S. A. Hosseini Ravandi and M. Valizadeh, "Properties of fibers and fabrics that contribute to human comfort," in *Improving Comfort in Clothing*, G. Song, Ed. Woodhead Publishing, 2011, pp. 61–78.

[152] R. Gonçalves *et al.*, "RFID-Based Wireless Passive Sensors Utilizing Cork Materials," *IEEE Sens. J.*, vol. 15, no. 12, pp. 7242–7251, 2015.

[153] R. Sugumar, S. Angappane, P. Adhikary, and D. Mandal, "Ultraviolet photodetection characteristics of Zinc oxide thin films and nanostructures," *IOP Conf. Ser. Mater. Sci. Eng.*, vol. 115, 2016.

[154] P. Pattamang, K. Jiramitmonkon, and P. Piyakulawat, "Photoresponse of composites of zinc oxide and poly(3-hexythiophene) under selective UV and white-light illumination," *Org. Electron.*, vol. 39, pp. 105–112, 2016.

[155] S. K. Panda and C. Jacob, "Preparation of transparent ZnO thin films and their application in UV sensor devices," *Solid-State Elecronics*, vol. 73, pp. 44–50, 2012.

[156] N. H. Al-hardan, M. A. A. Hamid, R. Shamsudin, and N. K. Othman, "Ultraviolet Sensors Based on Two-Dimensional Zinc Oxide Structures," in *Optoelectronics - Advanced Device Structures*, INTECH, 2017, pp. 251–267.

[157] C. Soci *et al.*, "ZnO Nanowire UV Photodetectors with High Internal Gain," *Nano Lett.*, vol. 7, no. 4, pp. 1003–1009, 2007.

[158] B. Mallampati, S. V Nair, H. E. Ruda, and U. Philipose, "Role of surface in high photoconductive gain measured in ZnO nanowire-based photodetector," *J. Nanoparticle Res.*, vol. 17, pp. 176–186, 2015.

[159] A. P. M. Tavares, M. H. de Sá, and M. G. F. Sales, "Innovative screen-printed electrodes on cork composite substrates applied to sulfadiazine electrochemical sensing," *J. Electroanal. Chem.*, vol. 880, p. 114922, 2021.

[160] N. Gama, A. Ferreira, and A. Barros-Timmons, "3D printed cork/polyurethane composite foams," *Mater. Des.*, vol. 179, p. 107905, 2019.

[161] F. Daver, K. P. M. Lee, M. Brandt, and R. Shanks, "Cork–PLA composite filaments for fused deposition modelling," *Compos. Sci. Technol.*, vol. 168, no. September, pp. 230–237, 2018.

[162] F. Brites *et al.*, "Cork Plastic Composite Optimization for 3D Printing Applications," *Procedia Manuf.*, vol. 12, no. December 2016, pp. 156–165, 2017.

[163] M. L. Seol *et al.*, "Printing of a passivation layer for the protection of printed supercapacitors," *ACS Appl. Electron. Mater.*, vol. 2, no. 11, pp. 3643–3649, 2020.

[164] C. Gaspar, J. Olkkonen, S. Passoja, and M. Smolander, "Paper as active layer in inkjet-printed capacitive humidity sensors," *Sensors (Switzerland)*, vol. 17, no. 7, pp. 1–10, 2017.

[165] N. M. Nair, I. Khanra, D. Ray, and P. Swaminathan, "Silver Nanowire-Based Printable Electrothermochromic Ink for Flexible Touch-Display Applications," *ACS Appl. Mater. Interfaces*, vol. 13, no. 29, pp. 34550–34560, 2021.

[166] A. K. Jaiswal, A. Hokkanen, V. Kumar, T. Mäkelä, A. Harlin, and H. Orelma, "Thermoresponsive Nanocellulose Films as an Optical Modulation Device: Proof-of-Concept," *ACS Appl. Mater. Interfaces*, vol. 13, pp. 25346–25356, 2021.

[167] S. Smocot, Z. Zhang, L. Zhang, S. Guo, and C. Cao, "Printed flexible mechanical sensors," *Nanoscale*, vol. 14, no. 46, pp. 17134–17156, 2022.

[168] J. Figueira *et al.*, "Screen-printed, flexible, and eco-friendly thermoelectric touch sensors based on ethyl cellulose and graphite flakes inks," *Flex. Print. Electron.*, vol. 8, 2023.

[169] S. Tachibana *et al.*, "Flexible printed temperature sensor with high humidity stability using bilayer passivation," *Flex. Print. Electron.*, vol. 6, no. 3, p. 034002, Sep. 2021.

[170] T. Kinkeldei, N. Munzenrieder, C. Zysset, K. Cherenack, and G. Tröster, “Encapsulation for flexible electronic devices,” *IEEE Electron Device Lett.*, vol. 32, no. 12, pp. 1743–1745, 2011.

[171] Z. Cui, *Printed Electronics: Materials, Technologies and Applications*. 2016.

[172] Y. Li, S. Arumugam, C. Krishnan, and M. D. B. Charlton, “Encapsulated Textile Organic Solar Cells Fabricated by Spray Coating,” pp. 407–412, 2019.

[173] F. Brunetti *et al.*, “Printed Solar Cells and Energy Storage Devices on Paper Substrates,” *Adv. Funct. Mater.*, vol. 29, no. 21, 2019.

[174] J. C. Zhu *et al.*, “A flexible micro direct methanol fuel cells array based on FPCB,” *Energy Convers. Manag.*, vol. 258, no. March, p. 115469, 2022.

[175] Z. Fan, Y. Zhang, L. Pan, J. Ouyang, and Q. Zhang, “Recent developments in flexible thermoelectrics : From materials to devices,” *Renew. Sustain. Energy Rev.*, no. October, p. 110448, 2020.

[176] Z. Li *et al.*, “Efficient strain modulation of 2D materials via polymer encapsulation,” *Nat. Commun.*, vol. 11, no. 1, pp. 1–8, 2020.

[177] Q. Zhang, Y. Di, C. M. Huard, L. J. Guo, J. Wei, and J. Guo, “Highly stable and stretchable graphene-polymer processed silver nanowires hybrid electrodes for flexible displays,” *J. Mater. Chem. C*, vol. 3, no. 7, pp. 1528–1536, 2015.

[178] J. Zheng *et al.*, “Integrating recyclable polymers into thermoelectric devices for green electronics,” *J. Mater. Chem. A*, vol. 10, no. 37, pp. 19787–19796, 2022.

[179] J. C. Agar, K. J. Lin, R. Zhang, J. Durden, K. S. Moon, and C. P. Wong, “Novel PDMS(silicone)-in-PDMS(silicone): Low cost flexible electronics without metallization,” *Proc. - Electron. Components Technol. Conf.*, pp. 1226–1230, 2010.

[180] L. Wu *et al.*, “Screen-printed flexible temperature sensor based on FG/CNT/PDMS composite with constant TCR,” *J. Mater. Sci. Mater. Electron.*, vol. 30, no. 10, pp. 9593–9601, 2019.

[181] Q. I. U. Lin *et al.*, “Experimental Characterization and Model Verification of Thermal Conductivity from Mesoporous to Macroporous SiOC Ceramics,” *J. Therm. Sci.*, vol. 30, no. 2, pp. 465–476, 2021.

[182] X. Niu, S. Peng, L. Liu, W. Wen, and P. Sheng, “Characterizing and patterning of PDMS-based conducting composites,” *Adv. Mater.*, vol. 19, no. 18, pp. 2682–2686, 2007.

[183] S. Ammar, K. Ramesh, B. Vengadaesvaran, S. Ramesh, and A. K. Arof, “Amelioration of anticorrosion and hydrophobic properties of epoxy/PDMS composite coatings containing nano ZnO particles,” *Prog. Org. Coatings*, vol. 92, pp. 54–65, 2016.

[184] G. Gomathi Sankar *et al.*, “Polydimethyl siloxane nanocomposites: Their antifouling efficacy invitro and in marine conditions,” *Int. Biodeterior. Biodegrad.*, vol. 104, pp. 307–314, 2015.

[185] I. Babu and G. de With, “Highly flexible piezoelectric 0-3 PZT-PDMS composites with high filler content,” *Compos. Sci. Technol.*, vol. 91, pp. 91–97, 2014.

[186] Y. Wang, W. Zhu, Y. Deng, B. Fu, P. Zhu, and Y. Yu, “Self-powered wearable pressure sensing system for continuous healthcare monitoring enabled by flexible thin-film thermoelectric generator,” *Nano Energy*, vol. 73, no. March, 2020.

[187] D. Niu *et al.*, “Reversible Bending Behaviors of Photomechanical Soft Actuators Based on Graphene Nanocomposites,” *Sci. Rep.*, vol. 6, no. June, pp. 1–10, 2016.

[188] K. K. Jung, Y. Jung, C. J. Choi, J. M. Lee, and J. S. Ko, “Flexible thermoelectric generator with polydimethyl siloxane in thermoelectric material and substrate,” *Curr. Appl. Phys.*, vol. 16, no. 10, pp. 1442–1448, 2016.

[189] L. Gil, “Cork: a strategic material,” *Front. Chem.*, vol. 2, no. April, pp. 1–2, 2014.

[190] M. Margarida, J. Moura, and R. Galhano, “Ultimate use of Cork - Unorthodox and innovative applications,” *Ciência Tecnol. dos Mater.*, vol. 29, no. 2, pp. 65–72, 2017.

[191] I. M. A. Aroso, A. R. R. Araújo, R. A. Pires, and R. L. Reis, “Cork: current technological developments and future perspectives for this natural, renewable, and sustainable material,” *ACS Sustain. Chem. Eng.*, vol. 5, no. 12, pp. 11130–11146, 2017.

[192] L. Gil, “Cortiça,” in *Ciência e Engenharia de Materiais de Construção*, 2012, pp. 663–715.

[193] L. Gil, “New cork-based materials and applications,” *Materials (Basel).*, vol. 8, no. 2, pp. 625–637, 2015.

[194] E. Carlos, R. Branquinho, P. Barquinha, R. Martins, and E. Fortunato, “New strategies toward high-performance and low-temperature processing of solution-based metal oxide TFTs,” in *Chemical Solution Synthesis for Materials Design and Thin Film Device Applications*, Elsevier, 2021, pp. 585–621.

[195] S. Spiegel, “Recent advances in applied polymer science,” *J. Appl. Polym. Sci.*, vol. 135, no. 24, Jun. 2018.

[196] K. Tufail Chaudhary, “Thin Film Deposition: Solution Based Approach,” in *Thin Films*, IntechOpen, 2021.

[197] “What are Laminating Pouches and why use them?,” 2017. [Online]. Available: https://www.zentesi.com/. [Accessed: 22-Sep-2023].

[198] “What is Laminating Film Made Out of?,” 2017. [Online]. Available: https://lamin-8.ca. [Accessed: 22-Sep-2023].

[199] M. Crescentini, S. F. Syeda, and G. P. Gibiino, “Hall-Effect Current Sensors: Principles of Operation and Implementation Techniques,” *IEEE Sens. J.*, vol. 22, no. 11, pp. 10137–10151, 2022.

[200] M. J. Lewis, “Viscosity,” in *Physical Properties of Foods and Food Processing Systems*, M. J. Lewis, Ed. Elsevier, 1996, pp. 108–136.

[201] J. Hapanowicz, “Proposition of non-standard method useful for viscosity measurements of unstable two-phase systems coupled with examples of its application,” *Measurement: Journal of the International Measurement Confederation*, vol. 164. 2020.

[202] “An Introduction to Viscometers.” [Online]. Available: https://www.scimed.co.uk/. [Accessed: 23-Sep-2023].

[203] A. Abdullah and A. Mohammed, “Scanning Electron Microscopy (SEM): A Review,” in *Proceedings of 2018 International Conference on Hydraulics and Pneumatics - HERVEX*, 2019, pp. 77–85.

[204] J. Deuermeier, “Origins of limited electrical performance of polycrystalline Cu2O thin-film transistors,” School of Science and Technology, NOVA University Lisbon, 2016.

[205] Y. Yuan and T. R. Lee, “Surface science techniques,” in *Springer Series in Surface Sciences*, vol. 51, no. 1, G. Bracco and B. Holst, Eds. Springer-Verlag Berlin Heidelberg, 2013.

[206] S. A. Naziri Mehrabani, V. Vatanpour, and I. Koyuncu, “Green solvents in polymeric membrane fabrication: A review,” *Sep. Purif. Technol.*, vol. 298, no. July, p. 121691, 2022.

[207] S. Chae *et al.*, “Isolation of nb2se9 molecular chain from bulk one-dimensional crystal by liquid exfoliation,” *Nanomaterials*, vol. 8, no. 10, pp. 1–9, 2018.

[208] R. Ding, S. Chen, H. Xuan, B. Li, and Y. Rui, “Green-solvent-processed amphiphobic polyurethane nanofiber membranes with mechanically stable hierarchical structures for seawater desalination by membrane distillation,” *Desalination*, vol. 516, no. June, p. 115223, 2021.

[209] Z. Cao, “Printable Thermoelectric Devices for Energy Harvesting,” Faculty of Physical Science and Engineering, 2014.

[210] T. Öhlund, “Metal Films for Printed Electronics : Ink-substrate Interactions and Sintering,” 2014.

[211] R. A. Angelova, “Organic Cotton: Technological and Environmental Aspects,” in *XXIII International Scientific Conference FPEPM 2018*, 2019, no. March, pp. 351–356.

[212] D. Atalie, A. Ferede, and G. K. Rotich, “Effect of weft yarn twist level on mechanical and sensorial comfort of 100% woven cotton fabrics,” *Fash. Text.*, vol. 6, no. 1, 2019.

[213] Bostik, “Safety Data Sheet EVO-STIK EVO-BOND WATERPROOF PVA,” 2011. [Online]. Available: https://www.farnell.com/datasheets/1504152.pdf. [Accessed: 25-Sep-2023].

[214] P. Sahu and M. Gupta, “Water absorption behavior of cellulosic fibres polymer composites: A review on its effects and remedies,” *J. Ind. Text.*, vol. 51, no. 5_suppl, pp. 7480S-7512S, Jun.

2022.

[215] A. Goudarzi, A. Soleimani-Gorgani, and O. Avinc, “Generation of Flexible Multifunctional Electronic Textile Displaying Appropriate Fastness Properties Utilizing Single-Stage Inkjet Printing onto Cotton Fabric Pre-treated with PVC,” *Fibers Polym.*, vol. 24, no. 2, pp. 555–573, Feb. 2023.

[216] J. Huang *et al.*, “Hybrid asynchronous brain-computer interface for yes/no communication in patients with disorders of consciousness,” *J. Neural Eng.*, vol. 18, no. 5, 2021.

[217] H. Chang *et al.*, “Ultrasensitive and Highly Stable Resistive Pressure Sensors with Biomaterial-Incorporated Interfacial Layers for Wearable Health-Monitoring and Human-Machine Interfaces,” *ACS Appl. Mater. Interfaces*, vol. 10, no. 1, pp. 1067–1076, 2018.

[218] Z. Wang, L. Zhang, J. Liu, H. Jiang, and C. Li, “Flexible hemispheric microarrays of highly pressure-sensitive sensors based on breath figure method,” *Nanoscale*, vol. 10, no. 22, pp. 10691–10698, 2018.

[219] V. Karthikeyan *et al.*, “Wearable and flexible thin film thermoelectric module for multi-scale energy harvesting,” *J. Power Sources*, vol. 455, no. February, p. 227983, 2020.

[220] L. Wang, X. Jia, D. Wang, G. Zhu, and J. Li, “Preparation and thermoelectric properties of polythiophene/multiwalled carbon nanotube composites,” *Synth. Met.*, vol. 181, pp. 79–85, Oct. 2013.

[221] Z. Wei, Z. Li, P. Luo, J. Zhang, and J. Luo, “Simultaneously increased carrier concentration and mobility in p-type Bi0.5Sb1.5Te3 throng Cd doping,” *J. Alloys Compd.*, vol. 830, 2020.

[222] Y. Xu, X. Wang, and Q. Hao, “A mini review on thermally conductive polymers and polymer-based composites,” *Compos. Commun.*, vol. 24, p. 100617, Apr. 2021.

[223] X. Guan and J. Ouyang, “Enhancement of the Seebeck Coefficient of Organic Thermoelectric Materials via Energy Filtering of Charge Carriers,” *CCS Chem.*, vol. 3, no. 10, pp. 2415–2427, 2021.

[224] Z. Tao, H. Wang, X. Li, Z. Liu, and Q. Guo, “Expanded graphite/polydimethylsiloxane composites with high thermal conductivity,” *J. Appl. Polym. Sci.*, vol. 134, no. 21, pp. 1–7, 2017.

[225] K. Janeczek, “Composite materials for printed electronics in Internet of Things applications,” *Bull. Mater. Sci.*, vol. 43, no. 1, p. 124, Dec. 2020.

[226] Y. Khan, A. Thielens, S. Muin, J. Ting, C. Baumbauer, and A. C. Arias, “A New Frontier of Printed Electronics: Flexible Hybrid Electronics,” *Adv. Mater.*, vol. 32, no. 15, Apr. 2020.

[227] N. J. A. Cordeiro, “Crescimento Direto de Nanoestruturas de MoS2 em Substratos de Papel utilizando a Síntese Hidrotermal por Microondas: Ajuste de Propriedades e produção de Sensores de Baixo Custo,” Universidade Estadual de Londrina, 2021.

[228] H. Fan, R. Wu, H. Liu, X. Yang, Y. Sun, and C. Chen, “Synthesis of metal-phase-assisted 1T@2H-MoS2 nanosheet-coated black TiO2 spheres with visible light photocatalytic activities,” *J. Mater. Sci.*, vol. 53, no. 14, pp. 10302–10312, Jul. 2018.

[229] S. Radhakrishnan, P. Mane, K. A. Sree Raj, B. Chakraborty, and C. S. Rout, “In-situ construction of hierarchical 2D MoS2/1D Te hybrid for supercapacitor applications,” *J. Energy Storage*, vol. 60, p. 106703, Apr. 2023.

[230] M. L. Matias *et al.*, “Floating TiO2-Cork Nano-Photocatalysts for Water Purification Using Sunlight,” *Sustainability*, vol. 14, no. 15, p. 9645, Aug. 2022.

[231] Ashraf, Forsberg, Mattsson, and Thungström, “Thermoelectric Properties of n-Type Molybdenum Disulfide (MoS2) Thin Film by Using a Simple Measurement Method,” *Materials (Basel).*, vol. 12, no. 21, p. 3521, Oct. 2019.

[232] J. Wu, H. Schmidt, K. K. Amara, X. Xu, G. Eda, and B. Özyilmaz, “Large thermoelectricity via variable range hopping in chemical vapor deposition grown single-layer MoS2,” *Nano Lett.*, vol. 14, no. 5, pp. 2730–2734, 2014.

APPENDICES

A CARBON INK TECHNICAL DATA SHEET

In **Appendix Figure 1** there is an excerpt of the technical data sheet of the used carbon ink in the screen-printing process (introduced in **section 4.2.1**) which presents some of the ink's typical properties such as its viscosity and sheet resistance.

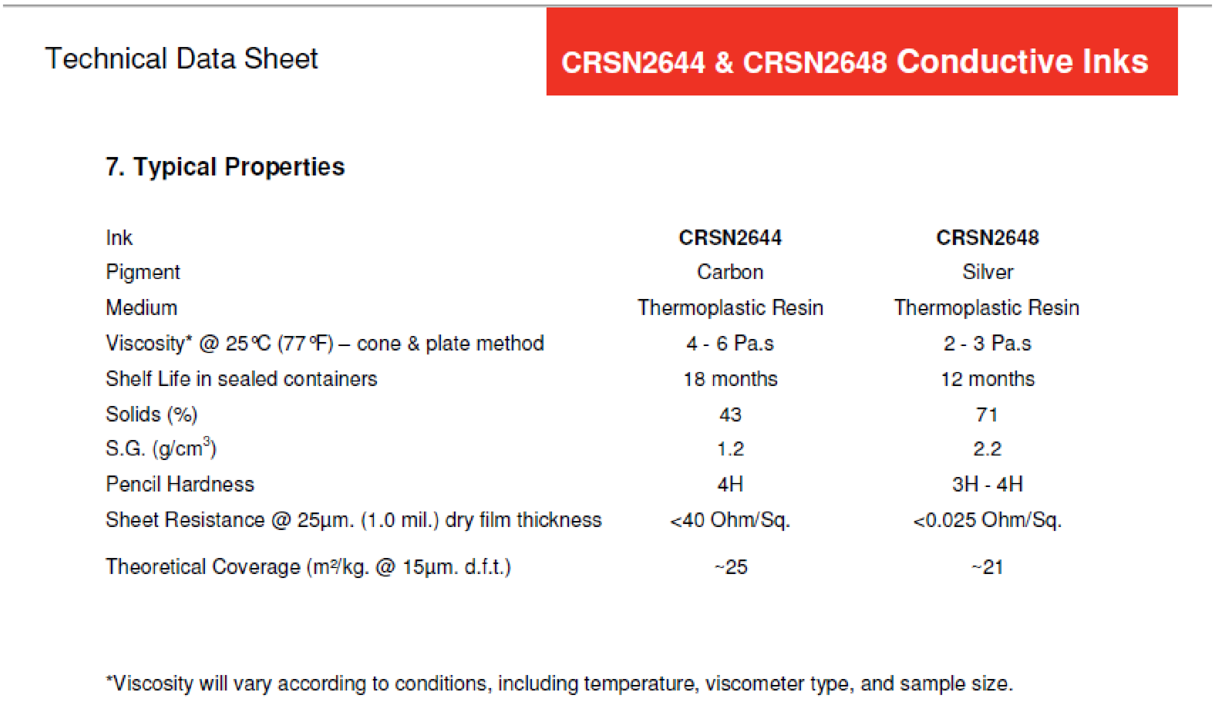

Technical Data Sheet

CRSN2644 & CRSN2648 Conductive Inks

7. Typical Properties

Ink	**CRSN2644**	**CRSN2648**
Pigment	Carbon	Silver
Medium	Thermoplastic Resin	Thermoplastic Resin
Viscosity* @ 25 °C (77 °F) – cone & plate method	4 - 6 Pa.s	2 - 3 Pa.s
Shelf Life in sealed containers	18 months	12 months
Solids (%)	43	71
S.G. (g/cm^3)	1.2	2.2
Pencil Hardness	4H	3H - 4H
Sheet Resistance @ 25µm. (1.0 mil.) dry film thickness	<40 Ohm/Sq.	<0.025 Ohm/Sq.
Theoretical Coverage (m^2/kg. @ 15µm. d.f.t.)	~25	~21

*Viscosity will vary according to conditions, including temperature, viscometer type, and sample size.

Appendix Figure 1 - Description of characteristic properties of the CRSN2644 carbon ink.

B | SEEBECK COEFFICIENT CALCULATION

The Seebeck coefficient was measured as described in the **section 3.2.3**. These are the data plots used for the S calculations of screen-printed EC/G_{Flakes} films, presented in **Figure 4.8**.

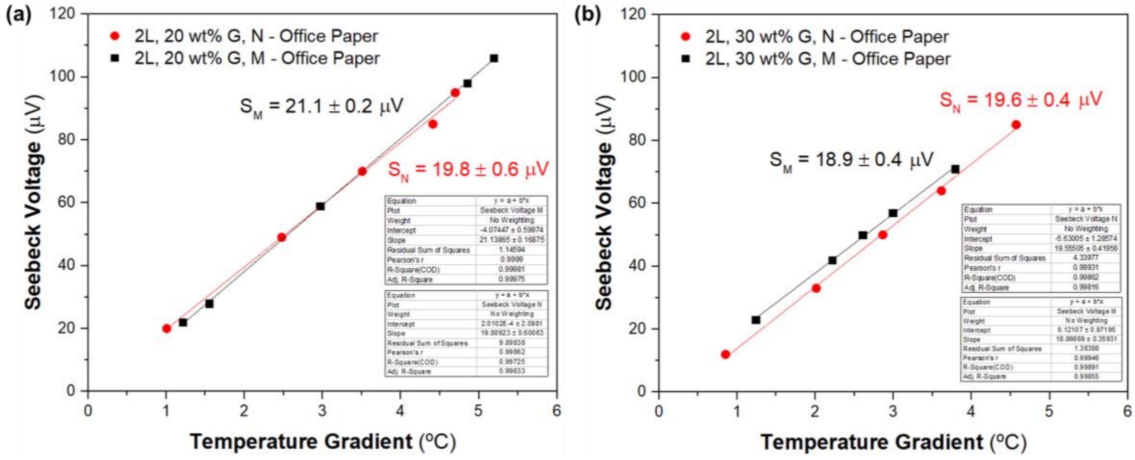

Appendix Figure 2 - Seebeck coefficient measurements for OP samples with 2 printed layers of: **(a)** 20 wt% G ink and **(b)** 30 wt% of G ink.

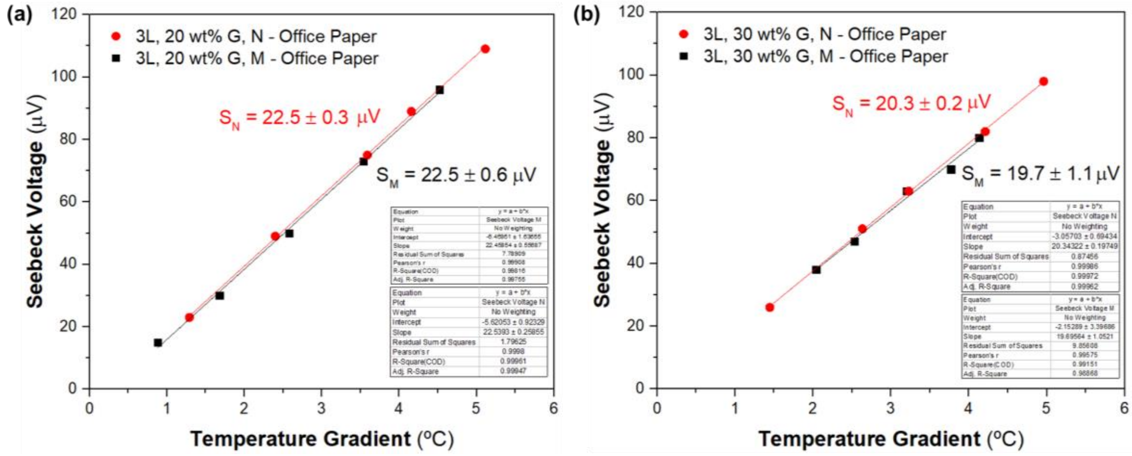

Appendix Figure 3 - Seebeck coefficient measurements for OP samples with 3 printed layers of: **(a)** 20 wt% G ink and **(b)** 30 wt% of G ink.

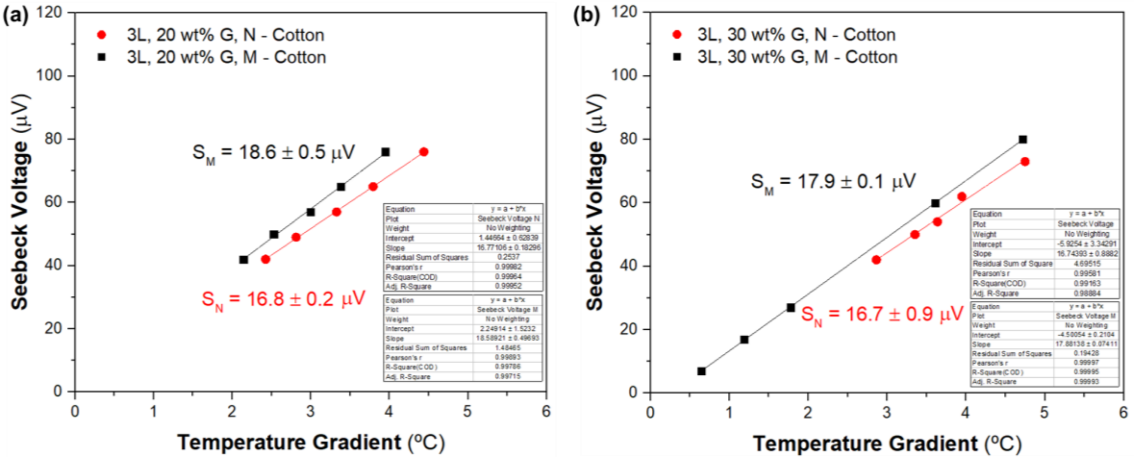

Equation	y = a + b*x
Plot	Seebeck Voltage N
Weight	No Weighting
Intercept	1.44664 ± 0.62839
Slope	16.77106 ± 0.18296
Residual Sum of Squares	0.2537
Pearson's r	0.99982
R-Square(COD)	0.99964
Adj. R-Square	0.99952

Equation	y = a + b*x
Plot	Seebeck Voltage M
Weight	No Weighting
Intercept	2.24914 ± 1.5232
Slope	18.58921 ± 0.49693
Residual Sum of Squares	1.48465
Pearson's r	0.99893
R-Square(COD)	0.99786
Adj. R-Square	0.99715

Equation	y = a + b*x
Plot	Seebeck Voltage
Weight	No Weighting
Intercept	-5.9254 ± 3.34291
Slope	16.74393 ± 0.8882
Residual Sum of Square	4.69515
Pearson's r	0.99581
R-Square(COD)	0.99163
Adj. R-Square	0.98884

Equation	y = a + b*x
Plot	Seebeck Voltage M
Weight	No Weighting
Intercept	-4.50054 ± 0.2104
Slope	17.88138 ± 0.07411
Residual Sum of Squares	0.19428
Pearson's r	0.99997
R-Square(COD)	0.99995
Adj. R-Square	0.99993

Appendix Figure 4 - Seebeck coefficient measurements for Cot samples with 3 printed layers of: **(a)** 20 wt% G ink and **(b)** 30 wt% of G ink.

C | TOUCH DETECTION TESTS - DIFFERENT USERS

The touch detection test is dependent on two different temperatures: the room temperature and the user finger temperature. This means that, even if the RT is kept constant, the sensors response will vary with the user temperature and on the other hand, a same user can have different responses, if the RT is different or if he is using a glove or not. This is relevant for the results **section 4.3.3**, where were a change in the tester user for the touch detection tests. To confirm this, a simple test was performed, where two users touched the same sensor ate the same time, with and without gloves, as can be seen in the following **Appendix Figure 5**:

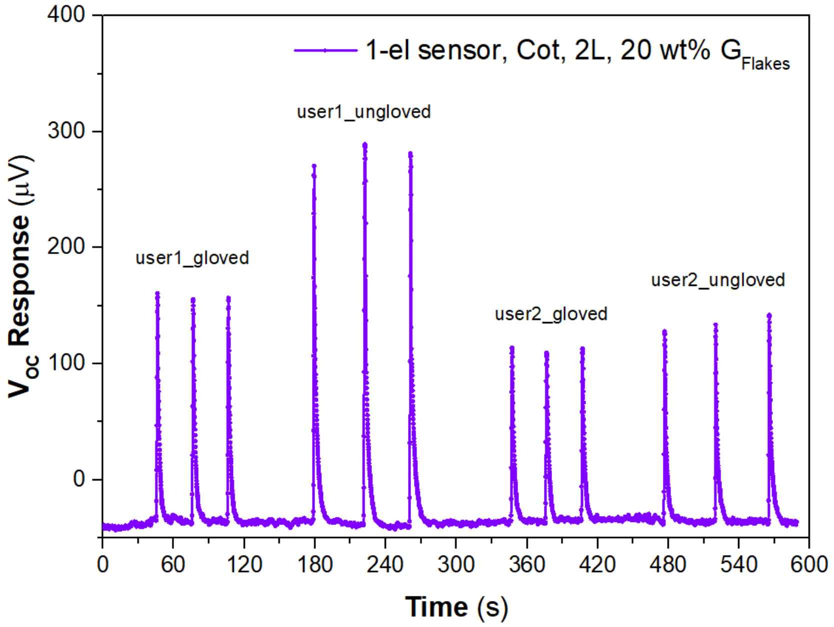

Appendix Figure 5 - Sensor response for a touch detection test, with two different users, for gloved and ungloved fingers.

D Touch Time Variation

The main objective was the optimization of the sensor's SNR, and not the response times, indeed, the higher the amplitude of the output response (for instance, due to a warmer touch or due to a longer touch), the slower these times are. **Figure 4.12** - **(a)** of the main text, in which several touch times were tested, underlines that behaviour. Moreover, with older samples, the same touch time variation test was carried out, but for quicker touches, **Appendix Figure 6**. The same sensor was touched with three different thermal contact times, giving distinct responses. Although this figure shows a normalization of all curves, the rise and fall times were calculated normalizing each peak individually.

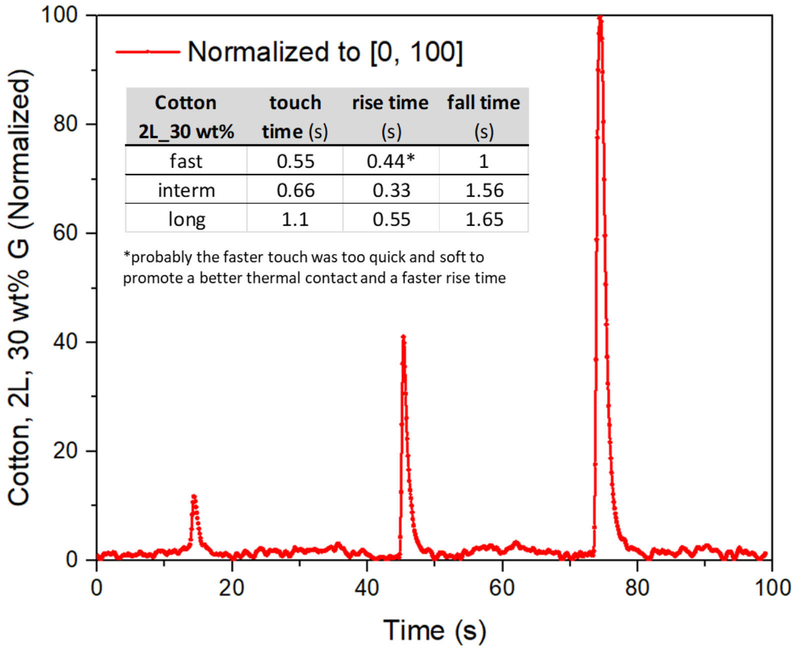

Cotton 2L_30 wt%	**touch time** (s)	**rise time** (s)	**fall time** (s)
fast	0.55	0.44*	1
interm	0.66	0.33	1.56
long	1.1	0.55	1.65

*probably the faster touch was too quick and soft to promote a better thermal contact and a faster rise time

Appendix Figure 6 - Touch detection tests for very fast gloved touches.

E | STATIC CONTACT ANGLE MEASUREMENTS

Full compilation off CA measurements, for the three encapsulant materials studied, on cotton and paper substrates.

Appendix Table 1 - Contact angle measurements summary table. (* represents measurements where water droplets were absorbed by the substrate; - represents measurements that were not performed).

Substrate	Encapsulation Material	Encapsulant Thickness (μm)	Ink Formulation ratio (V/V)	Layers	Contact Angle (°)					
					Before Bending		After Bending		After 1 min submersion	After 5 min submersion
					1 min	5 min	1 min	5 min		
Cotton	None	n.a.	n.a.	n.a.	~ 0	-	-	-	-	-
	Laminated Plastic	80 - 125	n.a.	1	90 ± 4	73 ± 2	76 ± 1	72 ± 1	81 ± 3	-
	PVA in water	4	1:7	1	125 ± 2	118 ± 4	123 ± 4	122 ± 3	127 ± 6	131 ± 5
	EC in EtOH&DAA	4	80:20	1	121 ± 4	119 ± 3	116 ± 2	111 ± 2	120 ± 2	111 ± 9
Paper	None	n.a.	n.a.	n.a.	~ 0	-	-	-	-	-
	Laminated Plastic	80 - 125	n.a.	1	91 ± 1	75 ± 4	82 ± 1	75 ± 6	84 ± 3	-
	PVA in water	4	1:7	1	88 ± 5	*	-	-	-	-
				2	89 ± 5	86 ± 6	91 ± 3	80 ± 5	87 ± 5	-
			3:2	1	52 ± 5	-	-	-	-	-
		90	1:7	1	*	-	-	-	-	-
				2	78 ± 1	-	-	-	-	-
	EC in EtOH&DAA	4	80:20	1	116 ± 4	108 ± 2	106 ± 2	103 ± 2	103 ± 4	-

F | VARIATION OF THE GRAPHITE CONTENT IN VERTICAL TOUCH DETECTORS

Three vertical devices of six elements connected electrically in series each were tested to check the differences between using 40, 45 or 50 wt% of graphite in the PDMS composite in vertical touch detectors, **Appendix Figure 7**. The results show that using 40 wt% of graphite in the composition is enough to achieve fast responses with SNR bigger than 30. However, looking at the electrical resistance values there is a huge decrease in resistivity when adding more G_{Flakes}, which is critical and should be considered when the goal is to connect multiple elements to increase the V_{OUT} and/or the goal is energy generation. On the other hand, although the 50 wt% composition presents higher electrical conductivity without significant losses in the response signal, the processability issues explained in **section 5.2.2** determine that the optimal composition to explore in vertical sensors is the one with 45 wt% of G_{Flakes}.

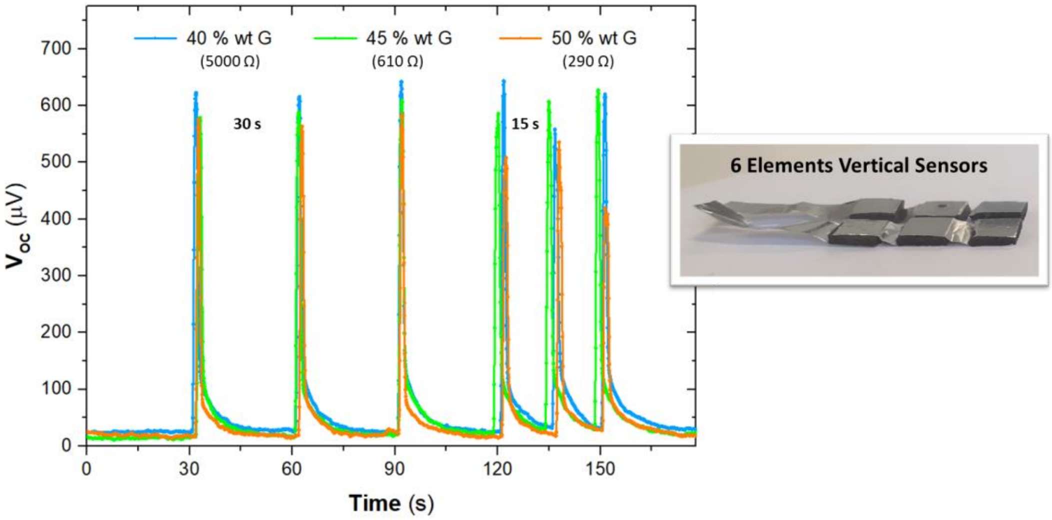

Appendix Figure 7 - Touch detection results for vertical samples with 6 elements connected electrically in series, varying the G_{Flakes} concentration and the period between gloved touches.

G | VALIDATION OF THERMAL STIMULUS EXCLUSIVITY

The following graph in **Appendix Figure 8** confirms that the developed thermoelectric sensors respond exclusively to the thermal stimulus during the experiments. A vertical PDMS/G_{Flakes} device with 6 elements connected electrically in series was submitted to a test where the V_{OC} was measured over time while the sensor was stimulated first with a hot water glass, which originated a voltage peak, and afterwards with a room temperature water glass, where no response was recorded.

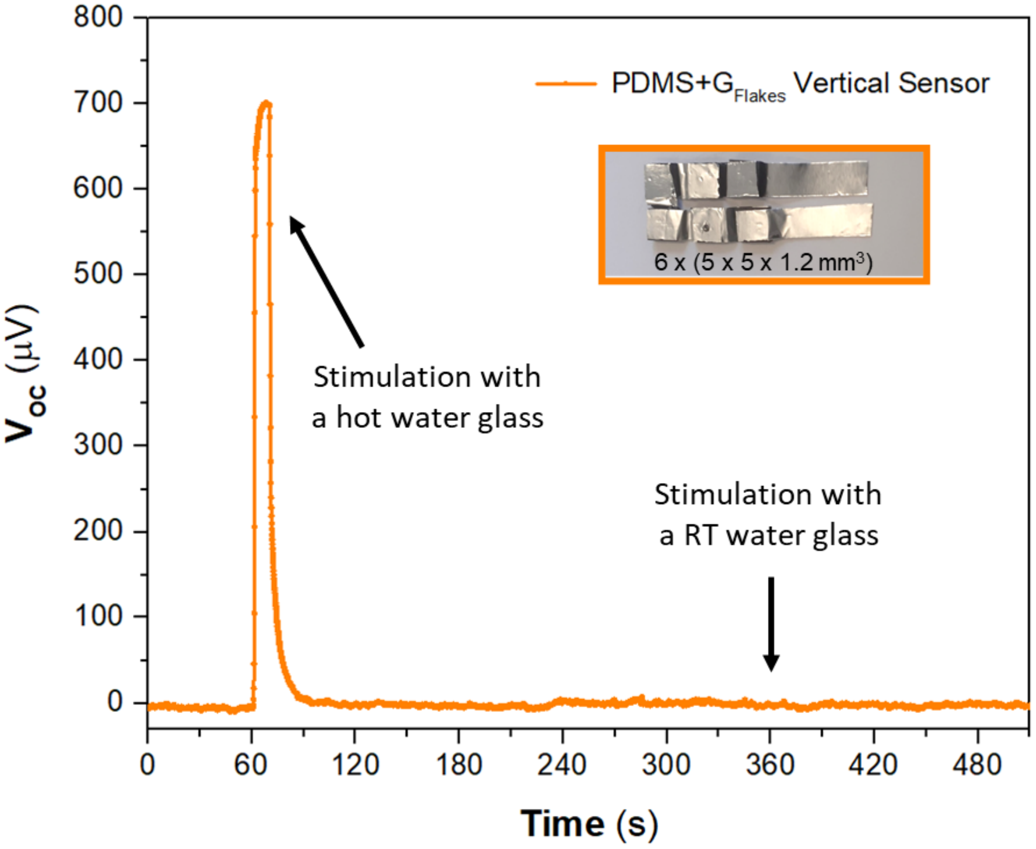

Appendix Figure 8 - Open circuit potential results for two water glass contacts with the PDMS/G_{Flakes} sensor depicted in the inset image - the initial peak was consequence of a thermal stimulation event during ~10 s due to the hot water inside the glass and the absence of response in the following period meant that the contact with the water glass at room temperature did not stimulate the sensor.

UNIVERSIDADE NOVA DE LISBOA

PRINTED ECO-MATERIALS FOR FLEXIBLE
THERMOELECTRIC DEVICES

JOANA ROUMELIOTIS SAMPAIO
FIGUEIRA

2023